Università degli Studi di Padova

DIPARTIMENTO DI INGEGNERIA INDUSTRIALE DII

Corso di Laurea Magistrale in
Ingegneria Aerospaziale

Low-energy tour of the Galilean moons

Studente

Andrea Viale
Mat. 1104437

Relatore

Prof. Enrico Lorenzini

Correlatori

Dr. Elena Fantino
Polytechnic University of Catalonia

Dr. Roberto Castelli
Vrije University Amsterdam

Prof. Kathleen C. Howell
Purdue University

ACKNOWLEDGEMENTS

Contents

Abstract

This thesis is aimed at studying direct (i.e., without intermediate flybys) trajectories to visit different moons of a planetary system. In particular, the case of study is that of the Galilean moons Europa, Ganymede and Callisto, first observed by Galileo Galilei in 1610, orbiting around Jupiter. The work is motivated by the growing interest in the robotic exploration of the Jovian moons, justified by the possible existence of water beneath their surfaces, and the consequent need for efficient trajectories with low fuel requirements connecting their neighbourhoods. Moreover, due to the intense particle radiation environment characterizing the Jovian magnetosphere, each moon-to-moon connection should be fast in terms of time of flight. For the same reason, the inner Galilean moon Io has been excluded from this work, being strongly affected by the radiation belts of the gas giant planet.

Two physical models are employed in this study: the circular restricted three-body problem and the restricted two-body problem. The former is used to study the spacecraft's dynamics in the vicinity of the moons, the primaries being Jupiter and one of its moon and the secondary being the spacecraft. The latter is employed to approximate the dynamics in regions far from the moons: in this case, the sole gravity of Jupiter is considered, neglecting the effects of the moons. Since the circular restricted three-body problem is employed in the vicinity of the moons, the trajectories we find are classified as *low-energy* trajectories. The planar assumption is made, since the relative inclinations between the orbital planes of the Galilean moons are much smaller than one degree.

The method to link the several sections where different models are used is explained. We want to identify trajectories going from Europa (the inner moon) towards Callisto (the outer moon, among the three considered) passing by Ganymede (outward journey), and then back to Europa (inward journey). This two-way journey is called a *tour*.

To study the trajectory in the vicinity of the moons several mathematical tools typical of the circular restricted three-body problem have been employed. In particular, the planar orbits around the equilibrium points,

their associated phase space structures (invariant manifolds) that regulate the transport of material to/from them (and provide a conduit between primary bodies for separate three-body systems), and the trajectories travelling inside these region (transit orbits) able to execute loops around the moons without the need for additional fuel. By employing transit orbits in the vicinity of the moons, we show that the time of flight for each moon-to-moon connection can be substantially lowered over traditional methods employing multiple flybys.

The method developed allows to treat the connections between the several moon-to-moon sections as a kinematical problem. Such connections has a cost, which is valued as the norm of the variation in the spacecraft's velocity vector (ΔV) to increase/decrease its orbital energy to journey between consecutive moons. The trajectory minimizing the sum of the required ΔV is selected. The minimum-ΔV trajectory calls for specific relative phases between the moons which cannot be guaranteed at every instant during the journey. For this reason we show that parking orbits around Callisto and Ganymede are needed during the inward journey: these orbits allow to wait the right time for the required rephasing between the moons. On the other hand, these rephasing orbits permit to get closer to the moons and spend more time around them.

With the method employed in this thesis, the cost for each moon-to-moon connection, measured in $\mathrm{km\,s^{-1}}$, is about $1\,\mathrm{km\,s^{-1}}$. Even if this budget is roughly 40% of the one required by a Hohmann transfer, it is still large to be performed by means of chemical thrusters: we are currently studying how to convert the ΔV-manoeuvres to low-thrust arcs using electrical thrusters.

List of acronyms

CI   Circle of Influence

CR3BP   Circular Restricted Three-Body Problem

ESA   European Space Agency

IM   Invariant Manifold

IRF   Inertial Reference Frame

MMO   Multi-Moon Orbiter

NASA   National Aeronautics and Space Administration

NU   Nondimensional Units

PLO   Planar Lyapunov Orbit

PGT   Petit Grand Tour

SRF   Synodical Refernce Frame

STM   State Transition Matrix

TBB   Time Backward Branch

TFB   Time Forward Branch

TO   Transit Orbits

TOF   Time Of Flight

ZVC   Zero Velocity Curve

ZVS   Zero Velocity Surface

Chapter 1

Introduction

The objective of this thesis is to present a method to determine the minimum-cost direct (i.e., without intermediate flybys) trajectory connecting consecutive moons of a planetary system. In particular, an application to the Galilean moons Europa, Ganymede and Callisto is provided. The motivation of this work is the contemporary interest in the *in situ* exploration of the planetary systems of the giant planets and the consequent need for efficient trajectories with low fuel requirements enabling the execution of transfers between their several moons.

Among the future missions sharing the same interest, ESA's JUICE (ESA, 2014), due to launch in 2022, will execute a series of flybys around Europa and Callisto, eventually orbiting Ganymede [Grasset et al., 2013]; NASA's Europa Mission Plan calls for a spacecraft to be launched to Jupiter in the 2020s: the probe would orbit the gas giant planet every two weeks and execute close flybys of Europa [Lam et al., 2015]. Prior to this, the cancelled JIMO project was characterized by a trajectory with orbits around Europa, Ganymede and Callisto [Sims, 2006]. Such interest in the design of trajectories to explore the Jovian system was emphasized by the sixth edition of the Global Trajectory Optimization Competition [Petropoulos, 2013]. Notable contributions [Colasurdo et al., 2014, Izzo et al., 2013] based on multi-gravity assist techniques in the framework of the two-body problem allow several flybys at very low ΔV expense (on the order of tens of ms^{-1}).

By means of the dynamical systems theory, it is possible to find low-energy (i.e., in the framework of the three-body problem) trajectories connecting different equilibrium points of the three-body problems composed by Jupiter and its moons. The first study of a low-energy tour of a planetary system is the Petit Grand Tour (PGT), applied to the exploration of the icy moons of Jupiter [Koon et al., 2000, Koon et al., 2002]. The aim of the PGT is to find an itinerary to explore the moons of any planetary system with almost arbi-

trary trajectories. In the quoted papers, a transfer from Ganymede to Europa is considered (see Fig. 1.1a). The model is the coupled CR3BP, based on the connection between the Jupiter-Ganymede CR3BP and the Jupiter-Europa CR3BP. The trajectories of the two systems are linked together by means of suitable Poincaré sections in the intermediate regions between the two moons, where a change in velocity is applied. Intersections are sought between the unstable and stable invariant manifolds of planar Lyapunov orbits around collinear libration points of the two CR3BPs. These structures act as gravitational conduits able to link the primaries of different three-body systems. A PGT between Ganymede and Callisto takes 25 days and less than a half the amount of propellant required by a Hohmann transfer (which has a cost of $2.8\,\mathrm{km\,s^{-1}}$). Other attempts to find low-energy connections in planetary systems led to the Multi-Moon Orbiter (MMO) concept, in which resonant gravity assists are employed to switch from an orbit around a Jovian moon to another [Ross et al., 2003, Koon et al., 2000]. In this case, the ΔV requirements are very low (less than $10\,\mathrm{m\,s^{-1}}$) but the time of flight is extremely long (in the quoted papers the time of flight for a tour of Europa, Ganymede and Callisto is 4 years). An example of such trajectory is showed in Fig. 1.1b. [Grover and Ross, 2009] propose a semi-analytical method to decrease the time of flight of the MMO. Gravity assists are replaced by suitable impulsive manoeuvres: as a result the travel time is reduced from years to months with ΔVs of $100 \div 200\mathrm{m\,s^{-1}}$. The investigations of [Lantoine and Russell, 2011] and [Lantoine et al., 2011] show a systematic way to compute fuel optimal transfers between the Galilean moons Ganymede and Europa. The strategy consists in combining resonant gravity assists with manifold tubes. Solutions are obtained which require $50\,\mathrm{m\,s^{-1}}$ and take $160 \div 200$ days.

Similarly to the PGT approach, in [Fantino and Castelli, 2016a] the invariant manifolds of the planet-moon planar Lyapunov orbits are propagated and eventually approximated with Jupiter-centred Keplerian orbits in regions far from the moons. Intersections between the corresponding osculating ellipses identify possible connections. This method leads to a significant reduction in computing time while maintaining a substantial level of accuracy. Moreover, there is no need for Poincaré sections to find intersections between invariant manifolds. In the present work transit orbits are employed instead of invariant manifolds to find a tour of the Galilean moons. These trajectories travel inside the manifold conduits and provide a faster link between distant point of the three-body system. Besides, transit orbits can execute loops around the smaller primary without the need for fuel.

Furthermore, this work has roots in another series of papers which laid the foundations of the low-energy transfers in the Sun-Earth-Moon system. In [Koon et al., 2001] invariant manifolds are propagated from Lyapunov or-

(a) PGT concept   (b) MMO concept
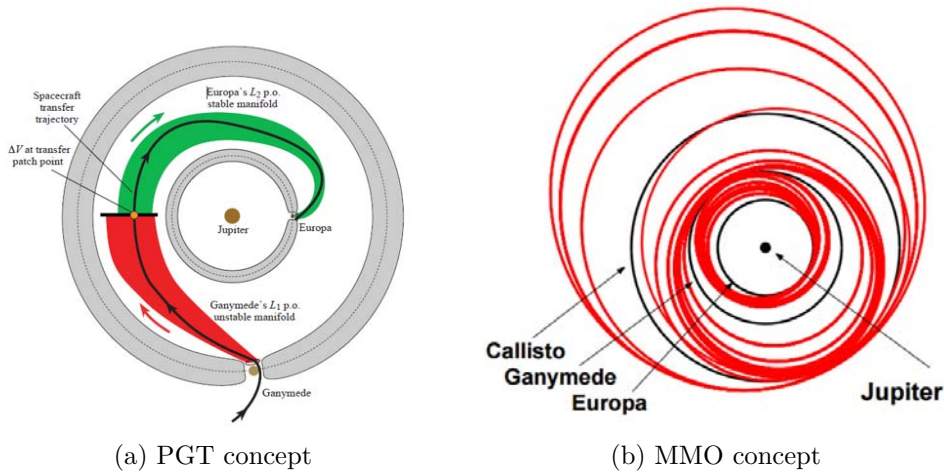
Figure 1.1: Left: a Petit Grand Tour of the Jupiter moons Ganymede and Europa [Koon et al., 2000]. Right: the Multi-Moon Orbiter concept for the Jovian moons, with resonant gravity assists between Europa, Ganymede ad Callisto [Ross et al., 2003].

bits in the Earth-Moon and Sun-Earth CR3BPs, in search for a low-ΔV intersection (see Fig. 1.2). Other significant contributions were given by [Zanzottera et al., 2012, Parker and Anderson, 2013].

The thesis is organized in four chapters.

- Chapter 2 defines the CR3BP and the related mathematical tools employed in this work. In particular, the planar orbits associated to the equilibrium points, the invariant manifolds and the transit orbits are explained.

- Chapter 3 describes the method to perform a moon-to-moon connection, by properly linking the CR3BP in the vicinity of the moons and the two-body approximation in the inter-moon region between them. An application to a transfer from Europa to Ganymede (and viceversa) is presented and the results are discussed.

- Chapter 4 explains how to repeatedly link moon-to-moon connections with the purpose to identify a two-way journey of the Galilean moons. The initial phases of the moons required to complete the tour are found and the rephasing problem is explained.

- Conclusions and final discussions follow in Chapter 5.
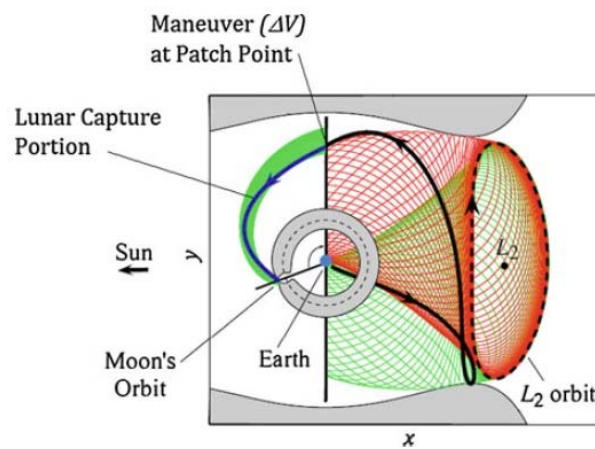
Figure 1.2: The first low-energy transfer to the Moon obtained by coupling two CR3BPs. The transfer is intended from a LEO to the vicinity of the L_2 of the Sun-Earth CR3BP through the stable manifold of a planar Lyapunov orbit, then from there to a Poincaré section through the unstable manifold of the same Lyapunov; an impulsive manoeuvre (ΔV at patch point) is then applied to join a trajectory of the stable manifold of a planar Lyapunov orbit around the L_2 point of the Earth-Moon CR3BP [Koon et al., 2001].

Chapter 2

The circular restricted three-body problem

Introduction. The circular restricted three-body problem (CR3BP) is the framework of the present work. Exploiting the natural dynamics provided by this problem offers a wider range of options with respect to the two-body problem approach, revealing structures that do not exist within the latter. Its properties are here introduced being them widely used as fundamental tools to perform trajectory design. After defining the problem, the equations of motions are derived using dimensionless coordinates. The autonomous character of the equations allows to find five points of equilibrium (Sect. 2.2). Existence of a first integral for the equations of motion, related to the conserved mechanical energy, is proven (Sect. 2.3). Studying the stability of the equilibrium points (Sect. 2.6) and linearising the equations of motion in their vicinity (Sect. 2.7) reveals the existence of periodic solutions (Sect. 2.8). Invariant manifold theory is introduced in connection with the collinear libration points (Sect. 2.9), and their associated planar periodic orbits (Sect. 2.11). These latter structures, in particular, are crucial in trajectory design and their role of separatrices leads to the definition of transit orbits (Sect. 2.13). These objects will be used as a means to find low-energy connections between couples of CR3BPs. Fundamental references include [Szebehely, 2012, Gómez and Mondelo, 2001, Gómez, 2001, Gómez et al., 2001, Gómez et al., 2004, Masdemont and Mondelo, 2004] for the CR3BP and [Perko, 2013, Parker and Chua, 2012] for the invariant manifold theory.

The circular restricted three-body problem considers three point masses P_1, P_2, P_3 with P_3 (e.g., the spacecraft) negligible with respect to P_1 and P_2 (often called *primary* and *secondary* respectively or *primaries* to refer to
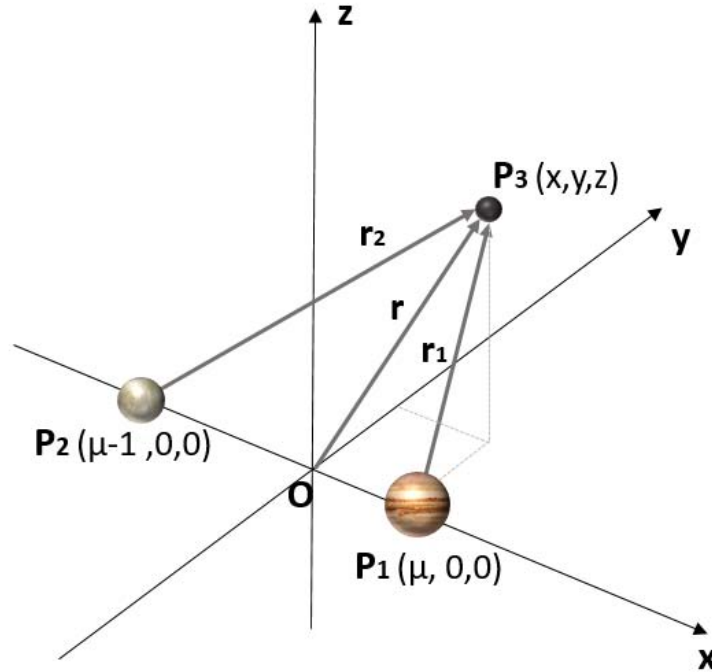
Figure 2.1: The primaries and the third body in the synodical reference frame. In this figure Jupiter (P_1) and Europa (P_2) are represented as primaries.P_3 is the third massless body. With the convention used in the present work, the smaller primary has negative x coordinate. In this figure, the coordinates of the primaries are given in normalized units.

both). The problem is further called *circular* because P_1 and P_2 are moving in circular orbits about each other and around their common barycentre. Therefore, the motion of the masses P_1 and P_2 is completely known. If the motion of P_3 is constrained to occur in the orbital plane of the primaries, the problem is also called *planar*, otherwise it is called *spatial*.

Let the *synodical reference frame* (SRF) (Figure 2.1) be the co-moving frame whose x-axis always contains the two primaries P_1 and P_2 in fixed positions, with the origin on their barycentre O; the y-axis lies in the orbital plane. The primaries are orbiting around each other in a circular orbit of radius r_{12}. In addition we define the *inertial reference frame* (IRF) as an inertial system centered on O. The inertial, angular velocity $\boldsymbol{\omega}$ is

$$\boldsymbol{\omega} = \omega\mathbf{k} \tag{2.1}$$

where

$$\omega = \frac{2\pi}{T}, \tag{2.2}$$

$\mathbf{k}$ is the unit vector along the SRF z-axis and T is the period of the primaries

$$T = 2\pi \frac{r_{12}^{3/2}}{\sqrt{GM}}, \tag{2.3}$$

being $G = 6.674\,08 \times 10^{-11}\,\mathrm{m^3\,kg^{-1}\,s^{-2}}$ the gravitational constant and $M = m_1 + m_2$ with m_i the mass P_i. For convention, the smaller primary is on the left of the origin, whereas the larger is on the right.[1] The *mass ratio* μ of the system is defined as

$$\mu = \frac{m_2}{m_1 + m_2}, \tag{2.4}$$

being $m_2 < m_1$ without loss of generality. Hence, μ is always smaller than $1/2$. The equations of motion of P_3 in the IRF are given by the Newton's second law

$$m_3\ddot{\mathbf{r}} = \mathbf{F_1} + \mathbf{F_2}, \tag{2.5}$$

being

$$\mathbf{F_1} = -\frac{Gm_1 m}{r_1^3}\mathbf{r_1}, \tag{2.6}$$

$$\mathbf{F_2} = -\frac{Gm_2 m}{r_2^3}\mathbf{r_2}, \tag{2.7}$$

$\mathbf{r_1}$, $\mathbf{r_2}$ the position vector of P_3 with respect to P_1 and P_2 respectively, and r_1, r_2 their magnitudes. We can easily rewrite the inertial acceleration $\ddot{\mathbf{r}}$ by means of the acceleration decomposition theorem:

$$\ddot{\mathbf{r}} = \mathbf{a_G} + \mathbf{a}_{\mathrm{rel}} + \dot{\boldsymbol{\omega}} \times \mathbf{r} + \boldsymbol{\omega} \times (\boldsymbol{\omega} \times \mathbf{r}) + 2\boldsymbol{\omega} \times \mathbf{v}_{\mathrm{rel}} \tag{2.8}$$

where $\mathbf{v}_{\mathrm{rel}} = \dot{x}\mathbf{i} + \dot{y}\mathbf{j} + \dot{z}\mathbf{k}$ is the relative velocity, $\mathbf{a}_{\mathrm{rel}} = \ddot{x}\mathbf{i} + \ddot{y}\mathbf{j} + \ddot{z}\mathbf{k}$ the relative acceleration and $\mathbf{a_G}$ the acceleration of the barycentre. Since the centre of mass of any n-body system within a central-force system has constant inertial velocity it follows that $\mathbf{a}_G = 0$. Equation (2.8) can thus be rewritten as:

$$\ddot{\mathbf{r}} = (\ddot{x} - 2\omega\dot{y} - \omega^2 x)\mathbf{i} + (\ddot{y} + 2\omega\dot{x} - \omega^2 y)\mathbf{j} + \ddot{z}\mathbf{k}, \tag{2.9}$$

where $\mathbf{i}, \mathbf{j}, \mathbf{k}$ are unit vectors along the SRF principal axes. To avoid the dependence of the previous equations on system quantities such as the masses

---

[1]It is frequent to find the opposite convention as well, with the smaller primary on the right and the larger on the left. A π rotation around the z-axis is required to switch from one representation to the other.

of the primaries or the distance between them, a set of nondimensional parameters is introduced. In particular we define the *distance unit* (*1du*) and the *mass unit* (*1mu*) such that:

$$(1du) = r_{12} \tag{2.10}$$

$$(1mu) = m_1 + m_2. \tag{2.11}$$

We further define the *time unit* (*1tu*) to be such that the angular velocity of the primaries in their orbits is unitary, i.e., $\omega = 1\mathrm{rad}/1tu$. In these *normal units* we have:

$$1\mathrm{rad}/tu = \omega = \sqrt{\frac{G(m_1 + m_2)}{r_{12}^3}} = \sqrt{\frac{(1mu)}{(1du)^3}}. \tag{2.12}$$

Thus, the numerical value of the gravitational constant G is one in these units. In addition, the coordinates of the primaries becomes $P_1(\mu, 0, 0)$ and $P_2(\mu - 1, 0, 0)$ and the CR3BP becomes a one-parameter problem, the parameter being μ.

Using these nondimensional units, Eqs. (2.5) and (2.8) becomes respectively:

$$\ddot{\mathbf{r}} = -\frac{\mu}{r_1^3} - \frac{1 - \mu}{r_2^3} \tag{2.13}$$

and

$$\ddot{\mathbf{r}} = (\ddot{x} - 2\dot{y} - x)\mathbf{i} + (\ddot{y} + 2\dot{x} - y)\mathbf{j} + \ddot{z}\mathbf{k}, \tag{2.14}$$

being the coordinates x, y, z now expressed in normal units. Equating the right-hand sides of Eqs. (2.13) and (2.14) yields the equations of motion of the CR3BP in nondimensional units, written in the SRF:

$$\begin{cases} \ddot{x} = 2\dot{y} + x - \dfrac{(1-\mu)(x-\mu)}{r_1^3} - \dfrac{\mu(x+1-\mu)}{r_2^3}, \\[2mm] \ddot{y} = y - 2\dot{x} - \dfrac{(1-\mu)y}{r_1^3} - \dfrac{\mu y}{r_2^3}, \\[2mm] \ddot{z} = -\dfrac{(1-\mu)z}{r_1^3} - \dfrac{\mu z}{r_2^3}. \end{cases} \tag{2.15}$$

Since there is not explicit dependence on time in the equations of motion, the system of differential equations is called *autonomous*. Moreover, the equations are nonlinear because of the dependence from the inverse of the third power of the distances r_1 and r_2 of P_3 from P_1 and P_2 respectively. Moreover, for an initial condition belonging to the xy-plane (with $\dot{z}(t = 0) = 0$), the resulting trajectory will evolve in the same plane solely. Thus, the planar

circular restricted three-body problem may be studied independently of the spatial circular restricted three-body problem. Using the vector notation, we can rewrite the previous system of second-order equations as:

$$\dot{\mathbf{x}} = \mathbf{f}(\mathbf{x}), \tag{2.16}$$

being:

$$\mathbf{x} = \{x, y, z, \dot{x}, \dot{y}, \dot{z}\}^T \tag{2.17}$$

and

$$\mathbf{f}(\mathbf{x}) = \begin{Bmatrix} f_1 \\ f_2 \\ f_3 \\ f_4 \\ f_5 \\ f_6 \end{Bmatrix} = \begin{Bmatrix} \dot{x} \\ \dot{y} \\ \dot{z} \\ 2\dot{y} + x - \dfrac{(1-\mu)(x-\mu)}{r_1^3} - \dfrac{\mu(x+1-\mu)}{r_2^3} \\ y - 2\dot{x} - \dfrac{(1-\mu)y}{r_1^3} - \dfrac{\mu y}{r_2^3} \\ -\dfrac{(1-\mu)z}{r_1^3} - \dfrac{\mu z}{r_2^3} \end{Bmatrix}. \tag{2.18}$$

The system (2.18) is not analytically integrable over time. A solution can be numerically approximated, once an initial state x_0 is given

$$\mathbf{x_0} = \begin{Bmatrix} \mathbf{r_0} \\ \mathbf{v_0} \end{Bmatrix} (t = 0). \tag{2.19}$$

Sometimes we will refer to the *flow* of Eq. (2.16). The flow Φ_t of $\mathbf{f}$ is defined so that $\Phi_t = \Phi(\mathbf{x}, t)$ is smooth and $\dfrac{d}{dt}\Phi(\mathbf{x}, t)|_{t=\tau} = \mathbf{f}(\Phi(\mathbf{x}, \tau))$.

2.1 Transformations between synodical and inertial reference frames

Coordinate transformation between reference frames is useful to evaluate the Keplerian orbital elements at specified points along the integrated trajectory. The SRF is rotating around the IRF at constant speed ω, as defined in Eq. (2.2) and, for convenience, the two frames are assumed to be aligned at the initial time $t = t_0 = 0$.

Since Keplerian elements are defined in the two-body problem and are referred to the relative motion of two bodies, a change of origin is required to centre the system on the given primary. In particular, if

$$\mathbf{x} = \{x, y, z, \dot{x}, \dot{y}, \dot{z}\}^T \tag{2.20}$$

represents the state vector in the SRF, we will consider the translation:

$$\mathbf{x}_i = \mathbf{x} - \hat{\mathbf{r}}_i, \quad i = 1, 2 \tag{2.21}$$

where $\hat{\mathbf{r}}_1 = \{\mu, 0, 0, 0, 0, 0\}^{\mathrm{T}}$ and $\hat{\mathbf{r}}_2 = \{\mu - 1, 0, 0, 0, 0, 0\}^{\mathrm{T}}$ for the P_1-centered IRF and the P_2-centered IRF respectively. Defining

$$\mathbf{X}_i = \left\{X, Y, Z, \dot{X}, \dot{Y}, \dot{Z}\right\}^T \tag{2.22}$$

the inertial state vector in the P_i-centered IRF, the relation between the two frames is given by:

$$\mathbf{X}_i = \mathbf{T}\mathbf{x}_i, \tag{2.23}$$

being

$$\mathbf{T} = \begin{pmatrix} \mathbf{R} & \mathbf{0}_{3\times 3} \\ \dot{\mathbf{R}} & \mathbf{R} \end{pmatrix}, \tag{2.24}$$

with the submatrices defined as follows:

$$\mathbf{R} = \begin{pmatrix} \cos t & -\sin t & 0 \\ \sin t & \cos t & 0 \\ 0 & 0 & 1 \end{pmatrix}, \tag{2.25}$$

$$\dot{\mathbf{R}} = \begin{pmatrix} -\sin t & -\cos t & 0 \\ \cos t & -\sin t & 0 \\ 0 & 0 & 1 \end{pmatrix}, \tag{2.26}$$

and $\mathbf{0}_{3\times 3}$ is the 3×3 matrix with all the elements equal to zero.

2.2   Equilibrium points

In the SRF we can identify specific points in which the combined gravitational pull exerted by P_1 and P_2 on P_3 is exactly balanced by the centripetal force required by P_3 to rotate with the SRF. These equilibrium locations are therefore stationary from the perspective of an observer within the SRF:

placing P$_3$ in one of these locations with zero velocity and zero acceleration will result in no motion. We can thus find these points by imposing in the Eqs. (2.15):

$$\dot{x} = \dot{y} = \dot{z} = 0, \quad \ddot{x} = \ddot{y} = \ddot{z} = 0, \tag{2.27}$$

which eventually results in the system:

$$x - \frac{(1-\mu)(x-\mu)}{r_1^3} - \frac{\mu(x+1-\mu)}{r_2^3} = 0, \tag{2.28a}$$

$$y \left[1 - \frac{1-\mu}{r_1^3} - \frac{\mu}{r_2^3} \right] = 0, \tag{2.28b}$$

$$z \left[\frac{1-\mu}{r_1^3} + \frac{\mu}{r_2^3} \right] = 0. \tag{2.28c}$$

From Eq. (2.28c), since the term in brackets is always positive, it follows that $z = 0$: the equilibrium points lie in the orbital plane of the primaries. Five solutions exist for their x and y coordinates, divided into two categories:

- Collinear equilibrium points (also known as *libration* or *Lagrangian* points). They are obtained by setting $y = 0$, i.e., by imposing that the solution lies on the x axis. In this case, we can rewrite Eq. (2.28a) as:

$$x - \frac{(1-\mu)(x-\mu)}{|x-\mu|^3} - \frac{\mu(x+1-\mu)}{|x+1-\mu|^3} = 0, \tag{2.29}$$

where $y = z = 0$. This equation takes three possible outcomes, according to the sign of the factors $(x - \mu)$ and $(x + 1 - \mu)$.

1. The solution lies between the primaries, i.e., $x - \mu + 1 > 0$, $x - \mu < 0$. Equation (2.29) is simplified as:

$$x + \frac{(1-\mu)}{(x-\mu)^2} - \frac{\mu}{(x+1-\mu)^2} = 0. \tag{2.30}$$

With the substitution $u = x + 1 - \mu$, Eq. (2.30) eventually becomes:

$$u^5 + u^4(\mu - 3) + u^3(3 - 2\mu) - u^2\mu + 2\mu u - \mu = 0. \tag{2.31}$$

This is an algebraic 5th-degree equation. Using Sturm's theorem [Sturm, 1835], we can prove that there is only one (positive) real solution, when μ is very small, being this condition verified in the majority of real cases (see Appendix A for further details), and this solution corresponds to the L$_1$ point. The exact x coordinates cannot be found analytically but can be determined numerically using $u_0 = (\mu/3)^{\frac{1}{3}}$ as an initial condition for Eq. (2.31) [Moulton, 2012].

2. The solution lies on the left of the smaller primary, i.e., $x - \mu + 1 < 0$, $x - \mu < 0$. In this case, the quintic equation is:

$$u^5 + u^4 + (\mu - 3) + u^3(3 - 2\mu) + u^2\mu - 2\mu u + \mu = 0. \quad (2.32)$$

   With similar considerations, it can be proven that a single real solution exists, and its value is calculated numerically from the initial condition $u_0 = -(\mu/3)^{\frac{1}{3}}$ [Moulton, 2012]. The resulting point is L$_2$.

3. The solution lies on the right of the larger primary, i.e., $x - \mu + 1 > 0$, $x - \mu > 0$. With the same notation, L$_3$ is found by solving:

$$u^5 + u^4 + (\mu - 3) + u^3(3 - 2\mu) + u^2(\mu - 2) + 2\mu u - \mu = 0$$

   using the initial condition $u_0 = \dfrac{7\mu}{12}\left[1 + \dfrac{23}{84}\left(\dfrac{7\mu}{12}\right)^2\right]$ [Moulton, 2012].

- Triangular equilibrium points. These points are found after observing that $r_1 = r_2 = 1$ is a solution of Eqs. 2.28a, 2.28b. Hence, two more equilibrium points are located at the vertexes of two equilateral triangles (displayed with a dotted line in Fig. 2.2). Their coordinates are clearly: $x = \mu - \dfrac{1}{2}$, $y = \mp\dfrac{\sqrt{3}}{2}$. The point with positive y is L$_4$, the other is L$_5$.

A representation of these points is given in Fig. 2.2 for the Earth-Moon system.

2.3   Jacobi constant

Equations (2.15) can be rewritten in a more compact form by means of the effective potential Ω. Ω is the sum of centrifugal potential and gravitational potential, often added to a constant term, i.e., $\left[\frac{1}{2}\mu(1 - \mu)\right]$, the meaning of which will be clarified later:

$$\Omega = \frac{1}{2}(x^2 + y^2) + \frac{1 - \mu}{r_1} + \frac{\mu}{r_2} + \left[\frac{1}{2}\mu(1 - \mu)\right]. \quad (2.33)$$

Thus, equations (2.15) become

$$\begin{cases} \ddot{x} - 2\dot{y} = \Omega_x, \\ \ddot{y} + 2\dot{x} = \Omega_y, \\ \ddot{z} = \Omega_z, \end{cases} \quad (2.34)$$
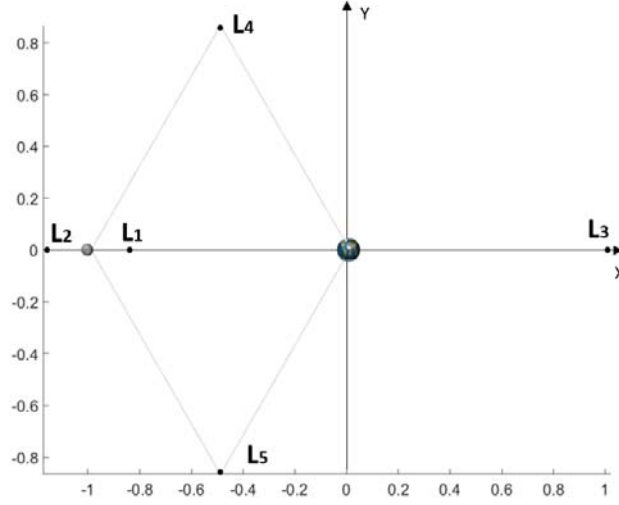
Figure 2.2: Position of the five equilibrium points for the Earth-Moon CR3BP ($\mu = 0.121\,506\,683 \times 10^{-1}$). L$_4$ and L$_5$ are located at the vertices of two equal equilateral triangles of unit side. The sizes of the Earth and the Moon are not to scale.

where the notation Ω_x means differentiation with respect to x. In terms of Ω, the vector field $\mathbf{f}(\mathbf{x})$ (Eq. (2.18)) is given by:

$$
\mathbf{f}(\mathbf{x}) = \left\{
\begin{array}{c}
\dot{x} \\
\dot{y} \\
\dot{z} \\
2\dot{y} + x + \Omega_x \\
y - 2\dot{x} + \Omega_y \\
\Omega_z
\end{array}
\right\},
\tag{2.35}
$$

In addition, we observe that the location of the equilibrium points can also be written as the solution of

$$
\nabla\Omega = \mathbf{0}.
\tag{2.36}
$$

Consider now the sum $\dot{x}\ddot{x} + \dot{y}\ddot{y} + \dot{z}\ddot{z}$. We can rewrite it as the total derivative of Ω and then of the kinetic energy with respect to time. From Eqs. (2.2) and then Eq. (2.34):

$$
\dot{x}\ddot{x} + \dot{y}\ddot{y} + \dot{z}\ddot{z} = \dot{x}(2\dot{y} + \Omega_x) + \dot{y}(-2\dot{x} + \Omega_y) + \dot{z}\Omega_z = \frac{d\Omega}{dt}.
\tag{2.37}
$$

Alternatively:

$$\dot{x}\ddot{x} + \dot{y}\ddot{y} + \dot{z}\ddot{z} = \frac{d}{dt}\frac{1}{2}(\dot{x}^2 + \dot{y}^2 + \dot{z}^2). \tag{2.38}$$

Therefore:

$$\frac{d}{dt}\frac{1}{2}(\dot{x}^2 + \dot{y}^2 + \dot{z}^2) = \frac{d\Omega}{dt}. \tag{2.39}$$

Introducing now the arbitrary constant J, the last equation can be integrated as follows

$$\frac{1}{2}(\dot{x}^2 + \dot{y}^2 + \dot{z}^2) = \Omega - \frac{J}{2}. \tag{2.40}$$

Manipulating this equation using (2.33) yields to the following result:

$$J = x^2 + y^2 + \frac{2(1-\mu)}{r_1} + \frac{2\mu}{r_2} + [\mu(1-\mu)] - (\dot{x} + \dot{y}^2 + \dot{z}^2). \tag{2.41}$$

This is the expression for the *Jacobi constant J*. Sometimes we will refer to J as the energy, implicitly referring to the value $E = -J/2$. The constant term $[\mu(1-\mu)]$ provides $J = 3$ at points L_4 and L_5. From Eq. (2.40) we can rewrite Eq. 2.41 in terms of Ω:

$$J = 2\Omega - v^2, \tag{2.42}$$

with $v^2 = x^2 + y^2 + z^2$.

2.4   Zero velocity surfaces

Even though the motion of P_3 cannot be determined analytically, its motion is bounded under certain conditions. From Eq. (2.42), when $J < 2\Omega(x, y, z)$ the velocity becomes imaginary. Thus, the components x, y and z of the position vector must be such that $2\Omega(x, y, z) \geq J$. Regions in space where that constraint is not respected are denoted as *forbidden* regions. The boundary of the forbidden region is a set of three-dimensional zero-velocity surfaces (ZVSs) which vary as functions of J (Fig. 2.3b). A projection of these zero-velocity surfaces onto the xy-plane results in the so called zero-velocity curves (ZVCs) (Fig. 2.3a). The region surrounding the larger primary is often defined as *interior* region (or *Hill's region*), the region in the vicinity of the smaller primary as P_2 *region*, and the region beyond the ZVCs as *exterior* region. Identifying with J_{L_i} the value of the Jacobi constant at L_i ($i = 1, 2, \ldots, 5$), it can be verified that:

$$J_{L_1} > J_{L_2} > J_{L_3} > J_{L_4} = J_{L_5}. \tag{2.43}$$

(a) Zero-velocity curves

(b) Zero-velocity surfaces
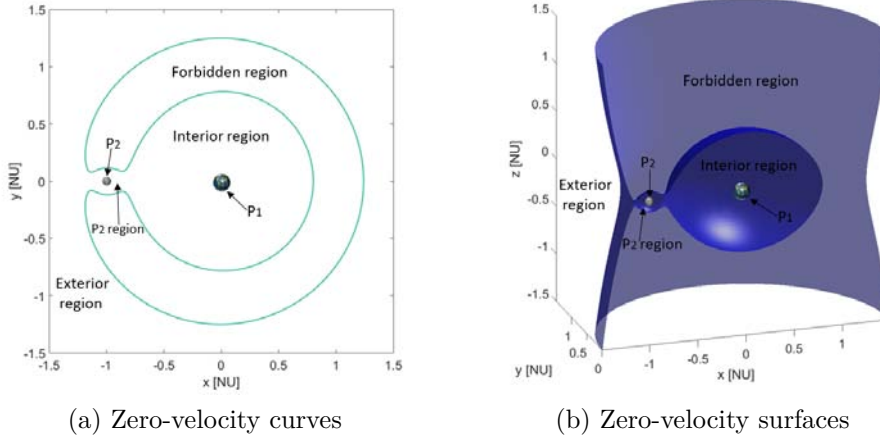
Figure 2.3: ZVCs and ZVSs (a three-dimensional cut on a xz-plane is displayed) for the Earth-Moon system with $J = 3.17$ (Earth and Moon are not to scale). Coordinates are expressed in nondimensional units (NU). At this energy level, P_3 is allowed to move inside the whole realm of interior region, P_2 region and exterior region.

Varying J over the intervals between consecutive values of J_{L_i} yields different possible morphologies for the ZVCs. At higher values of J, P_3 is confined around one of the two regions around P_1 or P_2, depending on the initial conditions (Fig. 2.4a). As J decreases, a *gateway* through L_1 arises; for values lower than J_{L_1} (Fig. 2.4b), the L_1 gateway opens and expands: P_3 can now move between the inner region and the P_2 region. Further decreasing the Jacobi constant below J_{L_2} (Fig. 2.4c) and J_{L_3} (Fig. 2.4d) opens the gateways nearby L_2 and L_3 respectively. For $J_{L_4}, J_{L_5} < J < J_{L_3}$ P_3 can move towards the exterior region (Fig. 2.4e) and eventually in the whole space for values greater than $J_{L_4} = J_{L_5}$ (Fig. 2.4f).

2.5 The state transition matrix

The *state transition matrix* (STM) is a useful tool to study the behaviour of the system (2.16) in response to a perturbation in the initial state relative to a particular reference solution. Assume that

$$\mathbf{x}_0(t) = \{x_0(t), y_0(t), z_0(t), \dot{x}_0(t), \dot{y}_0(t), \dot{z}_0(t)\}^{\mathrm{T}} \qquad (2.44)$$

(a) $J_{L_1} < J$

(b) $J = J_{L_1}$

(c) $J = J_{L_2}$

(d) $J = J_{L_3}$

(e) $J_{L_4}, J_{L_5} < J < J_{L_3}$

(f) $J = J_{L_4} = J_{L_5}$

Figure 2.4: Zero-velocity curves for several values of the Jacobi constant for the Earth-Moon system. Earth and Moon are not to scale.

is a reference solution to Eq. (2.16), i.e., $\dot{\mathbf{x}}_0 = \mathbf{f}(\mathbf{x}_0)$. Then, a nearby solution $\mathbf{x}(t) = \mathbf{x}_0(t) + \delta\mathbf{x}(t)$ can be represented via a Taylor series such that:

$$\dot{\mathbf{x}} = \dot{\mathbf{x}}_0 + \delta\dot{\mathbf{x}} = \mathbf{f}(\mathbf{x}_0) + \frac{\partial \mathbf{f}}{\partial \mathbf{x}}(\mathbf{x}_0)\delta\mathbf{x} + \text{H.O.T.} \qquad (2.45)$$
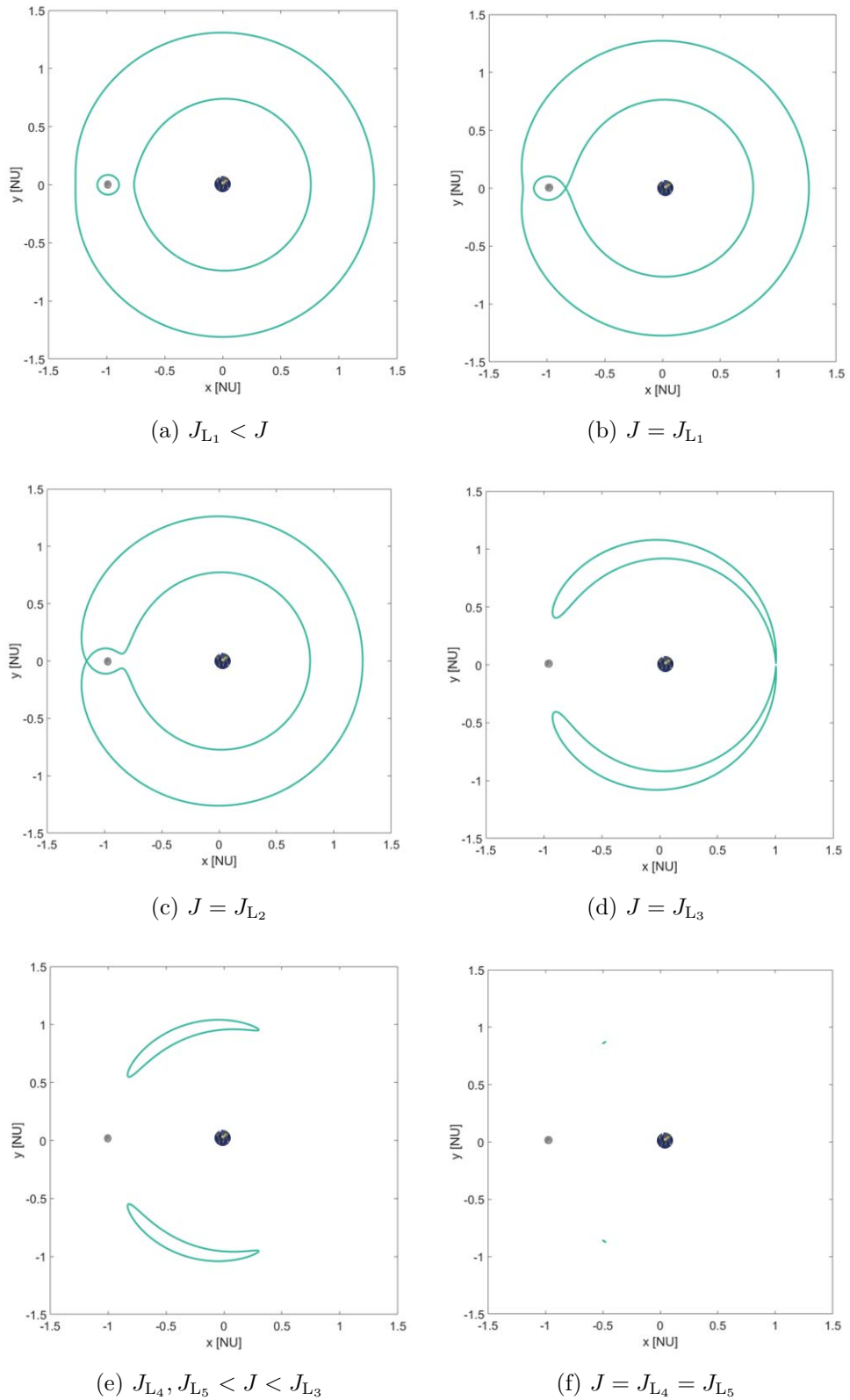
When the higher order terms (H.O.T) are neglected a linear system of differential equations is produced for $\delta\mathbf{x}$ such that:

$$\delta\dot{\mathbf{x}} = \mathbf{A}(t)\delta\mathbf{x}_0. \qquad (2.46)$$

The matrix $\mathbf{A}(t) = \dfrac{\partial \mathbf{f}}{\partial \mathbf{x}}(\mathbf{x}_0)$ has the following structure:

$$\frac{\partial \mathbf{f}}{\partial \mathbf{x}}(\mathbf{x}_0) = \mathbf{A}(t) \begin{bmatrix} \frac{\partial f_1}{\partial x_0} & \frac{\partial f_1}{\partial y_0} & \frac{\partial f_1}{\partial z_0} & \frac{\partial f_1}{\partial \dot{x}_0} & \frac{\partial f_1}{\partial \dot{y}0} & \frac{\partial f_1}{\partial \dot{z}_0} \\ \frac{\partial f_2}{\partial x_0} & \frac{\partial f_2}{\partial y_0} & \frac{\partial f_2}{\partial z_0} & \frac{\partial f_2}{\partial \dot{x}_0} & \frac{\partial f_2}{\partial \dot{y}0} & \frac{\partial f_2}{\partial \dot{z}_0} \\ \frac{\partial f_3}{\partial x_0} & \frac{\partial f_3}{\partial y_0} & \frac{\partial f_3}{\partial z_0} & \frac{\partial f_3}{\partial \dot{x}_0} & \frac{\partial f_3}{\partial \dot{y}0} & \frac{\partial f_3}{\partial \dot{z}_0} \\ \frac{\partial f_4}{\partial x_0} & \frac{\partial f_4}{\partial y_0} & \frac{\partial f_4}{\partial z_0} & \frac{\partial f_4}{\partial \dot{x}_0} & \frac{\partial f_4}{\partial \dot{y}0} & \frac{\partial f_4}{\partial \dot{z}_0} \\ \frac{\partial f_5}{\partial x_0} & \frac{\partial f_5}{\partial y_0} & \frac{\partial f_5}{\partial z_0} & \frac{\partial f_5}{\partial \dot{x}_0} & \frac{\partial f_5}{\partial \dot{y}0} & \frac{\partial f_5}{\partial \dot{z}_0} \\ \frac{\partial f_6}{\partial x_0} & \frac{\partial f_6}{\partial y_0} & \frac{\partial f_6}{\partial z_0} & \frac{\partial f_6}{\partial \dot{x}_0} & \frac{\partial f_6}{\partial \dot{y}0} & \frac{\partial f_6}{\partial \dot{z}_0} \end{bmatrix}. \qquad (2.47)$$

By using the vector field of the CR3BP represented by Eqs. (2.35), the previous matrix $\mathbf{A}(t)$ takes the form:

$$\mathbf{A}(t) = \begin{bmatrix} 0 & 0 & 0 & 1 & 0 & 0 \\ 0 & 0 & 0 & 0 & 1 & 0 \\ 0 & 0 & 0 & 0 & 0 & 1 \\ \Omega_{xx} & \Omega_{xy} & \Omega_{xz} & 0 & 2 & 0 \\ \Omega_{yx} & \Omega_{yy} & \Omega_{yz} & -2 & 0 & 0 \\ \Omega_{zx} & \Omega_{zy} & \Omega_{zz} & 0 & 0 & 0 \end{bmatrix}, \qquad (2.48)$$

where we used the notation $\Omega_{pq} = \dfrac{\partial^2 \Omega}{\partial p \partial q}$ for the second-order partial derivatives of the effective potential (2.33) (they are listed in Appendix B). In general, this 6×6 matrix is evaluated along the reference trajectory and is time-varying. The solution to Eq. (2.46) has the general form:

$$\delta\mathbf{x}(t) = \mathbf{\Phi}(t, t_0)\delta\mathbf{x}(t_0), \qquad (2.49)$$

where $\mathbf{\Phi}(t, t_0)$ is the state transition matrix (or *matrizant*). The expression in Eq. (2.49) linearly relates variations in the trajectory at time t to the initial perturbation at time t_0. Hence, the components of the STM are the partial derivatives of the state at time t with respect the state at time t_0:

$$\mathbf{\Phi} = \frac{\partial \mathbf{x}}{\partial \mathbf{x_0}}. \tag{2.50}$$

In other words,

$$\mathbf{\Phi}(t, t_0) = \Phi_{ij} = \begin{bmatrix} \frac{\partial x}{\partial x_0} & \frac{\partial x}{\partial y_0} & \frac{\partial x}{\partial z_0} & \frac{\partial x}{\partial \dot{x}_0} & \frac{\partial x}{\partial \dot{y}_0} & \frac{\partial x}{\partial \dot{z}_0} \\ \frac{\partial y}{\partial x_0} & \frac{\partial y}{\partial y_0} & \frac{\partial y}{\partial z_0} & \frac{\partial y}{\partial \dot{x}_0} & \frac{\partial y}{\partial \dot{y}_0} & \frac{\partial y}{\partial \dot{z}_0} \\ \frac{\partial z}{\partial x_0} & \frac{\partial z}{\partial y_0} & \frac{\partial z}{\partial z_0} & \frac{\partial z}{\partial \dot{x}_0} & \frac{\partial z}{\partial \dot{y}_0} & \frac{\partial z}{\partial \dot{z}_0} \\ \frac{\partial \dot{x}}{\partial x_0} & \frac{\partial \dot{x}}{\partial y_0} & \frac{\partial \dot{x}}{\partial z_0} & \frac{\partial \dot{x}}{\partial \dot{x}_0} & \frac{\partial \dot{x}}{\partial \dot{y}_0} & \frac{\partial \dot{x}}{\partial \dot{z}_0} \\ \frac{\partial \dot{y}}{\partial x_0} & \frac{\partial \dot{y}}{\partial y_0} & \frac{\partial \dot{y}}{\partial z_0} & \frac{\partial \dot{y}}{\partial \dot{x}_0} & \frac{\partial \dot{y}}{\partial \dot{y}_0} & \frac{\partial \dot{y}}{\partial \dot{z}_0} \\ \frac{\partial \dot{z}}{\partial x_0} & \frac{\partial \dot{z}}{\partial y_0} & \frac{\partial \dot{z}}{\partial z_0} & \frac{\partial \dot{z}}{\partial \dot{x}_0} & \frac{\partial \dot{z}}{\partial \dot{y}_0} & \frac{\partial \dot{z}}{\partial \dot{z}_0} \end{bmatrix}. \tag{2.51}$$

Given some initial perturbation $\delta \mathbf{x}(t_0)$ of the reference initial state $\mathbf{x}_0(t_0)$, the STM predicts the variation $\delta \mathbf{x}(t)$ of the state $\mathbf{x}_0(t)$ at a later time t. It has the following general properties:

$$\mathbf{\Phi}(t_0, t_0) = \mathbf{I}, \tag{2.52}$$
$$\mathbf{\Phi}(t_2, t_0) = \mathbf{\Phi}(t_2, t_1)\mathbf{\Phi}(t_1, t_0), \tag{2.53}$$
$$\mathbf{\Phi}(t_0, t_1) = \mathbf{\Phi}^{-1}(t_1, t_0). \tag{2.54}$$

Substituting Eq. (2.49) into the differential equations (2.46) yields the following differential equation for the STM:

$$\dot{\mathbf{\Phi}}(t, t_0) = \mathbf{A}(t)\mathbf{\Phi}(t, t_0). \tag{2.55}$$

So far, only variations of the state have been considered. However, variations with respect to a reference might also include time. In this case, Eq. (2.49) becomes:

$$\delta \mathbf{x}(t) = \mathbf{\Phi}(t, t_0)\delta \mathbf{x}(t_0) + \frac{\partial \mathbf{x}}{\partial t}\delta t$$
$$= \mathbf{\Phi}(t, t_0)\delta \mathbf{x}(t_0) + \mathbf{f}\delta t. \tag{2.56}$$

Hence, given a variation $\delta \mathbf{x}_0$ from a reference trajectory and variation in time δt_f, Eq. (2.56) predicts the final state at t_f as sketched in Fig 2.5.
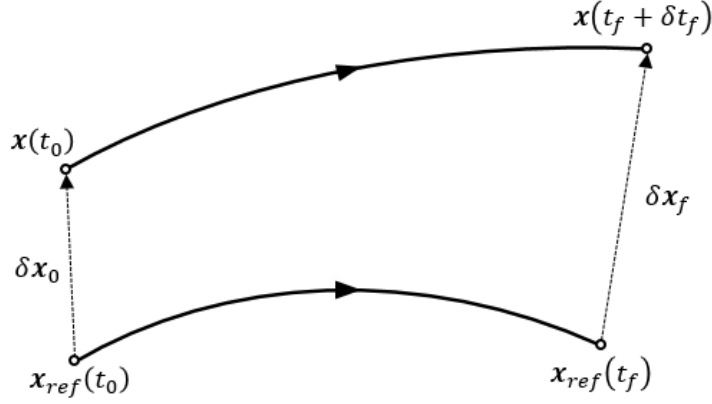
Figure 2.5: Perturbation of the state $\delta\mathbf{x}_0$ from the reference $\mathbf{x}_{\text{ref}}(t_0)$ leads to the variation $\delta\mathbf{x}_f$ of the state $\mathbf{x}_{\text{ref}}(t_f)$ by means of Eq. (2.56).

2.6 Stability of the equilibrium points

To analyse the behaviour of Eq. (2.15) in the vicinity of the equilibrium points the concept of stability must first be defined. The motion around an equilibrium point is defined *stable* if, when a particle initially in that point is perturbed, its subsequent motion remains bounded within a "small" neighbourhood of the equilibrium point itself.

In the equilibrium points of the CR3BP, the matrix $\mathbf{A}$ in Eq. (2.48) is constant (see Appendix B). Hence, from the fundamental theorem of linear systems [Perko, 2013], the solution to Eq. (2.46) can be expressed as:

$$\delta\mathbf{x}(t) = e^{\mathbf{A}(t-t_0)}\delta\mathbf{x}(t_0). \tag{2.57}$$

Hence, $\mathbf{A}$ can be rewritten in the form $\mathbf{A} = \mathbf{S}\mathbf{\Lambda}\mathbf{S}^{-1}$ where the columns of $\mathbf{S}$ are the eigenvectors $\mathbf{v}_i$ of $\mathbf{A}$ and the matrix $\mathbf{\Lambda}$ is diagonal with elements equal to the corresponding eigenvalues λ_i ($i = 1, \ldots 6$). Then, Eq. (2.57) with $t_0 = 0$ can be rewritten as

$$\delta\mathbf{x} = \mathbf{S}\, e^{\mathbf{\Lambda}}\, \mathbf{S}^{-1}\, \delta\mathbf{x}_0. \tag{2.58}$$

Now, if $\mathbf{A}$ admits n distinct eigenvalues[2], the previous equation can be rewrit-

---

[2]if the eigenvalues are not all distinct, Eq. (2.60) has the solution

$$\delta\mathbf{x}(t) = \mathbf{S}\,\text{diag}[\lambda_i(t-t_0)]\,\mathbf{S}^{-1}\left[\mathbf{I} + \mathbf{N}t + \cdots + \frac{\mathbf{N}^{k-1}t^{k-1}}{(k-1)!}\right]\delta\mathbf{x}_0 \tag{2.59}$$

where $\mathbf{N} = \mathbf{A} - \mathbf{P}$, with $\mathbf{P} = \mathbf{S}\text{diag}(\lambda_i)\mathbf{S}^{-1}$. The order k is chosen such that $\mathbf{N}^{k-1} \neq 0$, $\mathbf{N}^k = 0$.

ten as:

$$\delta\mathbf{x}(t) = \mathbf{S} \, \text{diag}[\lambda_i(t - t_0)] \, \mathbf{S}^{-1} \delta\mathbf{x}_0. \qquad (2.60)$$

It is clear from this equation that the eigenvalues λ_i of the matrix $\mathbf{A}$ govern the behaviour of $\delta\mathbf{x}(t)$. On the basis of the sign of $\Re(\lambda_i)$ we can classify different stability conditions at the equilibrium points.

- All the eigenvalues have $\Re(\lambda_i) < 0$: the point is stable.

- All the eigenvalues has $\Re(\lambda_i) > 0$: the point is unstable.

- There exist some $\Re(\lambda_i) > 0$ and some $\Re(\lambda_i) < 0$. The point is called a *saddle* and it is unstable.

- All the eigenvalues has zero real part. The point is called *centre* and it is stable.

In general, if $\text{Real}(\lambda) \neq 0$ for all the eigenvalues the point is called *hyperbolic*. Moreover we talk about the *centre part* when referring to specific eigenvalues with zero real part; similarly the *saddle part* stands for pairs of opposite eigenvalues with non-zero real part. For the CR3BP, the stability conditions are here analysed.

1. *Coordinate transformation.* It is more convenient to carry out the study from a reference frame centered at the given equilibrium point. So we define a transformation of coordinates consisting in a translation of the origin from the synodical barycentric frame to L_i $(i = 1, \ldots, 5)$. The axes are kept parallel to the original ones:

$$\begin{Bmatrix} x \\ y \\ z \end{Bmatrix} = \begin{Bmatrix} a \\ b \\ 0 \end{Bmatrix} + \begin{Bmatrix} \xi \\ \eta \\ \zeta \end{Bmatrix} \qquad (2.61)$$

where $\{a, b, 0\}^T$ is the position vector of the ith Lagrangian point and $\xi = \delta x$, $\eta = \delta y$, $\zeta = \delta z$. Velocities and accelerations of the third body in this new frame are the same as in the original one:

$$\begin{Bmatrix} \dot{x} \\ \dot{y} \\ \dot{z} \end{Bmatrix} = \begin{Bmatrix} \dot{\xi} \\ \dot{\eta} \\ \dot{\zeta} \end{Bmatrix}, \qquad \begin{Bmatrix} \ddot{x} \\ \ddot{y} \\ \ddot{z} \end{Bmatrix} = \begin{Bmatrix} \ddot{\xi} \\ \ddot{\eta} \\ \ddot{\zeta} \end{Bmatrix}. \qquad (2.62)$$

Thus, the equations of motion (2.34) remain unchanged in the coordinates (ξ, η, ζ):

$$\begin{cases} \ddot{\xi} - 2\dot{\eta} = \Omega_\xi, \\ \ddot{\eta} + 2\dot{\xi} = \Omega_\eta, \\ \ddot{\zeta} = \Omega_\zeta. \end{cases} \tag{2.63}$$

2. *Taylor series expansion of the effective potential around L_i.* The three-dimensional Taylor expansion of the effective potential around the ith Lagrangian point is:

$$\Omega = \Omega^0 + \Omega_\xi^0 \xi + \Omega_\eta^0 \eta + \Omega_\zeta^0 + \text{H.O.T.} \tag{2.64}$$

being $\Omega^0 = \Omega|_{L_i}$ the potential function evaluated at L_i.

3. *Linearization of the equations of motion.* Substituting Eq. (2.64) in Eq. (2.63) and neglecting the higher-order terms yields:

$$\begin{cases} \ddot{\xi} - 2\dot{\eta} &= \Omega_{\xi\xi}^0 \xi + \Omega_{\xi\eta}^0 \eta + \Omega_{\xi\zeta}^0 \zeta, \\ \ddot{\eta} + 2\dot{\xi} &= \Omega_{\eta\xi}^0 \xi + \Omega_{\eta\eta}^0 \eta + \Omega_{\eta\zeta}^0 \zeta, \\ \ddot{\zeta} &= \Omega_{\zeta\xi}^0 \xi + \Omega_{\zeta\eta}^0 \eta + \Omega_{\zeta\zeta}^0 \zeta. \end{cases} \tag{2.65}$$

Here the first-order partial derivatives of Ω disappear due to Eq. (2.36). Moreover, being the second-order derivative a continuous function, the mixed derivatives are equal (Schwarz's theorem): $\Omega_{pq} = \Omega_{qp}$. After introduction of the vectorial notation

$$\mathbf{x} = \begin{Bmatrix} x_1 \\ x_2 \\ x_3 \\ x_4 \\ x_5 \\ x_6 \end{Bmatrix} = \begin{Bmatrix} \xi \\ \eta \\ \zeta \\ \dot{\xi} \\ \dot{\eta} \\ \dot{\zeta} \end{Bmatrix}, \tag{2.66}$$

Eq. (2.65) takes the following more compact form

$$\dot{\mathbf{x}} = \mathbf{A}^0 \mathbf{x}, \tag{2.67}$$

in which:

$$\mathbf{A^0} = \begin{bmatrix} 0 & 0 & 0 & 1 & 0 & 0 \\ 0 & 0 & 0 & 0 & 1 & 0 \\ 0 & 0 & 0 & 0 & 0 & 1 \\ \Omega_{\xi\xi}^0 & \Omega_{\xi\eta}^0 & \Omega_{\xi\zeta}^0 & 0 & 2 & 0 \\ \Omega_{\eta\xi}^0 & \Omega_{\eta\eta}^0 & \Omega_{\eta\zeta}^0 & -2 & 0 & 0 \\ \Omega_{\zeta\xi}^0 & \Omega_{\zeta\eta}^0 & \Omega_{\zeta\zeta}^0 & 0 & 0 & 0 \end{bmatrix}. \tag{2.68}$$

The matrix $\mathbf{A^0}$ has the same structure as (2.48). However, since it is evaluated at a specific position, i.e., an equilibrium point, it is constant.

4. *Analysis of the eigenvalues.* The stability of the system of differential equations (2.67) can be studied through the analysis of the associated characteristic equation:

$$\det(\mathbf{A^0} - \lambda \mathbf{I}) = 0, \tag{2.69}$$

in which λ represents the generic eigenvalue. The analysis is similar for collinear and triangular libration points.

- Collinear libration points. Since $\eta = \zeta = 0$, from Appendix B we easily infer that $\Omega_{\xi\eta}^0 = \Omega_{\eta\zeta}^0 = \Omega_{\xi\zeta}^0 = 0$. Moreover, the signs of the pure second-order derivatives are as follows:

$$\Omega_{\xi\xi}^0 > 0, \quad \Omega_{\eta\eta}^0 < 0, \quad \Omega_{\zeta\zeta}^0 < 0. \tag{2.70}$$

Equation (2.69) becomes:

$$(\lambda^2 - \Omega_{\zeta\zeta}^0)[(\lambda^4) + \lambda^2(4 - \Omega_{\xi\xi}^0 - \Omega_{\eta\eta}^0) + \Omega_{\eta\eta}^0\Omega_{\xi\xi}^0] = 0. \tag{2.71}$$

By means of the substitutions:

$$\Lambda = \lambda^2, \tag{2.72a}$$

$$\beta_1 = 2 - \frac{\Omega_{\xi\xi}^0 + \Omega_{\eta\eta}^0}{2}, \tag{2.72b}$$

$$\beta_2 = -\Omega_{\xi\xi}^0\Omega_{\eta\eta}^0, \tag{2.72c}$$

the characteristic equation takes the form

$$(\Lambda - \Omega_{\zeta\zeta}^0)(\Lambda^2 + 2\beta_1\Lambda - \beta_2^2). \tag{2.73}$$

Its roots are:

$$\Lambda_1 = -\beta_1 + \sqrt{\beta_1^2 + \beta_2^2} > 0, \qquad (2.74a)$$

$$\Lambda_2 = -\beta_1 - \sqrt{\beta_1^2 + \beta_2^2} < 0, \qquad (2.74b)$$

$$\Lambda_3 = \Omega_{zz}^0 < 0. \qquad (2.74c)$$

Hence, the eigenvalues are:

$$\lambda_{1,2} = \pm\sqrt{\Lambda_1} = \pm\nu, \qquad (2.75a)$$

$$\lambda_{3,4} = \pm\sqrt{\Lambda_2} = \pm i\omega_p, \qquad (2.75b)$$

$$\lambda_{5,6} = \pm\sqrt{\Lambda_3} = \pm i\omega_v. \qquad (2.75c)$$

Overall the collinear equilibrium points behave linearly as the product of two centres (due to eigenvalues $\lambda_{3,4}$ and $\lambda_{5,6}$) by a saddle (due to eigenvalues $\lambda_{1,2}$). This means that in the vicinity of these points we deal with bounded orbits, associated with the central part, but also with escape trajectories which depart exponentially from the neighbourhood of the collinear points for $t \to \pm\infty$, and are due to the saddle part. In particular, $\lambda_{3,4}$ give rise to planar periodic orbits, $\lambda_{5,6}$ to vertical periodic orbits while the saddle part due to $\lambda_{1,2}$ is associated with stable/unstable invariant manifolds.

The instability behaviour of the collinear libration points has a key role in the study of the natural dynamics of the libration region, due to the saddle part. This allows to define dynamical structures responsible for transport of material to/from the neighbourhood of the libration points. For this reason, their behaviour will be further investigated in the next sections.

- Triangular equilibrium points. In this case, the mixed second-order derivatives are not all zero. They can easily be computed since the position of L$_4$ and L$_5$ are known exactly:

$$\Omega_{\xi\xi}^0 = \frac{3}{4}, \qquad (2.76a)$$

$$\Omega_{\eta\eta}^0 = \frac{9}{4}, \qquad (2.76b)$$

$$\Omega_{\xi\eta}^0 = \frac{3\sqrt{3}}{2}\left(\frac{1}{2} - \mu\right), \qquad (2.76c)$$

$$\Omega_{\xi\eta}^0 = \frac{3\sqrt{3}}{2}\left(\frac{1}{2} - \mu\right), \qquad (2.76d)$$

$$\Omega_{\xi\eta}^0 = \Omega_{\eta\zeta}^0 = 0. \qquad (2.76e)$$

Repeating the procedure used for the collinear equilibrium points leads to the following characteristic equation:

$$\lambda^4 + \lambda^2 + \frac{27}{4}\mu(1-\nu) = 0. \tag{2.77}$$

Hence, setting $\Lambda = \lambda^2$:

$$\Lambda_{1,2} = \frac{-1 \pm \sqrt{1 - 27\mu(1-\mu)}}{2}. \tag{2.78}$$

There exists a critical value of μ, which we call μ_{crit}, such that when $\mu > \mu_{\text{crit}}$, $\lambda_{12} > 0$ and the point is unstable:

$$\mu_{\text{crit}} = \frac{1}{2}\left(1 - \frac{\sqrt{69}}{9}\right) \approx 0.038521. \tag{2.79}$$

This critical value is rather high: for instance, the mass ratio of the CR3BPs composed by the Sun and each of the eight planets of the Solar System is smaller than μ_{crit}, implying that the corresponding triangular points are stable.

2.7   Linearised solutions around the collinear points

To write the linearised equation of motion around the collinear points, Eq. (2.63) is first rearranged. We define the variable γ as the distance of L_i $(i = 1, 2, 3)$ from the closest primary. Hence, for L_1 and L_2, γ is the distance from P_2, while for L_3 it is the distance from P_1. The second-order derivatives of the potential are derived in Appendix B.

- For L_1, $r_1^0 = 1 - \gamma$, $r_2^0 = \gamma$ and $x = \mu - 1 + \gamma$. It follows:

$$\Omega^0_{\xi\xi} = 1 + \frac{2(1-\mu)}{(1-\gamma)^3} + \frac{2\mu}{\gamma^3}, \tag{2.80a}$$

$$\Omega^0_{\eta\eta} = 1 - \frac{(1-\mu)}{(1-\gamma)^3} - \frac{\mu}{\gamma^3}, \tag{2.80b}$$

$$\Omega^0_{\zeta\zeta} = -\frac{(1-\mu)}{(1-\gamma)^3} - \frac{\mu}{\gamma^3}. \tag{2.80c}$$

- For L$_2$, $r_1^0 = 1 + \gamma$, $r_2^0 = \gamma$ and $x = \mu - 1 - \gamma$.

$$\Omega_{\xi\xi}^0 = 1 + \frac{2(1-\mu)}{(1+\gamma)^3} + \frac{2\mu}{\gamma^3}, \tag{2.81a}$$

$$\Omega_{\eta\eta}^0 = 1 - \frac{(1-\mu)}{(1+\gamma)^3} - \frac{\mu}{\gamma^3}, \tag{2.81b}$$

$$\Omega_{\zeta\zeta}^0 = -\frac{(1-\mu)}{(1+\gamma)^3} - \frac{\mu}{\gamma^3}. \tag{2.81c}$$

- For L$_3$, $r_1^0 = \gamma$, $r_2^0 = 1 + \gamma$ and $x = \mu + \gamma$.

$$\Omega_{\xi\xi}^0 = 1 + \frac{2(1-\mu)}{\gamma^3} + \frac{2\mu}{1+\gamma^3}, \tag{2.82a}$$

$$\Omega_{\eta\eta}^0 = 1 - \frac{(1-\mu)}{\gamma^3} - \frac{\mu}{1+\gamma^3}, \tag{2.82b}$$

$$\Omega_{\zeta\zeta}^0 = -\frac{(1-\mu)}{\gamma^3} - \frac{\mu}{1+\gamma^3}. \tag{2.82c}$$

We then define the constant c_2 [Richardson, 1980] as:

$$c_2 = \begin{cases} \dfrac{1}{\gamma^3}\left[\mu + \dfrac{(1-\mu)\gamma^3}{(1\mp\gamma)^3}\right], & \mathrm{L}_1^-, \mathrm{L}_2^+ \\[2ex] \dfrac{1}{\gamma^3}\left[1 - \mu + \dfrac{\mu\gamma^3}{(1+\gamma)^3}\right], & \mathrm{L}_3. \end{cases} \tag{2.83}$$

In the quoted paper, higher-order terms are taken into account; the value c_2 used here is the first-order approximation. Comparing (2.83) with Eqs. (2.80), (2.81) and (2.82) we see that $\Omega_{\xi\xi}^0 = 2c_2 + 1$, $\Omega_{\eta\eta}^0 = 1 - c_2$, $\Omega_{\zeta\zeta}^0 = -c_2$. Therefore, we can rewrite (2.63) as

$$\begin{cases} \ddot{\xi} - 2\dot{\eta} - (2c_2 + 1)\xi = 0, \\ \ddot{\eta} + 2\dot{\xi} + (c_2 - 1)\eta = 0, \\ \ddot{z} + c_2 z = 0, \end{cases} \tag{2.84}$$

and matrix $\mathbf{A^0}$ from equation (2.67) can be written as:

$$\mathbf{A^0} = \begin{bmatrix} 0 & 0 & 0 & 1 & 0 & 0 \\ 0 & 0 & 0 & 0 & 1 & 0 \\ 0 & 0 & 0 & 0 & 0 & 1 \\ 2c_2+1 & 0 & 0 & 0 & 2 & 0 \\ 0 & 1-c_2 & 0 & -2 & 0 & 0 \\ 0 & 0 & -c_2 & 0 & 0 & 0 \end{bmatrix}. \tag{2.85}$$

The third equation in system (2.84) is independent from the other two. It means that the motion in the vertical direction is not influenced by the motion in the xy plane. Being the matrix $\mathbf{A}^0$ constant, the general solution of (2.84) is

$$\begin{Bmatrix} \xi \\ \eta \\ \zeta \end{Bmatrix} = \sum_{i=1}^{n} \begin{Bmatrix} \xi_{0i} \\ \eta_{0i} \\ \zeta_{0i} \end{Bmatrix} e^{\lambda_i t}, \tag{2.86}$$

$$\begin{Bmatrix} \dot{\xi} \\ \dot{\eta} \\ \dot{\zeta} \end{Bmatrix} = \sum_{i=1}^{n} \begin{Bmatrix} \dot{\xi}_{0i} \\ \dot{\eta}_{0i} \\ \dot{\zeta}_{0i} \end{Bmatrix} e^{\lambda_i t}, \tag{2.87}$$

where $n = 6$ is the dimension of the state vector $\mathbf{x}$ in Eq. (2.67). The stability of this problem is similar to what seen in Sect. 2.6. The 4th-order characteristic equation is for the motion on the xy plane is

$$\lambda^4 - \lambda^2(c_2 - 2) + 1 + c_2 - 2c_2^2 = 0 \tag{2.88}$$

and its solutions:

$$\lambda_{1,2} = \pm\sqrt{\frac{c_2 - 2 + \sqrt{c_2(9c_2 - 8)}}{2}}, \tag{2.89}$$

$$\lambda_{3,4} = \pm\sqrt{\frac{c_2 - 2 - \sqrt{c_2(9c_2 - 8)}}{2}}. \tag{2.90}$$

For the motion along the z direction:

$$\lambda_{5,6} = \pm i\sqrt{c_2}. \tag{2.91}$$

It is easy to verify that $\lambda_{1,2}$ are real while $\lambda_{3,4}$ are complex. Therefore λ_1 and λ_2 are associated with exponential solutions whereas λ_3, λ_4, λ_5 and λ_6 are related to harmonic oscillations. Substituting

$$\lambda_{1,2} = \pm\nu, \tag{2.92}$$
$$\lambda_{3,4} = \pm i\omega_p, \tag{2.93}$$
$$\lambda_{5,6} = \pm i\omega_v, \tag{2.94}$$

yields the general linearised solution around the collinear points:

$$\begin{cases} \xi(t) = \xi_{01}e^{\nu t} + \xi_{02}e^{-\nu t} + \xi_{03}\cos(\omega_p t) + \xi_{04}\sin(\omega_p t), \\ \eta(t) = \eta_{01}e^{\nu t} + \eta_{02}e^{-\nu t} + \eta_{03}\cos(\omega_p t) + \eta_{04}\sin(\omega_p t), \\ \zeta(t) = \zeta_{01}\cos(\omega_v t) + \zeta_{02}\sin(\omega_v t). \end{cases} \tag{2.95}$$

ξ_{0i} and η_{0i} are not independent but related by Eq. (2.84). Upon substituting Eqs. (2.95) into Eqs. (2.84) and defining

$$k_1 = \frac{\nu_p^2 - 1 - 2c}{2\nu}, \tag{2.96}$$

$$k_2 = -\frac{\omega_p^2 + 1 + 2c}{2\omega_p}, \tag{2.97}$$

we notice that:

$$\eta_{01} = k_1 \xi_{01}, \tag{2.98a}$$

$$\eta_{02} = -k_1 \xi_{02}, \tag{2.98b}$$

$$\eta_{03} = -k_2 \xi_{04}, \tag{2.98c}$$

$$\eta_{04} = k_2 \xi_{03}. \tag{2.98d}$$

Thus we rewrite (2.95) as:

$$\begin{cases} \xi(t) = \xi_{01} e^{\nu t} + \xi_{02} e^{-\nu t} + \xi_{03} \cos(\omega_p t) + \xi_{04} \sin(\omega_p t), \\ \eta(t) = k_1 \xi_{01} e^{\nu t} - k_1 \xi_{02} e^{-\nu t} - k_2 \xi_{04} \cos(\omega_p t) + k_2 \xi_{03} \sin(\omega_p t), \\ \zeta(t) = \zeta_{01} \cos(\omega_v t) + \zeta_{02} \sin(\omega_v t), \end{cases} \tag{2.99}$$

where ν, ω_p, ω_v are those obtained in Sect. 2.6.

By appropriate selection of the initial values ξ_{0i}, η_{0i} and ζ_{0i} at time $t_0 = 0$, it is possible to isolate specific behaviours. If $\xi_{01} = \xi_{02} = 0$, from Eqs. (2.98a) and (2.98b) it follows that $\eta_{01} = \eta_{02} = 0$. Calling

$$\xi_{03} = A_x \cos \phi_{xy}, \tag{2.100a}$$

$$\xi_{04} = -A_x \sin \phi_{xy}, \tag{2.100b}$$

$$\zeta_{01} = A_z \cos \phi_z, \tag{2.100c}$$

$$\zeta_{02} = -A_z \sin \phi_z, \tag{2.100d}$$

with

$$A_x = \sqrt{\xi_{03}^2 + \xi_{04}^2}, \tag{2.101a}$$

$$A_z = \sqrt{\zeta_{01}^2 + \zeta_{02}^2}, \tag{2.101b}$$

$$\tan \phi_{xy} = \frac{\xi_{04}}{\xi_{03}}, \tag{2.101c}$$

$$\tan \phi_z = \frac{\zeta_{02}}{\zeta_{01}}, \tag{2.101d}$$

the motion is bounded and contains only oscillating terms:

$$\begin{cases} \xi(t) = A_x \cos(\omega_p t + \phi_{xy}), \\ \eta(t) = k_2 A_x \sin(\omega_p t + \phi_{xy}), \\ \zeta(t) = A_z \cos(\omega_v t + \phi_z). \end{cases} \tag{2.102}$$

As already noticed, the motion in the vertical direction is uncoupled from the x and y motion. Moreover, the frequency and the phase of the motion is the same in x and y: the projection of the trajectory onto the xy-plane is therefore an ellipse. If $A_z \neq 0$ the z-motion slowly traces out an elliptical cylinder shape. These linear solutions are called *Lissajous trajectories* and are quasi-periodic orbits [Howell and Pernicka, 1987]. Choosing an initial condition such that $A_z = 0$ provides a planar periodic orbit, called *planar Lyapunov orbit* (PLO). Since we will deal with the planar CR3BP, we are interested in these orbits. With $A_x = 0$, the solution is a *vertical Lyapunov orbit*: at the first-order it reduces to a one-dimensional motion in z, whereas to obtain a three-dimensional orbit, higher-order terms must be included. *Halo orbits* and their quasi-periodic counterparts known as quasi-halos are three-dimensional periodic orbits obtained by considering higher-order terms in the equations of motion [Howell, 1984]. Examples of Lissajous, planar and vertical Lyapunov and Halo orbits are illustrated in Fig. 2.6. On the other hand, selecting $\xi_{03} = \xi_{04} = 0$ (hence $\eta_{03} = \eta_{04} = 0$) allows to isolate the unstable divergent behaviour is isolated. Using the substitution $e^x = \cosh x + \sinh x$ and calling

$$\xi_{01} + \xi_{02} = B_x \cosh \chi, \tag{2.103a}$$
$$\xi_{02} - \xi_{02} = B_x \sinh \chi, \tag{2.103b}$$

with

$$B_x = 2\sqrt{\xi_{01}\xi_{02}}, \tag{2.104a}$$

$$\tanh \chi = \frac{\xi_{01} - \xi_{02}}{\xi_{01} + \xi_{02}}, \tag{2.104b}$$

the motion on the xy-plane results unbounded and described by the hyperbolic equations

$$\begin{cases} \xi(t) = B_x \cosh(\omega_p + \chi), \\ \eta(t) = k_2 B_x \sinh(\omega_p t + \phi). \end{cases} \tag{2.105}$$
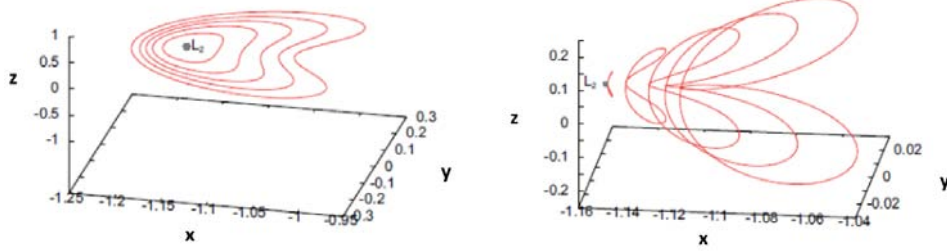
(a) Planar Lyapunov orbits around L$_2$

(b) Vertical Lyapunov orbits around L$_2$
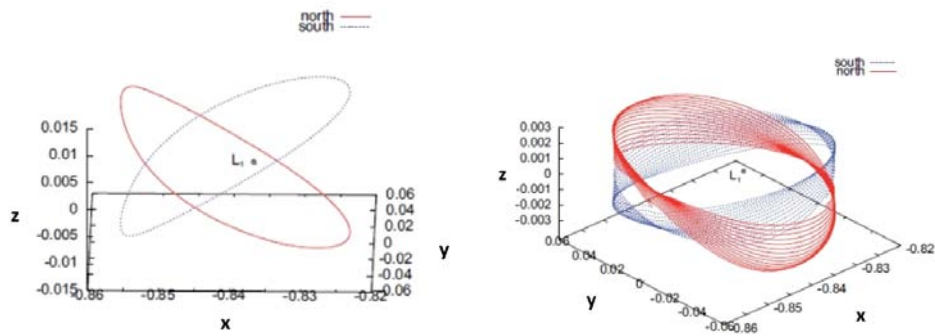
(c) Halo orbits around L$_1$

(d) Quasi-halo orbits around L$_1$
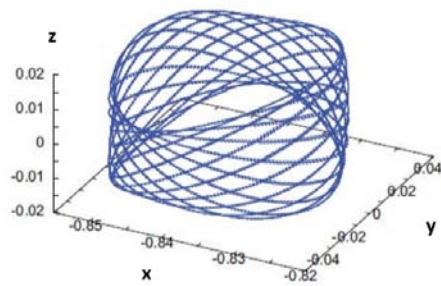
(e) Lissajous orbit around L$_1$

Figure 2.6: Examples of orbits around the libration points L$_1$ and L$_2$ in the Earth-Moon system [Alessi et al., 2010].

2.8 Computation of PLOs with the symmetry method

Equations (2.99) represent a linearisation of the nonlinear system (2.15) around the collinear points, therefore they are an adequate approximation of the motion only in close proximity of the equilibrium points. If one wants to obtain a valid solution far from the equilibrium point, nonlinear terms must be introduced in the equations of motion. For instance, *Linsted-Poincarè* procedures use Legendre polynomials to approximate the inverse of the distance involved in Eqs. (2.15); see for example [Farquhar and Kamel, 1973] for an application to Earth-Moon L_2. However, there is an alternative to compute an orbit far from the equilibrium point and we can still use the linearised equations to obtain suitable initial conditions.

From Eqs. (2.99) with $\xi_{01} = \xi_{02} = 0$

$$\begin{cases} \xi(t) = \xi_{03} \cos(\omega_p t) + \xi_{04} \sin(\omega_p t), \\ \eta(t) = -k_2 \xi_{04} \cos(\omega_p t) + k_2 \xi_{03} \sin(\omega_p t). \end{cases} \tag{2.106}$$

The velocities are:

$$\begin{cases} \dot{\xi}(t) = -\xi_{03}\omega_p \sin(\omega_p t) + \xi_{04}\omega_p \sin(\omega_p t), \\ \dot{\eta}(t) = k_2 \xi_{04}\omega_p \sin(\omega_p t) + k_2 \xi_{03}\omega_p \sin(\omega_p t). \end{cases} \tag{2.107}$$

At $t = 0$

$$\xi(t = 0) = \xi_{03}, \tag{2.108a}$$
$$\eta(t = 0) = -k_2 \xi_{04}. \tag{2.108b}$$

Imposing that the initial condition lies on the x-axis results in $\xi_{04} = 0$. Substituting these conditions in Eqs. (2.107) at $t = 0$ yields:

$$\dot{\xi}(t = 0) = \xi_{04}\omega_p = 0, \tag{2.109a}$$
$$\dot{\eta}(t = 0) = k_2 \xi_{03}\omega_p. \tag{2.109b}$$

The symmetry with respect to the x-axis is guaranteed by the *mirror theorem.*

Theorem 1. *(The mirror theorem)* *If n point masses are acted upon their mutual gravitational forces only, and at a certain epoch each radius vector from the center of mass of the system is perpendicular to every velocity vector, then the orbit of each mass after that epoch is a mirror image of its orbit prior to that epoch. Such a configuration of radius and velocity vectors is called a mirror configuration [Roy, 2004].*

Since such mirror configuration occurs at $t = 0$ (see Eqs. (2.109)), as a result of the previous theorem and to guarantee the periodicity, a new mirror configuration must occur at the next intersection with the x-axis: the resulting PLO will be symmetric with respect to the x-axis. As a consequence, it is necessary to consider only one half of the orbit, i.e., the part with positive y.

Using Eq. (2.56) with $t = T/2$, we represent the relationship between the variation $\delta\mathbf{x}$ at time $t = T/2$ with respect to the initial state $\delta\mathbf{x}_0$, being T the period of the PLO:

$$\delta\mathbf{x}(T/2) = \Phi(T/2)\delta\mathbf{x}_0 + \mathbf{f}(T/2)\delta t(T/2). \tag{2.110}$$

The initial condition at $t = 0$ will be $\mathbf{x_0} = \{\xi_{03} + x_{\mathrm{L}_i}, 0, 0, 0, k_2\xi_{03}\omega_p, 0\}^{\mathrm{T}}$, being x_{L_i} the x coordinate of the ith collinear point; ξ_{03} must be adequately small since this value was found under linear approximation. The initial guess for the y component of the velocity is chosen according to Eq. (2.109b). We then integrate until the trajectory cuts the x-axis again: the time it takes is a first approximation of half the period of the orbit. Since the initial condition $\dot{y}_0$ was just a guess, at $t = T/2$ the trajectory will have, in general, $\dot{x} \neq 0$. Therefore, a variation at $t = 0$

$$\delta\mathbf{x}_0 = \{0, 0, 0, 0, \delta\dot{y}_0, 0\}^{\mathrm{T}}, \tag{2.111}$$

will cause a variation at t:

$$\delta\mathbf{x} = \{\delta x, \delta y, 0, \delta\dot{x}, \delta\dot{y}, 0\}^{\mathrm{T}}. \tag{2.112}$$

In other words, we let $\dot{y}_0$ vary with everything else fixed (x_0) or null $(y_0, z_0, \dot{x}_0, \dot{z}_0)$ and we aim to change properly $x, y, \dot{x}, \dot{y}$ and half the period. The differential corrections to apply are derived by substituting (2.111) and (2.112) into Eq. (2.110):

$$\begin{Bmatrix} \partial x \\ \partial y \\ 0 \\ \partial\dot{x} \\ \partial\dot{y} \\ 0 \end{Bmatrix} = \begin{Bmatrix} \Phi_{15}\partial\dot{y}_0 + f_1\partial t \\ \Phi_{25}\partial\dot{y}_0 + f_2\partial t \\ \Phi_{35}\partial\dot{y}_0 + f_3\partial t \\ \Phi_{45}\partial\dot{y}_0 + f_4\partial t \\ \Phi_{55}\partial\dot{y}_0 + f_5\partial t \\ \Phi_{65}\partial\dot{y}_0 + f_6\partial t \end{Bmatrix}. \tag{2.113}$$

Since the only non-zero term in Eq. (2.111) is $\delta\dot{y}_0$, the only STM components that appear in Eq. (2.113) are Φ_{i5} $(i = 1, \ldots, 6)$. At $t = T/2$ we have $y = 0$
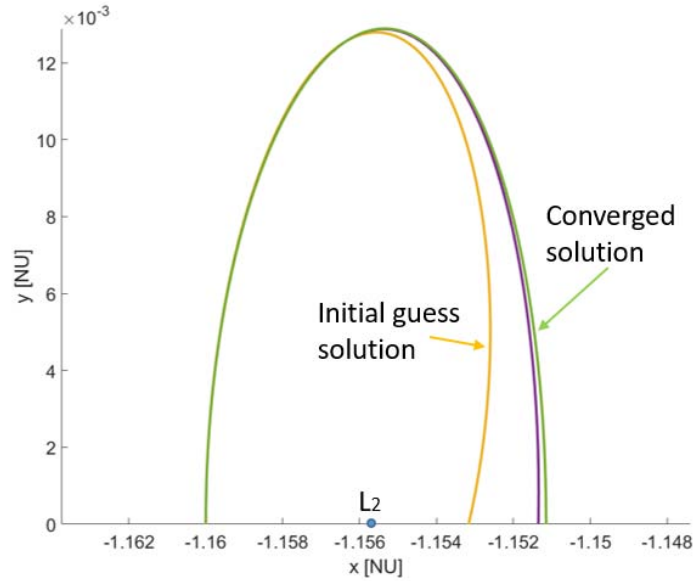
Figure 2.7: Application of differential corrections to compute a PLO around Earth-Moon L_2. The initial half-PLO (displayed in orange) is computed using the linear approximation at $t = 0$. The algorithm converges in a few steps, once $|\delta \dot{y}_0|$ falls below a given tolerance (in this case 10^{-10}).

and the corresponding variation will be zero as well. Moreover we want to correct $\dot{x}$ with a variation opposite to the current value at $t = T/2$. In other words:

$$\delta y = 0, \tag{2.114a}$$

$$\delta \dot{x} = -\dot{x}. \tag{2.114b}$$

Substituting in equation (2.113) and rearranging yields to:

$$\delta t = -\frac{\Phi_{25}}{f_2} \delta \dot{y}_0, \tag{2.115a}$$

$$\delta \dot{y}_0 = -\frac{\dot{x} f_2}{f_2 \Phi_{45} - f_4 \Phi_{25}}. \tag{2.115b}$$

The variation $\partial \dot{y}_0$ is applied to obtain a new initial guess for the y component of the velocity at $t = 0$: $\dot{y}_0 = \dot{y}_0 + \partial \dot{y}_0$. The procedure is repeated until convergence (i.e., the algorithm is stopped when $\delta \dot{y}_0$ falls below a sufficiently small value). Figure 2.7 shows an example of half PLO for the Earth-Moon system around L_2. Once the initial condition for the converged PLO has been
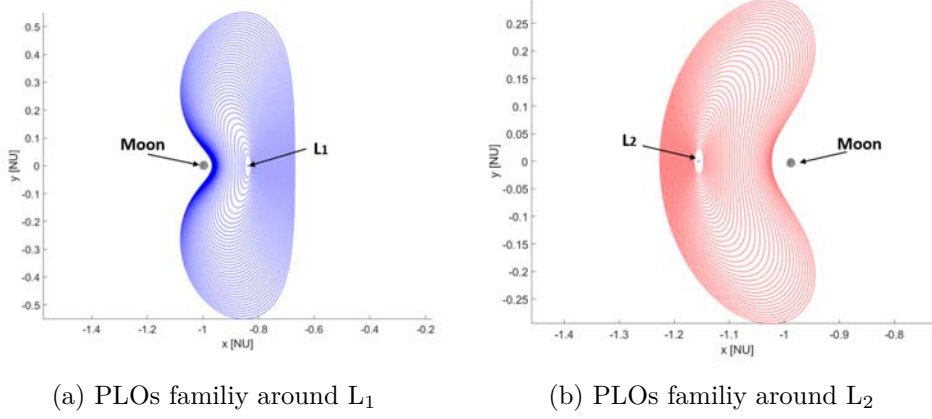
(a) PLOs familiy around L_1 (b) PLOs familiy around L_2

Figure 2.8: PLO families around L_1 and L_2 for the Earth-Moon system (Moon at $3\times$). A constant step increment $\delta x = 4e-4$ has been used 160 times each. Only one PLO every four is displayed for clarity. Notice that PLOs around L_2 are bigger than orbits around L_1.

obtained, it is possible to evaluate its period (as a consequence of periodicity, it is clearly two times the time of flight from the initial condition to the next x-axis crossing) and then, through Eq. (2.41), the value of the Jacobi constant. Eventually, we can generate a second PLO, whose initial state vector will be:

$$\mathbf{x}_0 = \left\{ x_0 + \delta x, 0, 0, 0, \dot{y}_1, 0 \right\}^{\mathrm{T}}, \qquad (2.116)$$

where δx is a small increment in the x-coordinate , $\dot{y}_1$ is the converged y velocity of the previous PLO. Its value must be small enough to prevent a possible divergence at the following step. By repeating this process, a *family* of PLOs can be generated. In Figs. 2.8a and 2.8b a family of PLOs for the Earth-Moon system around L_1 and L_2 respectively is displayed.

2.9 Invariant manifolds of equilibrium points

The topic of *manifolds* is vast, with numerous texts devoted to study their properties. In the present work, only two particular kinds of manifold are of interest, i.e., the stable and the unstable manifold. Nevertheless, we will introduce the center manifold theorem as a proof of existence of stable/unstable invariant manifold in our case of interest. To have a general idea, suppose a limit set L exists for the system (2.15), where a "limit set" might be an equilibrium point. In [Parker and Chua, 2012] the *stable* and *unstable* manifold associated with L are locally defined as follows:

Definition 1. The stable manifold $W_{\text{loc}}^{\text{S}}(L)$ of a limit set L is the set of all the $\mathbf{x}$ in the neighbourhood of L that approach L as $t \to \infty$.

Definition 2. The unstable manifold $W_{\text{loc}}^{\text{U}}(L)$ of a limit set L is the set of all the $\mathbf{x}$ in the neighbourhood of L that approach L as $t \to -\infty$.

Besides, we talk about *center manifold* when referring to the set of $\mathbf{x}$ whose behaviour is not influenced by either the attraction of the stable manifold or the repulsion of the unstable manifold. Before exploring manifolds related to the collinear points of the CR3BP, we recall here the general solution to the system (2.46) around an equilibrium point:

$$\delta\mathbf{x} = e^{\mathbf{A}(t-t_0)}\delta\mathbf{x}(t_0). \tag{2.117}$$

The eigenvalues of matrix $\mathbf{A}$ are used to identify the character of stability of the motion around the equilibrium point (see Sect. 2.6). Now, let $\mathbf{w} = \mathbf{u}_j + i\mathbf{v}_j$ be a generalized eigenvector of the matrix $\mathbf{A}$ corresponding to the eigenvalue $\lambda_j = a_j + ib_j$. Then, calling n the dimension of the space:

- $E^{\text{S}} = \text{Span}\{\mathbf{u}_j, \mathbf{v}_j | a_j < 0\}$ is called the *stable subspace* of $\mathbb{R}^n$;

- $E^{\text{U}} = \text{Span}\{\mathbf{u}_j, \mathbf{v}_j | a_j > 0\}$ is called the *unstable subspace* of $\mathbb{R}^n$;

- $E^{\text{C}} = \text{Span}\{\mathbf{u}_j, \mathbf{v}_j | a_j = 0\}$ is called the *center subspace* of $\mathbb{R}^n$;

i.e., E^s, E^u and E_c are the subspaces of $\mathbb{R}^n$ spanned by the real and imaginary parts of the generalized eigenvectors w_j corresponding to eigenvalues λ_j with negative, zero and positive real part respectively. The three subspaces fill the entire phase space

$$\mathbb{R}^n = E^s \otimes E^u \otimes E^c, \tag{2.118}$$

i.e., calling n_{S}, n_{U} and n_{C} the dimensions of the three subspaces, $n_{\text{S}} + n_{\text{U}} + n_{\text{C}} = n$. Moreover, the three subspaces are *invariant* under the flow Φ_t: if an initial condition $\mathbf{x}_0$ is contained in one of the three subspaces at $t = 0$ it will remain in that subspace for every $t \in \mathbb{R}$. As proved in Sect. 2.7, collinear libration points exhibit non-hyperbolic behaviour, in other words $n_{\text{C}} > 0$. The existence of stable/unstable as well as center manifolds is proved by the Center manifold theorem [Guckenheimer and Holmes, 1983].

Theorem 2. *(Center Manifold Theorem). Let $\mathbf{f}$ be a C^r vector field on $\mathbb{R}^n$ (i.e., it is continuous up to its rth derivative) vanishing at the equilibrium point $\mathbf{x}_{eq}$[3], so that $\mathbf{f}(\mathbf{x}_{eq}) = \mathbf{0}$ and let $\mathbf{A} = D\mathbf{f}(\mathbf{x}_{eq})$ be the Jacobian matrix in*

---

[3][Guckenheimer and Holmes, 1983] reports "vanishing at the origin". Here the origin has been shifted to the equilibrium point.

the equilibrium point. Let the stable, center and unstable invariant subspaces spanned by the eigenvalues of $\mathbf{A}$ *be* E^s, E^c *and* E^u *respectively. Then, there exist* C^r *stable and unstable invariant manifolds* W_{loc}^S *and* W_{loc}^U, *tangent to* E^s *and* E^u *at* $\mathbf{x}_{eq}$ *and a* C^{r-1} *center manifold* W^C *tangent to* E^C *tangent to* $\mathbf{x}_{eq}$. *These manifolds are all invariant under the flow of* $\mathbf{f}$.

Calling $\mathbf{v}^s$ and $\mathbf{v}^u$ the eigenvectors associated with two eigenvalues with negative and positive real parts respectively, it is possible to produce the local stable and unstable manifolds associated to the equilibrium point by introducing a small perturbation relative to the equilibrium point $\mathbf{x}_{\mathrm{eq}}$ in the direction of the corresponding eigenvalue. Thus, the step along the eigenvector is computed as

$$\mathbf{x}^{s+} = \mathbf{x}_{\mathrm{eq}} + d\frac{\mathbf{v}^s}{\|\mathbf{v}^s\|}, \tag{2.119a}$$

$$\mathbf{x}^{s-} = \mathbf{x}_{\mathrm{eq}} - d\frac{\mathbf{v}^s}{\|\mathbf{v}^s\|}, \tag{2.119b}$$

$$\mathbf{x}^{u+} = \mathbf{x}_{\mathrm{eq}} + d\frac{\mathbf{v}^u}{\|\mathbf{v}^u\|}, \tag{2.119c}$$

$$\mathbf{x}^{u-} = \mathbf{x}_{\mathrm{eq}} - d\frac{\mathbf{v}^u}{\|\mathbf{v}^u\|}, \tag{2.119d}$$

where d may be interpreted as a small distance away from the equilibrium point. If d is too large, the perturbation is not a close approximation to the state that actually exists along the manifold. Should d be too small, long integration times are required to globalize the manifolds, due to their asymptotic nature, leading to accumulation of numerical error. The local stable and unstable manifold are globalized by numerically propagating the states defined in Eqs. (2.119) with the equations of the CR3BP backward and forward in time respectively. This is qualitatively outlined in Fig. 2.9.

2.10   Poincaré maps and sections

Poincaré maps (also called *first-return maps*) were first introduced by Henry Poincaré to study the stability of periodic orbits [Perko, 2013, Poincaré, 1882]. Nowadays, they are a useful tool in the analysis and visualization of dynamical systems as they evolve. Consider an autonomous n-dimensional continuous system

$$\dot{\mathbf{x}} = \mathbf{f}(\mathbf{x}), \tag{2.120}$$

where for the CR3BP $n = 6$. Recall that the flow Φ_t is defined by $\mathbf{f}$ such that $\Phi_t(\mathbf{x}) = \Phi(\mathbf{x}, t)$ is smooth and $\frac{d}{dt}(\Phi_t(\mathbf{x}, t))|_{t=\tau} = \mathbf{f}(\Phi(\mathbf{x}, t))$. Define
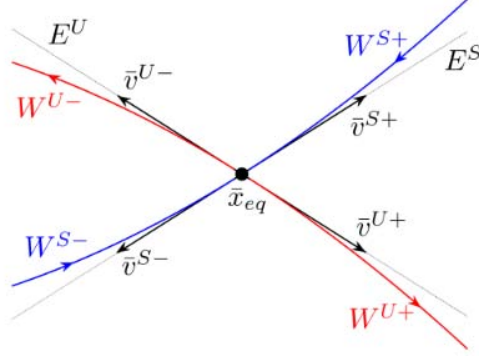
Figure 2.9: Global stable and unstable manifold of an equilibrium point of the CR3BP. Signs $+$ and $-$ refer to the direction of the perturbation in Eqs. (2.119). The black arrows represent the stable and unstable eigendirections. The dotted black lines represent the stable and unstable subspaces E^{s} and E^{u} which are parallel to the corresponding eigenvectors and approximate W_{loc}.

$\Sigma_1 \in \mathbb{R}^n$ ans $\Sigma_2 \in \mathbb{R}^n$ as $(n-1)$-dimensional hypersurfaces (also called *surfaces of section* or *Poincaré sections*) that represent cross sections of the dynamical flow Φ_t. A Poincaré map P is a mapping from one surface of section to another one, i.e., $P : \Sigma_1 \to \Sigma_2$ [Villac and Scheeres, 2003]. The hypersurfaces are often selected such that $\Sigma_1 = \Sigma_2$: in this case the Poincaré map is a mapping of subsequent intersections with one hypersurface. Traditional Poincaré sections are defined as planes in position space (for example $\Sigma = \{\mathbf{x} : x = \mu - 1, z = 0\}$) but they can be any surface in general. An example of a Poincaré map is reported in Fig. 2.10 for a periodic solution γ^* of minimum period T for the system (2.16) that possesses a state $\mathbf{x}^*$ located along the trajectory. In this case $\Phi_t(\mathbf{x}^*, t) = \Phi_{t+T}(\mathbf{x}^*, t_0)$ and $\mathbf{x}^*(t_0) = \mathbf{x}^*(t_0 + T)$. Hence, γ^* in Fig. 2.10 represents a periodic orbit that intersect Σ always in the same point $\mathbf{x}^* \in \Sigma$, being $P(\mathbf{x}^*) = \mathbf{x}^*$. The point $\mathbf{x}^*$ is defined *fixed point* [Parker and Chua, 2012]. A small perturbation from the initial state $\mathbf{x}^*$ to the state $\mathbf{x}_1$ will result in a mapping $P(\mathbf{x}_1) \neq \mathbf{x}_1$ as showed in Fig. 2.10. Poincaré maps can be employed to visualize periodic orbits in the neighbourhood of equilibrium points., i.e., to visualize the center manifold associated with the point itself. In Fig. 2.11 an example is reported for the point L_1 of the Earth-Moon system at four different energy levels. The exterior curve in each plot is the PLO with the prescribed energy. For energies close to that of the equilibrium point, the map is composed by the Lissajous intersections surrounding the vertical Lyapunov orbit. Halo orbits
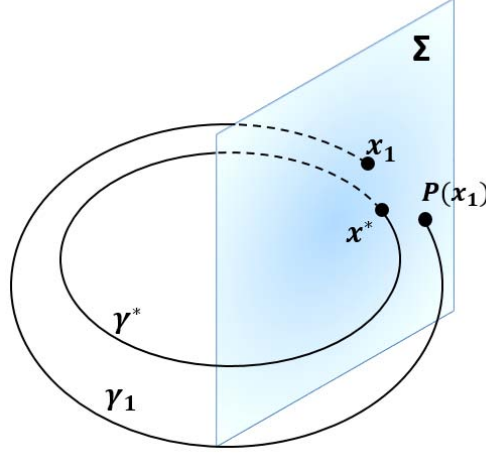
Figure 2.10: The Poincaré section Σ is used to map the initial states $\mathbf{x}^*$ and $\mathbf{x}_1$ using the Poincaré map $P : \Sigma \rightarrow \Sigma$. For a periodic orbit $P(\mathbf{x}^*) = \mathbf{x}^*$.

appear at a specific energy level ($J = 3.15$ in this case). Like the vertical Lyapunov orbit, they are also surrounded by other trajectories, the quasi-halo orbits.

2.11 Invariant manifolds for periodic orbits

Let us assume that a certain periodic orbit Γ of period T exists around an equilibrium point of the system (2.16):

$$\Gamma : \mathbf{X} = \gamma(t), \quad 0 \leq t \leq T \tag{2.121}$$

in which the time interval T is the minimum period corresponding to Γ. For such an orbit, the same state occurs after the period T, i.e., $\Gamma(t_0+T) = \Gamma(t_o)$, or equivalently $\mathbf{x}(t_0) = \mathbf{x}(t_0) = \mathbf{x}(t_0 + T)$. Thus, a periodic orbit may be entirely represented by any point along the orbit. In particular, consider the mapping $P : \Sigma \rightarrow \Sigma$ that maps the state from $\mathbf{x}(k)$ at the time nT to $\mathbf{x}(k+1)$ at the time $(n + 1)T$, where $k = nT$, $k + 1 = (n + 1)T$, $n \in \mathbb{Z}$. From this mapping, Γ appear as a single fixed point $\mathbf{x}(nT) = \mathbf{x}((n + 1)T) = \mathbf{x}^*$ on the map P. Then, the map can be linearised relative to x^*:

$$\delta\mathbf{x}(k + 1) = DP(\mathbf{x}^*)\delta\mathbf{x}(k). \tag{2.122}$$

Equation (2.122) is a discrete time representation of the evolution of solutions in the vicinity of $\mathbf{x}$. The matrix $DP(\mathbf{x}^*)$ is the STM corresponding
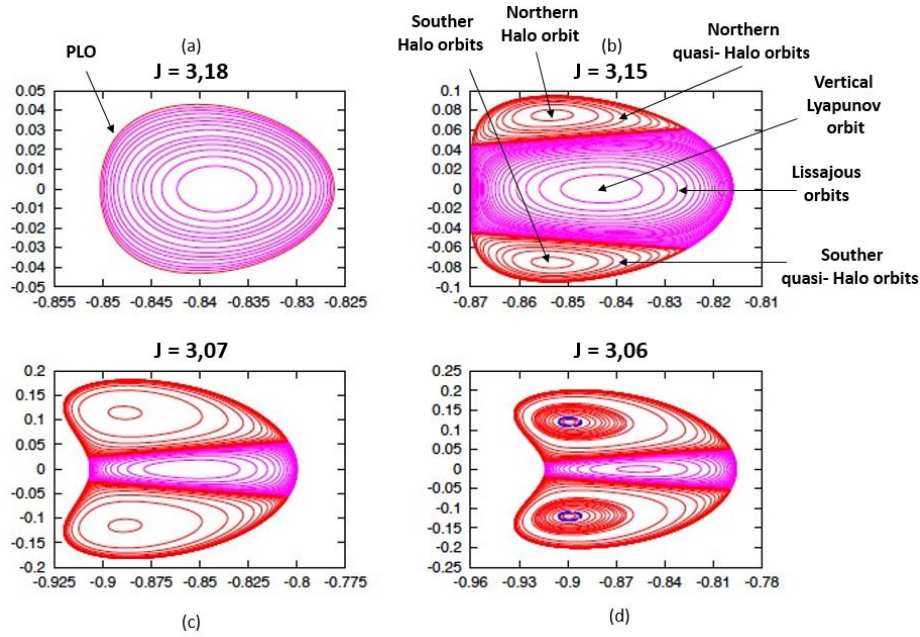
Figure 2.11: Poincaré map representation of the center manifold associated to L_1 for different Jacobi constants in the Earth-Moon CR3BP (adapted from [Gómez and Mondelo, 2001]).

to one period along the orbit, i.e., $DP(\mathbf{x}^*) = \Phi(T, 0)$. This matrix is called *monodromy matrix*. By means of the *Floquet's theorem* [Floquet, 1883], we can relate this matrix to the stability of the orbit itself. In particular, the above mentioned theorem allows to rewrite the STM as:

$$\Phi(t) = Z(t)e^{Rt}, \qquad (2.123)$$

where R and Z are square matrices with the same dimension as A, R is constant and Z is non-singular, differentiable and periodic with period T. Being $\Phi(0) = I$ then $Z(0) = I$. The eigenvalues of R are called *characteristic exponents* of Γ, the eigenvalues of the matrix e^{Rt} are called *characteristic multipliers* of Γ. We then define the *monodromy matrix* M as:

$$M = \Phi(T), \qquad (2.124)$$

The monodromy matrix is the STM after one period of Γ. Applying the theorem of Floquet to M provides:

$$M = \Phi(T) = Z(T)e^{Rt} = Z(0)e^{Rt} = e^{Rt}. \qquad (2.125)$$

Therefore, the monodromy matrix allows to determine the characteristic multipliers of Γ that correspond to the eigenvalues of M. Lyapunov's theo-

rem [Burton, 1966] states that if λ is an eigenvalue of the monodromy matrix then λ^{-1} is also an eigenvalue. Moreover, the monodromy matrix associated with any periodic solution possesses at least one unit eigenvalue [Steves et al., 2006]. Hence, as a consequence of Lyapunov's theorem, two eigenvalues are equal to 1.

The behaviour of the manifold is determined by the eigenvectors of M $\mathbf{w}_i = \mathbf{u}_i + i\mathbf{v}_i$ associated with the eigenvalues $\lambda_i = a_i + ib_i$. In a similar way to the previous section for equilibrium points we define:

- the *stable subspace*: $E^s(\Gamma) = \{\mathbf{u}_j, \mathbf{v}_j | a_j < 0\}$;

- the *unstable subspace*: $E^u(\Gamma) = \{\mathbf{u}_j, \mathbf{v}_j | a_j > 0\}$;

- the *center subspace*: $E^s(\Gamma) = \{\mathbf{u}_j, \mathbf{v}_j | a_j = 0\}$.

Besides, the local stable $W^s_{loc}(\Gamma)$ and unstable $W^u_{loc}(\Gamma)$ manifolds of Γ are defined respectively as:

$$W^s_{loc} = \{x \in U | \Phi_t \to \Gamma \text{ for } t \to +\infty \text{ and } \Phi(t) \in U \ \forall \ t \geq 0\}, \qquad (2.126)$$
$$W^u_{loc} = \{x \in U | \Phi_t \to \Gamma \text{ for } t \to -\infty \text{ and } \Phi(t) \in U \ \forall \ t \geq 0\}, \qquad (2.127)$$

being U a neighbourhood of Γ and ϕ_t the flow of the equations of the motion of the dynamical system. Then, we define the stable and unstable *global manifolds* as:

$$W^s(\Gamma) = \bigcup_{t \leq 0} \phi_t(W^s_{loc}(\Gamma)), \qquad (2.128)$$

$$W^u(\Gamma) = \bigcup_{t \geq 0} \phi_t(W^u_{loc}(\Gamma)). \qquad (2.129)$$

In other words:

- The global stable manifold is the locus of points that tends asymptotically to the periodic orbit in the future, for $t \to +\infty$.

- The global unstable manifold is the locus of points that tends asymptotically to the periodic orbit in the past, for $t \to -\infty$.

Besides, each manifold is invariant under the flow Φ_t.

2.12 Computation of the invariant manifolds of a periodic orbit

In this section we provide a practical recipe for the computation of stable and unstable IMs associated with a PLO around a libration point.

1. Numerically propagate the orbit within N discretized of points (preferably equally spaced in time); $\mathbf{x}_i = \mathbf{x}(t_i)$ represent the state at the time t_i $(i = 1, \ldots, N)$ and $\mathbf{x}_1$ represents the state corresponding to the time $t = T$, being T the period of the PLO.

2. From the monodromy matrix, compute the characteristic multipliers of Γ, and their corresponding eigenvectors. The eigenvector $\mathbf{v}^s(\mathbf{x}_1)$ associated with the positive real eigenvalue gives the direction of the stable manifold, whereas the eigenvector $\mathbf{v}^u(\mathbf{x}_1)$ associated with the negative real eigenvalue is related to the unstable manifold of Γ.

3. Since the eigenvectors represent a variation from the local state, their evolution at time t with respect to $t_0 = T$ can be computed through the STM. Therefore, for the ith point of the periodic orbit, compute the stable and unstable eigendirection by multiplying the local STM by $\dfrac{\mathbf{v}^s(\mathbf{x}_1)}{\|\mathbf{v}^s(\mathbf{x}_1)\|}$ and $\dfrac{\mathbf{v}^u(\mathbf{x}_1)}{\|\mathbf{v}^u(\mathbf{x}_1)\|}$ respectively:

$$\mathbf{v}_i^s = \Phi(t_i, T)\frac{\mathbf{v}^s(\mathbf{x}_1)}{\|\mathbf{v}^s(\mathbf{x}_1)\|}, \tag{2.130}$$

$$\mathbf{v}_i^u = \Phi(t_i, T)\frac{\mathbf{v}^u(\mathbf{x}_1)}{\|\mathbf{v}^u(\mathbf{x}_1)\|}, \tag{2.131}$$

where the subscript i refers to the eigenvector corresponding to the state $\mathbf{x}_i$.

4. Using the directions computed in the previous step, apply a small perturbation $\epsilon \approx 10^{-6}$ to jump locally from the periodic orbit to the stable/unstable manifold:

$$\mathbf{x}_i^s = \mathbf{x}(t_i) \pm \epsilon \mathbf{v}^s(\mathbf{x}_1), \tag{2.132}$$

$$\mathbf{x}_i^u = \mathbf{x}(t_i) \pm \epsilon \mathbf{v}^u(\mathbf{x}_1). \tag{2.133}$$

This is qualitatively represented in Figs. 2.12a. Each manifold thus has two *branches*, each identified by one of the two signs in Eq. (2.132) (see Fig. 2.12b). There is not direct correspondence between the sign used in Eqs. (2.132) and the effective direction of propagation of the global manifold, since it depends on the energy level of the PLO. In other words, if for a given Jacobi constant J_1 the branch corresponding to $+\epsilon$ propagates towards P_2 for another $J_2 \neq J_1$ the resulting manifold may propagate in the opposite direction.
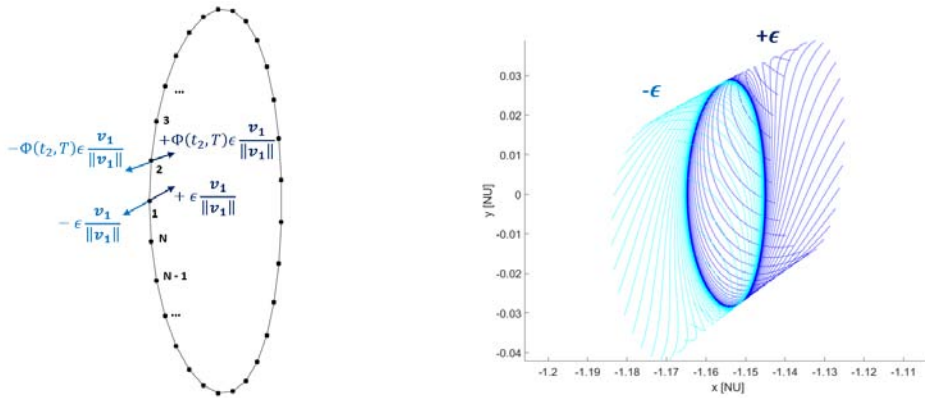
(a) Positive and negative eigendirections calculated at the first and second point of the numerically integrated PLO. The dimensions of the vectors are here exaggerated for the sake of clarity.

(b) Globalization of IMs with the two branches corresponding to $+\epsilon$ and $-\epsilon$.

Figure 2.12: Example of two IM branches.

5. Globalize the manifold by integrating each initial state found at the previous step for a given time or until the intersection with a given Poincaré section.

6. Repeat steps 2, 3, 4, 5 for $i = 1, \ldots, N$.

The complete sets of stable and unstable IMs corresponding to each fixed point along the PLO are often called manifold *tubes*. This descriptor originates from the appearance of IMs projection onto position space; however, these structures exist in the higher six-dimensional space and cannot be precisely defined as three-dimensional objects. When working with the planar CR3BP, IMs become four-dimensional object, since the z component of position and velocity is not considered.

Some examples are provided in Fig. 2.13 for the collinear points L_1 and L_2 in the Earth-Moon system for the planar CR3BP. For some energy levels and depending on the radius of P_2, such as in Fig. 2.13a, the manifold tube could impact the smaller primary. Notice how the IMs tend to fold around P_2 inside the inner region.
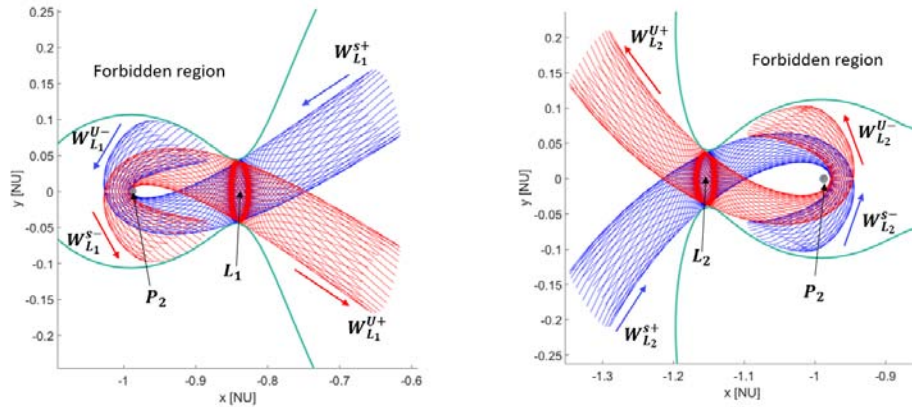
(a) IMs originating from PLO around Earth-Moon L_1. $J = 3.18067$, propagation time: 23.05 days.

(b) IMs originating from PLO around Earth-Moon L_2. $J = 3.19238$, propagation time: 17.39 days.
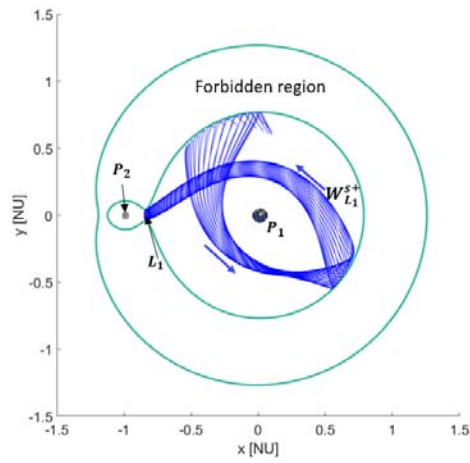
(c) Stable IM originating from PLO around Earth-Moon L_2. $J = 3.19238$, propagation time: 38.26 days.

Figure 2.13: Different morphologies of IMs originating from PLOs around L_1 and L_2 points of the Earth-Moon system.
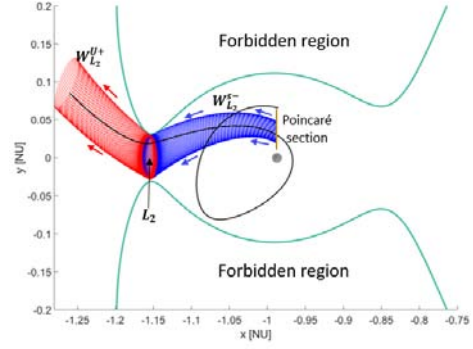
2.13   Transit orbits

A key feature of the IMs of PLOs is that they act as separatrices for the flow through the equilibrium region, i.e., they separate two distinct types of motion: *transit* orbits (TOs), which moves inside the manifold tubes, and *non-transit* orbits, which are those outside the tubes [Gómez et al., 2004, Koon et al., 2001, Corrêa et al., 2004, Conley, 1968]. Moreover, only TOs can travel between the interior and the exterior region, thus controlling the transport of material to and from the L_2 bottleneck. In Fig. 2.14 examples of transit and non-transit orbits are provided for the Earth-Moon planar CR3BP. A stable IM has been integrated from a PLO with the same Jacobi constant J around L_2 until the Poincaré section $\Sigma = \{\mathbf{x} : x = \mu - 1\}$, where the components $(y, \dot{y})$ are determined (see Figs. 2.14a, 2.14c). Initial conditions for the TO are obtained by taking a point inside the stable manifold cut (as showed in Fig. 2.14a) and then selecting the component $\dot{x} = \dot{x}(y, \dot{y}, J)$, by means of Eq. (2.41):

$$\dot{x} = \sqrt{x^2 + y^2 + \frac{2(1-\mu)}{r_1} + \frac{2\mu}{r_2} + \mu(1-\mu) - \dot{y}^2 - J} \qquad (2.134)$$

being J the Jacobi constant of the corresponding stable IM. By propagating this state forward in time, a TO travelling inside the IM is generated. As showed in Fig 2.14b, the TO is inside the planar projection of the stable IM represented in blue until it reaches the PLO region, then it continues inside the unstable IM represented in red. As a consequence, all TOs will pass inside the region defined by the PLO itself. Similarly, taking an initial condition just outside the manifold cut (Fig. 2.14c) leads to a non-transit orbit, i.e., one which do not access the exterior region but loops back towards P_2.
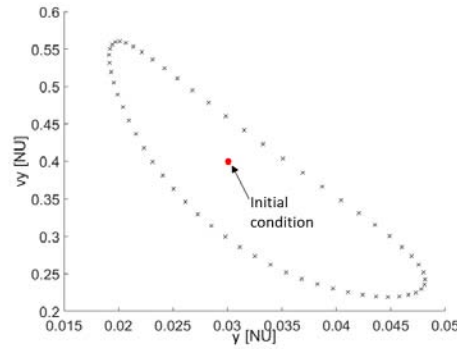
(a) Poincaré section and initial condition for transit orbit

(b) Transit orbit
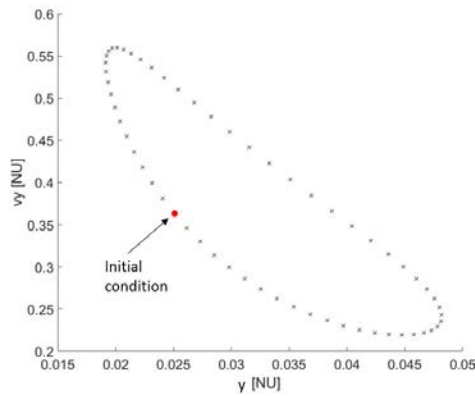
(c) Poincaré section and initial condition for non-transit orbit
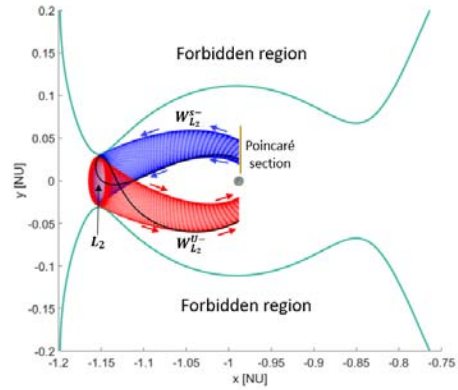
(d) Non-transit orbit

Figure 2.14: Examples of TOs for the Earth-Moon planar CR3BP ($J = 3.182003$). On the left the Poincaré sections of the stable manifold and the initial condition chosen to generate a transit or non-transit orbit. On the right, these Poincaré sections are depicted as a gold line and the corresponding transit/non-transit orbits are represented in black. We observe that for the non-transit orbit the initial condition has been chosen just at a small distance from the boundary of the manifold cut. $W_{\mathrm{L}_2}^{S-}$, $W_{\mathrm{L}_2}^{U-}$, $W_{\mathrm{L}_2}^{U+}$ represent the stable IM in the inner region, the unstable IM in the inner region and the IM in the outer region, respectively.

Chapter 3

Model and method

Introduction. In this chapter the method to find trajectories connecting consecutive moons of a planetary system is introduced. Two physical models are used: the CR3BP is employed to study the dynamics of the spacecraft in the vicinity of the moons (intra-moon space) while the two body approximation is used in the inter-moon space between them, by considering the sole gravity of the larger primary. The geometry of the problem and the definition of the boundary between the intra-moon space and the inter-moon space is described in Sect. 3.1. We use two different approaches for trajectory propagation inside the intra-moon space, i.e., by means of TOs and IMs (Sect. 3.2). The method to identify possible connections in the inter-moon space is described in Sect. 3.3. An application to a transfer between Europa and Ganymede (and viceversa) is reported in Sect. 3.4. The analysis of the results follows in Sect. 3.5.

3.1 Moon-to-moon connections: the approach

In the present work we aim at finding low-energy transfers (i.e., conceived in the framework of the CR3BP) between consecutive moons of a planetary system. Such connections are carried out by propagating low-energy trajectories in the neighbourhood of each moon towards the other moon and identifying the intersections between couple of trajectories. The purpose is to evaluate the minimum-cost connection, being the cost the difference in velocity in the intersection between two trajectories. These trajectories are generated as IMs or TOs and propagated in the so called *coupled* CR3BP [Koon et al., 2008, Castelli, 2012] according to which there is no influence between the two CR3BPs involved from a dynamical viewpoint, being their relationship merely kinematical. The coupling is made by the appropri-
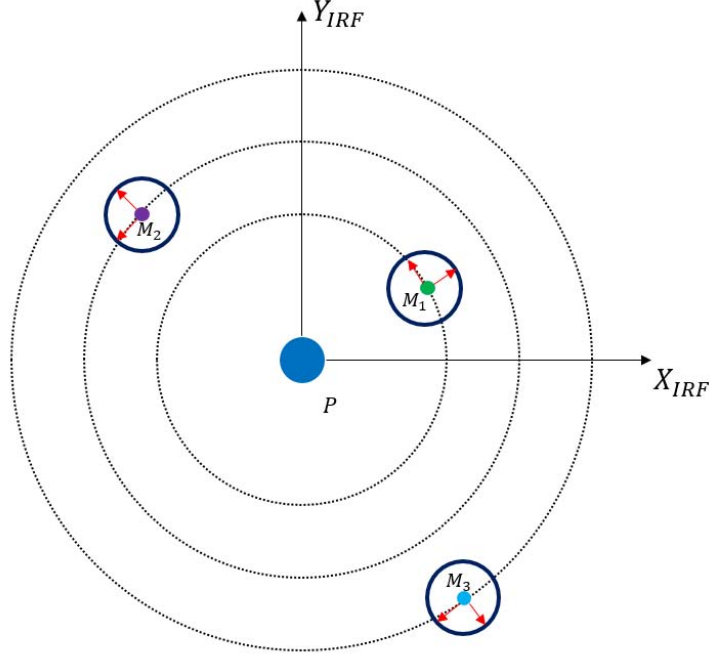
Figure 3.1: A planetary-system with three moons (M_1, M_2, M_3) orbiting around a planet P. The planet-centered IRF is represented in black, while the SRFs of each moon are represented in red (the x-axes are in the direction of the vector connecting the planet to the moon). The intra-moon space is defined by the regions inside each CI (represented in blue), where the CR3BP is used. Outside, defining the inter-moon space, the two-body approximation is adopted. The orbits of the moons are assumed circular, one of the conditions for the applicability of the CR3BP.

ate transformation of coordinates between the two SRFs of two consecutive moons. In the quoted papers the two restricted models are directly connected, i.e., the phase states (position and velocity vectors) in one synodical frame are converted into phase states in the other synodical frame when a given Poincaré section is reached. In this work, however, the space where the CR3BP is used is limited to circular regions (whose borders are called *circles of influence* (CIs)) around each moon: we call these regions the *intra-moon* space; in the remaining space, called *inter-moon space* the two-body model is adopted (see Fig. 3.1). In other words, each connection between two consecutive moons implies a intra-moon branch inside the CI of the first moon, two inter-moon branches where the intersection takes place, and a final intra-moon branch inside the CI of the second moon. The coordinate system adopted when describing the inter-moon dynamics is the planet-centered

IRF[1]. In order to perform the coupling, a coordinate change is applied from each SRF to the planet-centered IRF at the boundary between the inter-moon and intra-moon space, i.e., at the CI. This transformation requires a translation from the barycentre of the planet-moon system to the centre of the planet and a rotation about the z-axis by the angle between the x-axes of the SRF and the X-axis of the IRF. However, in this work we ignore the first translation, being the centre of mass of the planet-moon system within a negligible distance from the centre of the planet in the majority of real cases (for example, each planet-moon barycentre of the Galilean moons is three to six orders of magnitude smaller than the radius of Jupiter). The overall coupling between two moons depends on the angle swept by the x-axis of the SRFs with respect to the X-axis of the IRF. However, we choose to orient the IRF so that one of the two x-axes coincides with the inertial X-axis at $t = 0$: this allows to remove the dependence on one of the two angles. Therefore, the transformation has just one degree of freedom, represented by the relative phase α_0 between the two x-axes at $t = 0$, as sketched in Fig. 3.2 for two consecutive moons of a planetary system. Moreover, since the angular velocities of the moons are constant, we can choose the angle α_0 at any fixed time to completely parametrise the model. We can use this parameter to map all the possible relative orientations between two moons in search for the optimal trajectory which links them.

Regardless the method to propagate the trajectories in the intra-moon space (i.e., IMs or TOs), the procedure to connect two points in the CIs of two consecutive moons in the inter-moon space is the same. The method exploiting IMs is the same developed in [Fantino and Castelli, 2016a]; we derive the algorithm for the inter-moon connection from the same paper. The procedure with TOs is introduced as a possible enhancement to the previous one. The results of the two methods are then compared and discussed.

3.2 Motion in the intra-moon space

An outward connection between two moons by means of IMs is conceived as a trajectory leaving a PLO around P_2 of the inner moon through the unstable manifold and approaching a PLO around P_1 of the outer moon through the stable manifold. Similarly, an inward connection is intended as a trajectory leaving a PLO around P_1 of the outer moon through the

---

[1]To be precise, this frame is more generally a planet-centered fixed axes frame. In fact, in some application (e.g., Jupiter and the Galilean moons), the origin is accelerated, being the planet itself in circular motion around another body (e.g., the Sun in the case of Jupiter).
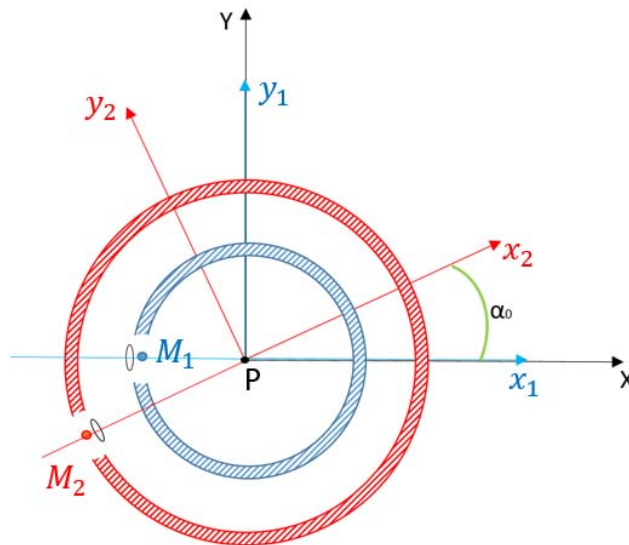
Figure 3.2: The coupled CR3BP for two consecutive moons M_1 and M_2 in circular motion around the planet P at constant angular velocity. The plot outlines the coupling at the time $t = 0$, with the x_1-axis aligned with the inertial X-axis. The angle α_0 between the two SRFs parametrises the model. For the sake of illustration, the forbidden region corresponding to the value of the Jacobi constant for two PLOs around P_1 or P_2 is represented.

(a) Stable IM.
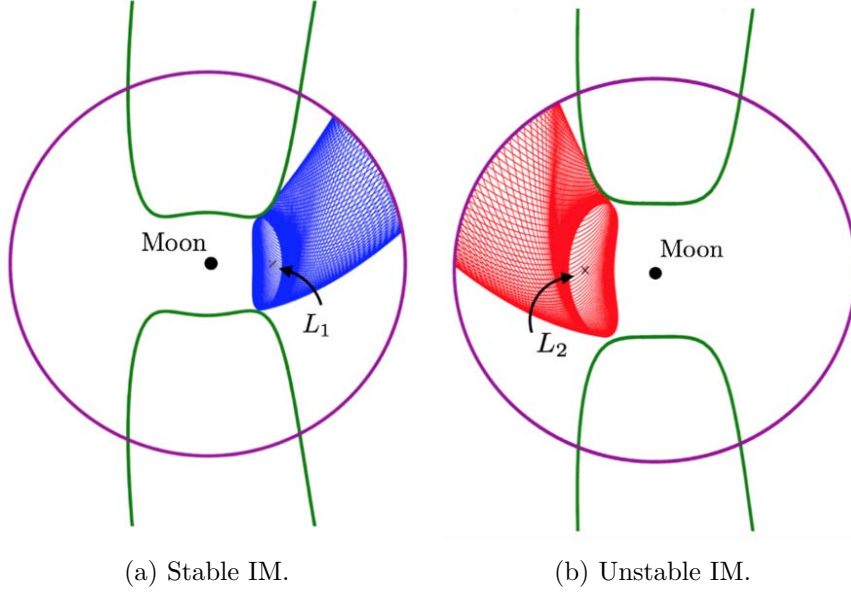
(b) Unstable IM.

Figure 3.3: Stable and unstable IMs originating from a PLO around P$_1$ (left) and P$_2$ (right), integrated until the CI (represented in purple). The ZVCs are represented in green.

unstable manifold and approaching a PLO around P$_2$ of the inner moon through the stable manifold. PLOs are varied according to a certain energy discretization, leading to a database to be used in the trajectory design. The intra-moon space, where the CR3BP is used, is defined by the radius of the CI. We define this radius r_{CI} for a given moon as the radius of the Laplace sphere [Roy, 2004] multiplied by a convenient factor k:

$$r_{CI} = kr_0 \left(\frac{m}{M} \right), \tag{3.1}$$

being r_0 the orbital radius of the moon, m its mass and M the mass of the planet. The value of k is selected in such a way that it contains, with due margin, all the Lyapunov orbits of the database. For each PLO of the database, the corresponding stable (or unstable) IM is propagated until intersection with the CI using the method described in Sect. 2.12 (see Fig. 3.3). The phase states collected on the CIs are transformed to the planet-centered IRF and considered as initial conditions for backward/forward propagation.

In the case of the TOs, instead of leaving/approaching the PLO, the trajectory passes through it (Sect. 2.13). For this reason, we select initial
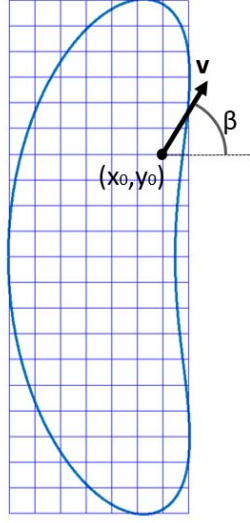
Figure 3.4: 8×21 grid around a PLO. Only points (x_0, y_0) inside the Lyapunov orbit are selected as initial conditions for trajectory propagation. The components $(\dot{x}_0, \dot{y}_0)$ of the velocity vector **v** are selected through Eq. (3.2) for a given angle β.

conditions for the TOs directly inside the area enclosed by each PLO of the database by means of a $n_X \times n_Y$ grid (see Fig. 3.4). Since each PLO is computed numerically as a set of points, an analytical representation of the PLO is needed to distinguish between points inside or outside the grid: this is obtained by approximating the PLO through a parametric cubic spline (see Appendix D). Only points inside the grid are selected as initial positions. For a given position (x_0, y_0) and a value of the Jacobi constant J, the magnitude of the initial velocity is constrained by Eq. (2.41):

$$ v = \sqrt{\dot{x}^2 + \dot{y}^2} = \sqrt{x^2 + y^2 + \frac{2(1-\mu)}{r_1} + \frac{2\mu}{r_2} + [\mu(1-\mu)] - J}. \qquad (3.2) $$

Therefore, once selected an angle β (see Fig. 3.4) between the velocity direction and the positive x-axis, the velocity components of the initial state $\dot{x}_0$ and $\dot{y}_0$ are given by:

$$ \begin{cases} \dot{x} = v \cos \beta, \\ \dot{y} = v \sin \beta, \end{cases} \qquad (3.3) $$

where $\beta \in [0, 2\pi[$. We call n_β the number of angles in which the range $[0, 2\pi[$ is discretized. A given initial state for a TO is therefore a function of the position (x_0, y_0) on the grid, the Jacobi constant J and the angle β. Varying

the position on the grid and the remaining two parameters permits to define a set of initial states $(x_0, y_0, \dot{x}_0, \dot{y}_0)$ to be integrated by means of Eqs. 2.15 until intersection with the CI. Eventually, the phase states at the CI are converted from the SRF to the planet-centered IRF using the transformation presented in Sect. 2.1.

3.3 Motion in the inter-moon space

The two-body approximation in the planet-centered IRF substitutes the CR3BP when dealing with the spacecraft's dynamics beyond the CI, i.e., in the inter-moon space. The initial states on the CI expressed in the planet-centered IRF are used as initial conditions for backward/forward Keplerian orbit propagation. No matter the time direction, these Keplerian orbits are ellipses with a focus on the planet's centre. Any Keplerian orbit can be parametrised by means of the five classical orbital elements, i.e., the semi-major axis a, the eccentricity e, the inclination i, the right ascension of the ascending node Ω, the argument of periapsis ω. Additionally, the true anomaly indicates the geometric position along the ellipse. In planar approximation, however, the inclination and the right ascension of the ascending node are irrelevant, therefore ω is measured from the X-axis to the periapsis of the ellipses and the so-called *Keplerian elements set* just consists of a, e, ω and θ (see Fig. 3.5). The semimajor axis and the eccentricity provide the shape of the ellipse, and as such are fixed for a given state on the CI. The argument of periapsis depends only on the relative orientation between the x-axis with the XY-plane at the given time. In other words, a change $\Delta\alpha$ in the orientation of the SRF produces an equivalent change $\Delta\omega = \Delta\alpha$ of the argument of periapsis of the resulting ellipse. For a proof see Appendix C.

Given two moons, the procedure to find possible connections is now presented. For a choice of two PLOs, one on each CR3BP, IMs and TOs are integrated with the method described in the previous section. For a choice of α_0 the phase states are collected on the two CIs and converted into Keplerian elements sets. Connections between moons are then sought by looking at the geometrical intersections between all the possible combinations of ellipses from the two CIs. Consider now the generic Cartesian implicit equation for an ellipse:

$$ax^2 + bxy + cy^2 + dx + ey + f = 0. \tag{3.4}$$

Dividing the left and right-hand side of Eq. (3.4) by f, it turns out that a generic ellipse is a function of five parameters. If we fix the coordinates of the focus, two of these five parameters can be written as some functions f_1 and f_2 of the remaining ones. In other words, an ellipse $\mathcal{E}_1$ with a fixed focus
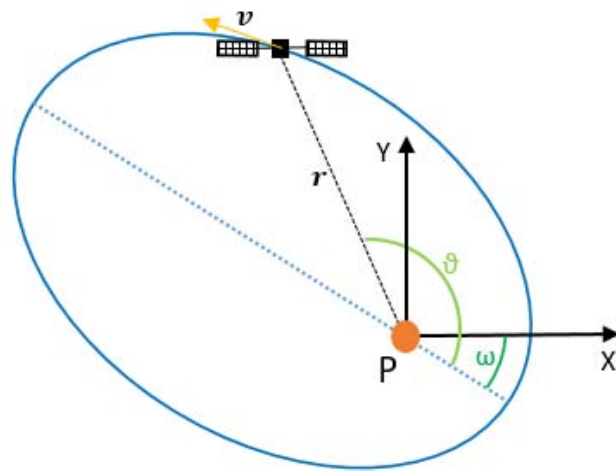
Figure 3.5: An elliptical orbit with a focus on the planet P. Its orientation with respect to the IRF (represented in black) is defined by the argument of periapsis ω, i.e., the angle between the inertial X-axis and the periapsis of the ellipse. The position $\mathbf{r}$ and the velocity $\mathbf{v}$ of a point with true anomaly θ are also shown.
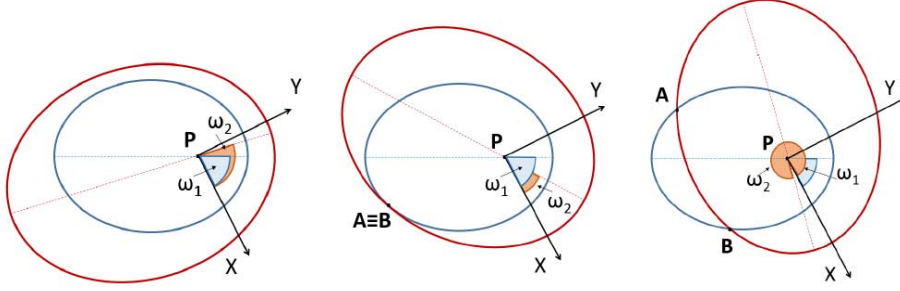
Figure 3.6: Possible intersections between two ellipses sharing the same focus: none, two identical ($A \equiv B$), two distinct $A \neq B$, respectively on the left, center, right.

can be written as a function of three parameters:

$$a_1 x^2 + b_1 xy + c_1 y^2 + f_1(a_1, b_1, c_1)x + f_2(a_1, b_1, c_1). \tag{3.5}$$

If we know three different points A_1, A_2 and A_3 of $\mathcal{E}_1$, a unique set of a_1, b_1 and c_1 defining $\mathcal{E}_1$ can be found. Suppose another ellipse $\mathcal{E}_2$ shares the same focus of $\mathcal{E}_1$; its Cartesian equation becomes:

$$a_2 x^2 + b_2 xy + c_2 y^2 + f_1(a_2, b_2, c_2)x + f_2(a_2, b_2, c_2). \tag{3.6}$$

If $\mathcal{E}_2$ intersects $\mathcal{E}_1$ in A_1 A_2 and A_3, then $a_1 = a_2$, $b_1 = b_2$, $c_1 = c_2$ and $\mathcal{E}_1$ coincides with $\mathcal{E}_2$. Therefore, the maximum number of intersection between two different ellipses sharing the same focus is two. In case of one solution the two ellipses are tangent. All the possible situations are represented in Fig. 3.6.

   If an intersection between two ellipses exist, the magnitude ΔV of the difference in velocity at the intersection point is the magnitude of the impulse to be applied by the propulsion system of the spacecraft to change from one orbit to another and eventually accomplish the task of connecting the two CR3BPs. If more than one intersection exists, two possible paths connecting the two moons are available, and the ΔVs at the two intersections are different. Figure 3.7 shows two ways to connect the CIs of two moons by means of the two paths provided by intersections A and B. This procedure should be repeated for all the PLOs of the database in each CR3BP and requires varying α_0 from 0 to 2π according to some discretization. Comparing all the possible combinations of ellipses allows to find the initial conditions providing the minimum-ΔV. This may become time-consuming if the resolution taken to discretize the angle α_0, the individual PLO (or the related grid, in case of TOs) and the energy level of the Lyapunov family is narrow.
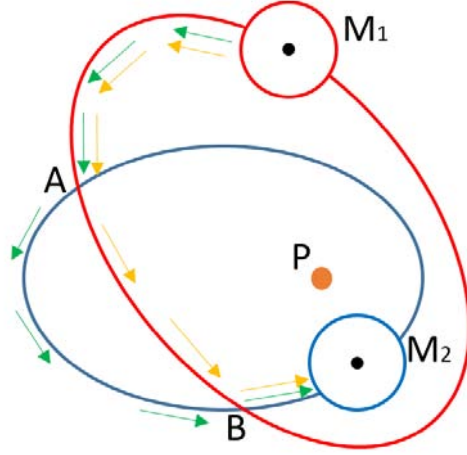
Figure 3.7: Two possible paths (indicated with orange and green arrows) from the CI of moon M_1 to the CI of moon M_2 through the intersections A and B, respectively. The two ellipses share the same focus, represented by the planet P.

However, a closer look allows to simplify the problem and, in turn, reduce the amount of computations. We start by writing the polar equation of the ellipse, providing the distance r of the spacecraft to the focus as a function of the true anomaly θ:

$$r = \frac{p}{1 + e \cos \theta}, \tag{3.7}$$

being $p = a(1 - e^2)$ the *semilatus rectum* of the ellipse. At the intersection points A and B between two ellipses defined by the orbital sets (a_1, e_1, ω_1) and (a_2, e_2, ω_2) (see Fig. 3.8), the orbit equations can be written as:

$$r = \frac{p_1}{1 + e_1 \cos \theta_1}, \tag{3.8a}$$

$$r = \frac{p_2}{1 + e_2 \cos \theta_2}, \tag{3.8b}$$

in which r is the distance of the intersection from the planet, θ_1 and θ_2 are the true anomalies of the intersection point, calculated from the apse lines given by ω_1 and ω_2, respectively. The angular displacement between the two apse lines is

$$\Delta\omega = \theta_2 - \theta_1, \tag{3.9}$$

hence

$$\cos(\theta_2) = \cos(\theta_1 + \Delta\omega) = \cos\theta_1 \cos\Delta\omega - \sin\theta_1 \sin\Delta\omega. \tag{3.10}$$
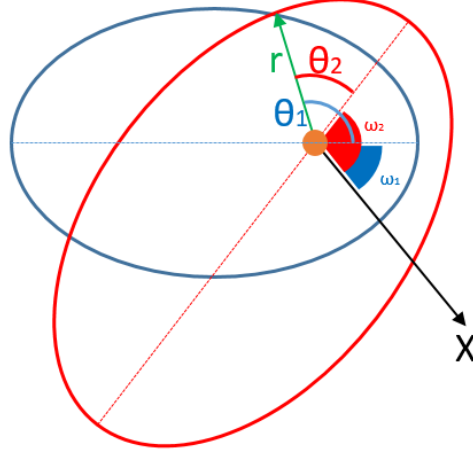
Figure 3.8: Intersection point between two ellipses sharing the same focus. The radius r is the same in this point, while the true anomalies θ_1 and θ_2 vary according with the two argument of perigee ω_1 and ω_2 (referred to the inertial X-axis).

From Eqs. (3.8) and (3.10) it follows

$$p_1 - p_2 + \cos\theta_1 \left[p_1 e_2 \cos\Delta\omega - p_2 e_1\right] = \sin\theta_1 (p_1 e_2 \sin\Delta\omega) \qquad (3.11)$$

or, in a more compact form

$$k_1 + k_2 \cos\theta_1 = k_3 \sin\theta_1, \qquad (3.12)$$

where we made the substitutions:

$$k_1 = p_1 - p_2, \qquad (3.13a)$$
$$k_2 = p_1 e_2 \cos\Delta\omega - p_2 e_1, \qquad (3.13b)$$
$$k_3 = p_1 e_2 \sin\Delta\omega. \qquad (3.13c)$$

Squaring both the members of Eq. (3.12) and rearranging yields:

$$(\cos\theta_1)_{1,2} = \frac{-k_1 k_2 \pm |k_3|\sqrt{k_3^2 + k_2^2 - k_1^2}}{k_2^2 + k_3^2}. \qquad (3.14)$$

The values found in Eq. (3.12) are the cosines of the true anomalies of A and B measured from the apse line given by ω_1. Solutions exist and are real only if the discriminant is positive:

$$k_3^2 + k_2^2 - k_1^2 \geq 0, \qquad (3.15)$$

where the equality

$$k_3^2 + k_2^2 - k_1^2 = 0, \tag{3.16}$$

corresponds to the tangency condition between the two ellipses. From (3.12):

$$\sin\theta_1 = \frac{k_1 + k_2\cos\theta_1}{k_3}, \tag{3.17}$$

hence, the correct quadrant of the angle θ_1 can be found using (3.14) and (3.17). Once the two intersections are found, the radial and perpendicular components of the velocity are computed for each orbit:

$$v_{r,ij} = \frac{\mu}{h}e\sin\theta_{ij}, \tag{3.18a}$$

$$v_{\perp,ij} = \frac{\mu}{h}(1 + e\cos\theta_{ij}). \tag{3.18b}$$

The first index i represents the orbit ($i = 1, 2$) and the second index j represents the intersection ($j = 1, 2$). Hence, we can write the velocity at each intersection as:

$$\mathbf{v_{ij}} = v_{r,ij}\hat{\mathbf{u}}_{r,ij} + v_{\perp ij}\hat{\mathbf{u}}_{\perp,ij}, \tag{3.19}$$

being $\hat{\mathbf{u}}_{r,ij}$ and $\hat{\mathbf{u}}_{\perp,\mathbf{ij}}$ the radial and perpendicular unit vectors. Therefore $\Delta\mathbf{v}_j$ ($j = 1, 2$) is given by:

$$\Delta\mathbf{v}_j = \mathbf{v}_{2j} - \mathbf{v}_{1j}. \tag{3.20}$$

The condition on the discriminant (Eq. (3.15)) translates into a condition for $\Delta\omega$ to be satisfied, i.e., the two ellipses intersect only in a limited range of values for $\Delta\omega$:

$$\tau \leq \Delta\omega \leq 2\pi - \tau, \tag{3.21}$$

with $\tau \in [0, 2\pi[$. The value of τ depends only on the shape of the two ellipses and can be explicitly calculated in terms of a_i and e_i ($i = 1, 2$) from the tangency condition, given by Eq. 3.16. For $\tau > 0$ the domain of intersections is limited by the geometrical configurations for which the ellipses are mutually tangent (Fig. 3.9), i.e., $\Delta\omega = \tau$ and $\Delta\omega = 2\pi - \tau$. On the other hand, if $\tau = 0$ no tangency condition exists and the two ellipses always have two intersections, regardless their relative orientation. In principle, one should vary $\Delta\omega$ for each pair of ellipses and then choose the value that minimizes the $\Delta V = \|\Delta\mathbf{v}\|$ at one of the two intersections. Actually, as our intuition suggests, the minimum-ΔV values corresponds to the tangency configuration. In order to prove it, we analysed the behaviour of ΔV as a function of $\Delta\omega$ for several pairs of ellipses, varying the semimajor axis and the eccentricity. For each pair, the value of τ has been determined and, by
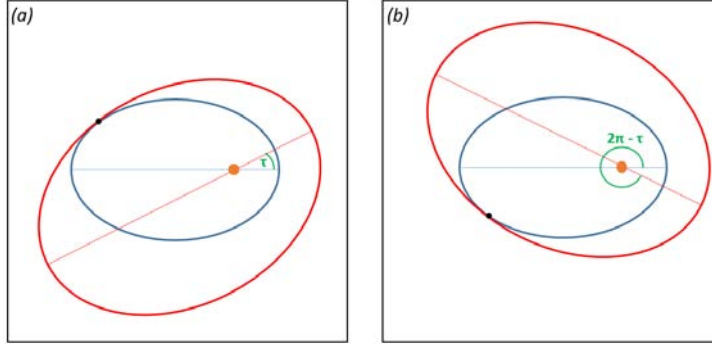
Figure 3.9: Relative angular displacement $\Delta\omega$ between the arguments of periapsis of two ellipses when they are mutually tangent. The configuration is symmetrical and the two ellipses are tangent for $\Delta\omega = \tau$ (left) or $\Delta\omega = 2\pi - \tau$ (right).

varying $\Delta\omega$ between τ and $2\pi - \tau$ with a certain discretization the value of ΔV has been computed at every intersection. The results show that if $\tau > 0$, ΔV has two equal minima when $\Delta\omega$ lies at either limit of the domain, i.e., when the two ellipses are mutually tangent. For all the other values of $\Delta\omega$, the cost is higher. In particular, ΔV is maximum when $\Delta\omega = \pi$, that is when the two apse lines are opposite (see Fig. 3.10). This behaviour always appears at least when the eccentricities are smaller than 0.2. In our case, since the ellipses studied are an extension of the motion originating in the vicinity of the libration points, their path in the IRF must inherit the behaviour of the corresponding equilibrium points, which move in circular orbits around the planet. Therefore, these orbits are expected to have low eccentricities and this guarantees the applicability of the intersection pattern shown in Fig. 3.10.

The procedure here presented is therefore completely analytical and allows to connect two states on the CIs without the need to propagate them numerically.

3.4 Application: from Europa to Ganymede and viceversa

In this section we present an application of the method to the case of a transfer between two consecutive Galilean moons, Europa and Ganymede. The orbits of the four Galilean moons are represented to scale in Fig. 3.11. Their relevant orbital parameters are listed in Table 3.1. Connections are
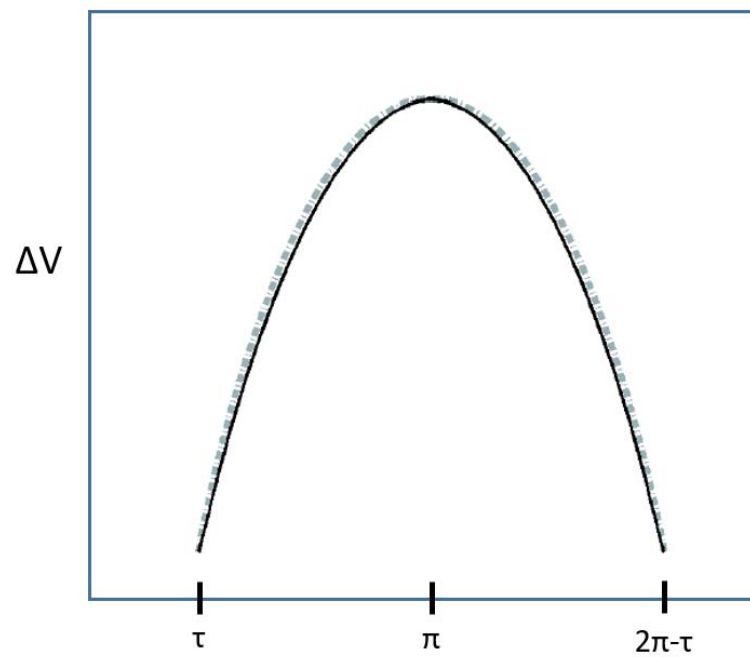
Figure 3.10: ΔV at the intersections between two ellipses versus their relative orientation $\Delta \omega$. The two different curves (solid and dashed) stand for the ΔVs at the two different intersections A and B. The minima correspond to the tangency configuration while the maximum is for $\Delta \omega = \pi$.
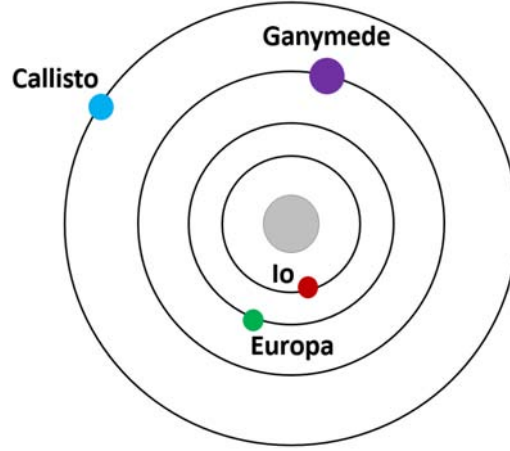
Figure 3.11: The orbits of the Galilean moons (the equatorial radii of Jupiter and the moons are not to scale).

sought by means of IMs and TOs in the intra-moon space. In the case of IMs, the transfer connects two PLOs, one around L_2 of Jupiter-Europa and the other around L_1 of Jupiter-Ganymede. On the other hand, when dealing with TOs, the trajectory links one point inside a PLO around L_2 of Jupiter-Europa and one inside a PLO around L_1 of Jupiter-Ganymede. PLOs are taken from two databases of 95 orbits (see Fig. 3.12), each discretized in 99 points. The Jacobi constant for PLOs around P_2 ranges from 3.001631769881 to 3.003593748544, while for PLOs around Ganymede P_1 the range is from 3.005357382121 to 3.007543590510 (sorted from 1 to 95 in increasing energy order, i.e., deceasing Jacobi constant). The CIs have radii of $38\,905\,\mathrm{km}$ for Europa and $97\,409\,\mathrm{km}$ for Ganymede, both corresponding to $k = 4$ in Eq. (3.1). The best coupling between the two CR3BPs is that which minimizes ΔV at the intersection point between the two ellipses at their tangent configuration in the inter-moon space. A common time event scheme is set up for IMs and TOs and is reported in Table 3.2.

3.4.1 Invariant manifolds

When designing a connection from Europa to Ganymede by means of IMs, the unstable IM of a Jupiter-Europa PLO is propagated to the CI around Europa and the stable IM around Jupiter-Ganymede is propagated to the CI around Ganymede. The stability must be reversed when dealing with the transfer from Ganymede to Europa. Using two databases of 95 PLOs, with each PLO discretized in 99 points (using a constant time-step), leads to more than 88 million possible intersections. However, only pairs in which the

Moon	Orbital radius $[10^5 \text{ km}]$	Orbital Period [days]	Mass ratio $[10^{-4}]$
Io	4.2180	1.8	0.470542991630
Europa	6.7110	3.6	0.252865845179
Ganymede	10.7040	7.2	0.780632933465
Callisto	18.8270	16.7	0.566808592975

Table 3.1: The second and the the third column represent the orbital radii and periods of the Galilean moons, respectively. The fourth column lists the mass ratios $m_i/(m_i + M)$, being m_i the mass of the moon and $M = 0.189\,813 \times 10^{28}$ kg the mass of Jupiter.
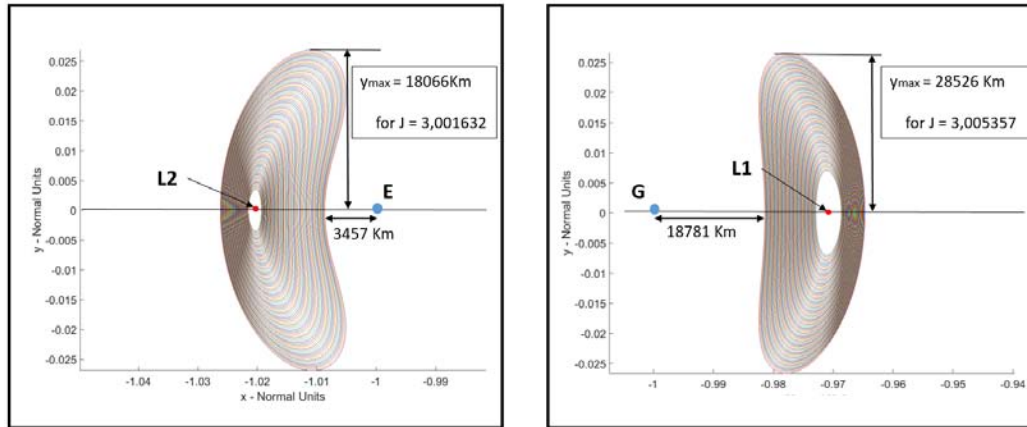

Figure 3.12: The database of PLOs around L_2 in the Jupiter-Europa CR3BP (left) and around L_1 in the Jupiter-Ganymede CR3BP (right) shown in their respective SRF. The maximum amplitude in the y direction of the largest PLO and its minimum distance to the moon are displayed.

Time event	Description
T_0	Initial condition on Europa's PLO
T_1	Leaving Europa's CI
T_2	ΔV
T_3	Entering Ganymede's CI
T_4	Initial condition on Ganymede's PLO

Table 3.2: Description of the main time events. Events T_0, T_1, T_3, T_4 occur in the intra-moons space, while T_2 represent the impulsive ΔV to be applied in the inter-moon space. Events T_0 and T_4 are associated with points on the PLO in the case of IMs, and with points inside the PLO for TOs.

periapsis of the outer ellipse is smaller than the apoapsis of the inner ellipse are selected. In the case of the connection from Europa to Ganymede, the total number of intersections to be analysed according with this criterion is drastically reduced to about 9 millions, corresponding to 10% of the total amount. Figures 3.13 and 3.14 show the eccentricities, the semimajor axes and the periapsis/apoapsis for the transfer from Europa to Ganymede and viceversa. As predicted, the eccentricities of the resulting ellipses are very small (smaller than 0.14 for this application) thus enabling the application of the algorithm described in Sect. 3.3. Moreover, each pair of ellipses have a strictly positive value of τ, meaning that a tangency configuration always exists and represents the minimum-ΔV solution for each possible transfer. A plot representing the minimum-ΔV of each pair of ellipses is showed in Fig. 3.15 for the transfer from Europa to Ganymede and viceversa. The absolute minimum is $\Delta V_{\text{MIN}} = 0.8814 \, \text{km s}^{-1}$ for both the outward and inward transfer. It is obtained for the PLO number 95 in both the databases, corresponding to the highest energies of the database. The minimum-cost trajectories are shown in Fig. 3.16. The times of flight using the time events described in Table 3.2 are reported in Table 3.4. As we can see from the last row, also the time of flight is the same for both transfer directions: as one may predict, the problem is symmetric. Hence, even the orbital elements of the two minimum-ΔV transfer ellipses are the same: they are reported in Table 3.5.
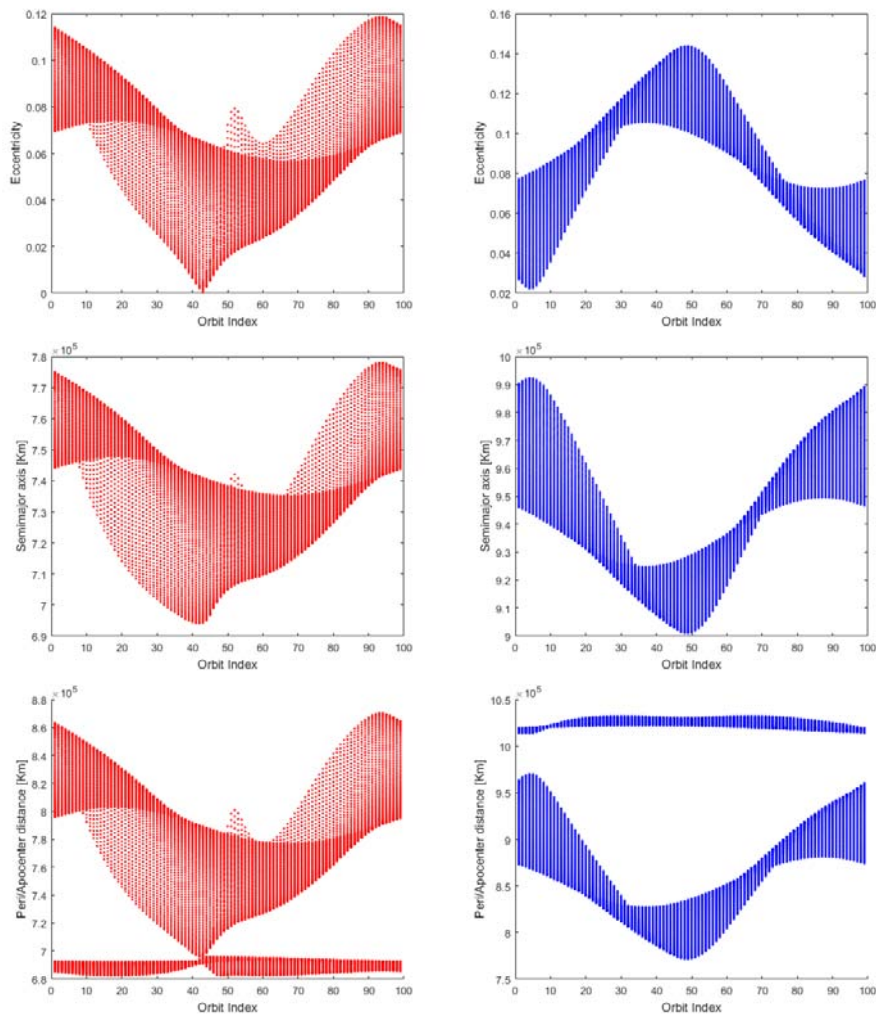
Figure 3.13: Eccentricities, semimajor axes and apo/periapsis for trajectories leaving the unstable IM around Jupiter-Europa L_2 (left column) and approaching the stable IM around Jupiter-Ganymede L_1 (right column). Each value in the plot is a function of the discretization index on each PLO (ranging from 1 to 99).
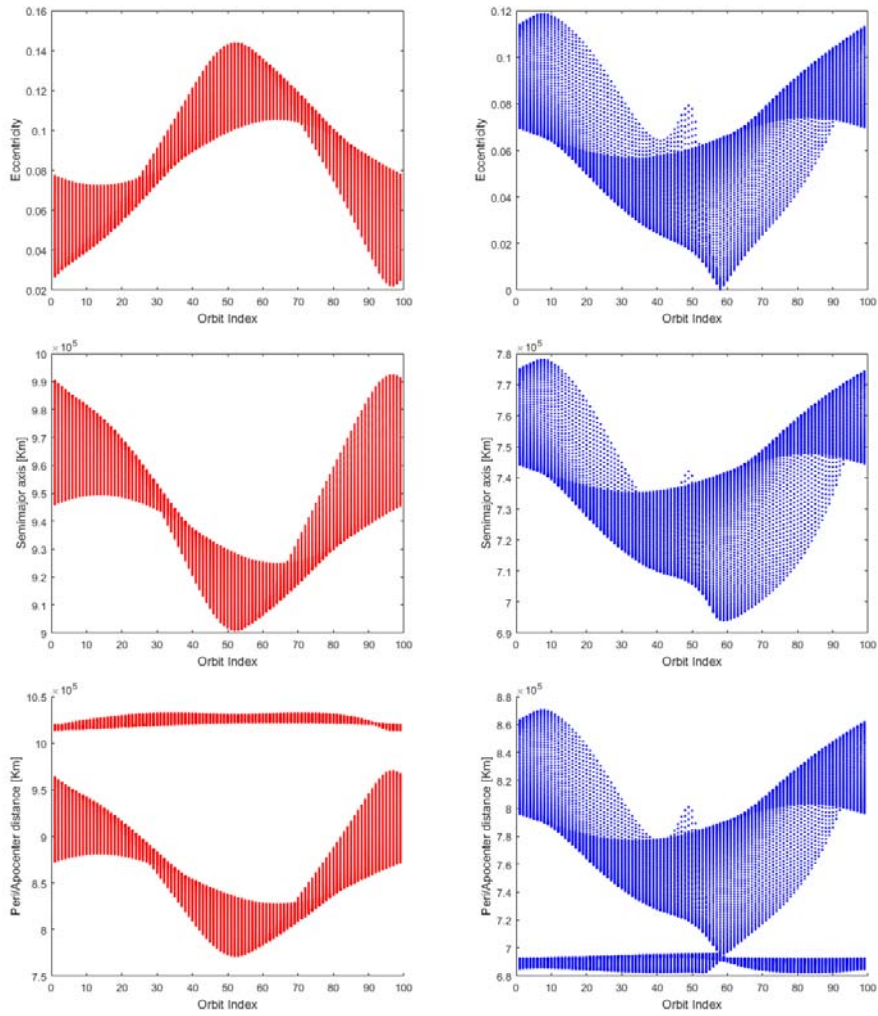
Figure 3.14: Eccentricities, semimajor axes and apo/periapsis for trajectories leaving the unstable IM around Jupiter-Ganymede L_1 (left column) and approaching the stable IM around Jupiter-Europa L_2 (right column). Each value in the plot is a function of the discretization index on each PLO (ranging from 1 to 99).
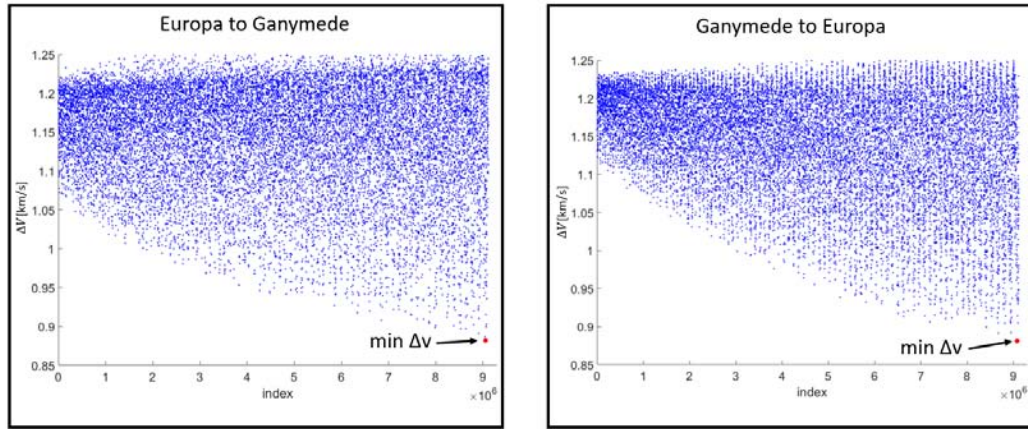
Figure 3.15: The cost of the cheapest transfers (corresponding to tangent ellipses) from Europa to Ganymede (left) and Ganymede to Europa (right) as functions of the combination index (ranging from 1 to ≈ 9 millions) with the IMs method inside the CI. The absolute minima are displayed within a red circle. For the sake of clarity, one coupling every 500 is showed in this map to prevent an excessive superposition of points.
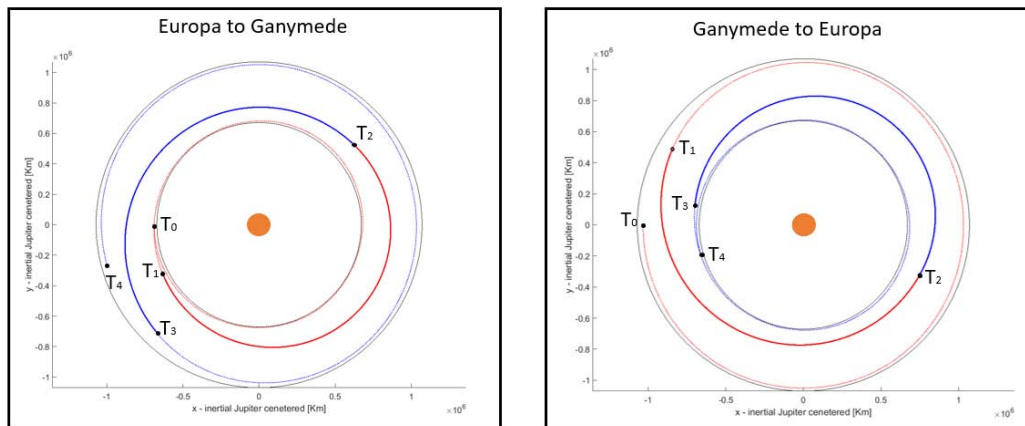
Figure 3.16: The transfer from Europa to Ganymede (left) and viceversa (right) as viewed from the Jupiter-centred IRF with the IMs method inside the CI. The time events $T_i (i = 1, \ldots, 5)$ refers to the time scheme reported in Table 3.2. The trajectory in the neighbourhood of Europa is plotted in red until time event T_2 (where the ΔV is applied). Moreover, the trajectory is represented with a dashed line as long as the spacecraft is inside the CI while it is a continuous line on the Keplerian ellipses.

3.4.2 Transit orbits

In the case of using TOs to construct the transfer, the initial conditions required for propagation in the intra-moon space are selected inside the PLOs of the database. This is done by means of a grid of points, as described in Sect. 3.3. Grids are computed with the following criteria:

1. the border of the grid is tangent to the PLO;

2. the distance between two consecutive points on the grid is constant in both the directions x and y.

As a consequence of the second criterion above mentioned, n_Y will vary according to the y-amplitude of the PLO. Each grid is then completely parametrized by n_X and n_β. For this application, we choose a grid discretization with $n_X = 5$. To select these angles β, discrete values in the range $R^- = [\pi/2, 3\pi/2]$ are chosen if the TOs are moving towards L_2 forward in time; on the other hand if the TOs are moving towards L_1 forward in time, values in the range $R^+ = [3\pi/2, \pi/2]$ are selected. Since a TO crosses the equilibrium regions flowing inside the spatial bi-dimensional projection of the same-energy manifold tube, the right angular range can be inferred looking at the motion provided by the latter. Analysing the manifold tubes for a transfer from Europa to Ganymede, we deduce that the range R^- must be chosen (see Fig. 3.17). For this application we select $n_\beta = 3$ with the velocity angles $\beta_1 = 3\pi/4$, $\beta_2 = \pi$ and $\beta_3 = 5\pi/4$. Similarly, the reverse transfer from Ganymede to Europa requires the range R^+ and we select $\beta_4 = 3\pi/4$, $\beta_5 = \pi$ and $\beta_6 = 5\pi/4$. Exploiting the entire range of 95 PLOs for each database with the designated values of n_X and n_β, the maximum number of possible couplings raises to more than 290 millions (see Table 3.3), considerably more than the previous case with IMs. Moreover, if one wants to double both the planar and the angular resolution, this number increases by a factor 64. Even if the actual number of intersections is reduced after applying the criterion of the apoapsis/periapsis, the overall computing time may still be high. However, from the previous results for IMs, we observed that the minimum-ΔV trajectory is generated for the highest energies (i.e., for the last orbits in the database); hence our intuition suggests to limit the range of the databases to the higher energies: for this application only PLOs from 70 to 95 are taken into account (Table 3.3). This will reduce the overall possible couplings to about 17 millions, which is the same order of magnitude as the corresponding value in the case of IMs (9 millions). The minimum-ΔV in this case is $\Delta V_{\mathrm{MIN}} = 0.5145\,\mathrm{km\,s}^{-1}$ in both directions and, again, it is associated with the highest energies of the two databases. A plot with the transfers in the
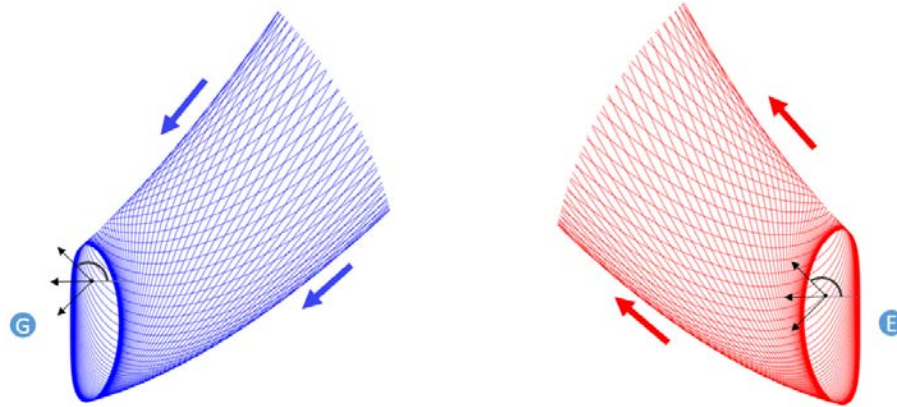
(a) Velocity directions for a grid point inside a PLO around Ganymede

(b) Velocity directions for a grid point inside a PLO around Europa

Figure 3.17: Selected velocity directions for the transfer from Europa to Ganymede using TOs, i.e., $\beta_1 = 3\pi/4$, $\beta_2 = \pi$, $\beta_3 = 5\pi/4$ (represented by three black arrows). These values are the same for all the grid points inside the PLOs around Europa (a) and Ganymede (b).
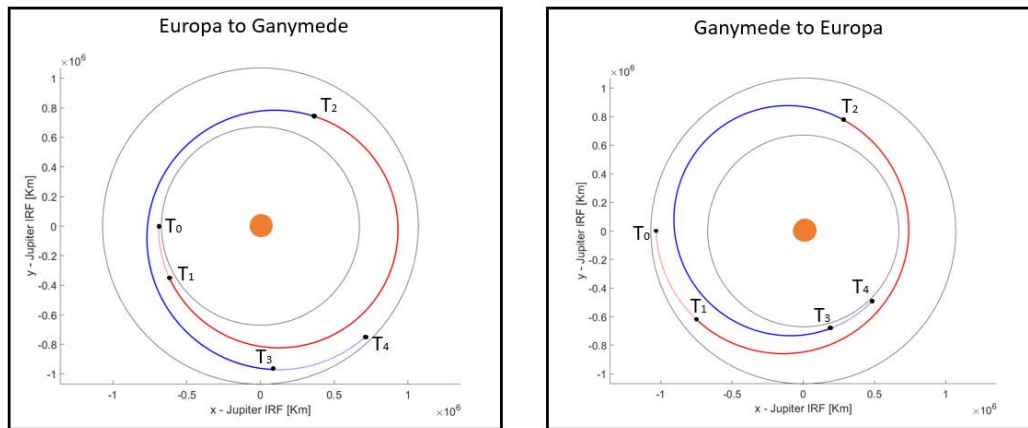
Figure 3.18: Transfer from Europa to Ganymede (left) and viceversa (right) as viewed from the Jupiter-centred IRF with the TOs method inside the CI. The time events $T_i (i = 1, \ldots, 5)$ refer to the time scheme reported in Table 3.2. The trajectory in the neighbourhood of Europa is plotted in red until time event T_2 (where the ΔV is applied). Moreover, the trajectory is represented with a dashed line as long as the spacecraft is inside the CI and with the continuous on the Keplerian ellipses.

		Europa database	Ganymede database
1 ÷ 95	Total initial conditions	16425	17625
	Min linear resolution	2802 km	3741 km
	Max linear resolution	297 km	914 km
	Average linear resolution	1337 km	2312 km
70 ÷ 95	Total initial conditions	3834	4521
	Min linear resolution	2802 km	3743 km
	Max linear resolution	1890 km	2942 km
	Average linear resolution	2355 km	3336 km

Table 3.3: Significant parameters for the database of PLOs around Europa and Ganymede using $n_X = 5$ and $n_\beta = 3$. The table shows the difference between two sets of PLOs taken into account: from PLO 1 to 95 and from PLO 70 to 95. In the first case about 290 millions possible intersections can be found, in the second case only 17 millions. Since n_X is fixed, the linear resolution will vary depending on the dimensions of the current PLO. As a consequence, the smaller PLO of the database is associated to the maximum resolution value.

	Time event	Europa to Ganymede [days]	Ganymede to Europa [days]
	T_0	0	0
	T_1	3.82	6.54
IMs	T_2	4.68	7.67
	T_3	5.85	8.58
	T_4	12.38	12.38
	T_0	0	0
	T_1	0.29	0.77
TOs	T_2	1.07	1.71
	T_3	2.00	2.49
	T_4	2.78	2.78

Table 3.4: Time events for the coupling between Europa and Ganymede (and viceversa) when IMs and TOs are employed for propagation in the intra-moon space.

Jupiter-centred IRF is reported in Fig. 3.18. The main time events are reported in Table 3.4. Eccentricities, semimajor axes and the values of $\Delta\omega$ in this case are reported in Table 3.5.

3.5   Results

We have verified the physical validity of the solutions in the case of IMs by propagating the initial state on the PLO around L_2 of Europa forward in time to the manoeuvre point in the Jupiter-Europa CR3BP, and the final state on the PLO around L_1 of Ganymede backwards in time to the manoeuvre point in the Jupiter-Ganymede CR3BP. The propagation time is of 4.68 days over the former segment and 7.70 days over the latter. The distance between the endpoints of the two segments is of 7000 km, which is equivalent to the accumulation of a speed error of $6\,\mathrm{m\,s^{-1}}$ over the whole transfer (7000 km / 14.48 days). This error, due to the Keplerian approximation of the CR3BP model, is negligible when compared with the size of the computed manoeuvre $(0.88\,\mathrm{km\,s^{-1}})$.

| | | Keplerian ellipses | |
		From/to Europa CI	From/to Ganymede CI
IMs	Eccentricity	0.11854803	0.14374662
	Semi-major axis	7.780×10^5 km	9.001×10^5 km
	$\Delta\omega$	295.19°	
TOs	Eccentricity	0.15159419	0.16323860
	Semi-major axis	8.114×10^5 km	8.843×10^5 km
	$\Delta\omega$	329.67°	

Table 3.5: Eccentricities, semimajor axes and $\Delta\omega$ of the osculating ellipses connecting Europa to Ganymede and viceversa.

The numerical code has been written with Matlab R2015b on a Lenovo Laptop computer with Intel Core i7-4510U, 2.6 GHz CPU and Windows 10. Numerical integrators are written in `C++` and then integrated in Matlab as binary MEX files to reduce the computing time. Matlab Parallel Computing Toolbox is used to increase performances. The computations are performed in two phases. In the first phase, after discretizing the PLOs, IMs and TOs are integrated until the two CIs: the integration of IMs requires 11 s, while 20 s are required for TOs (in this case, most of the time is spent to compute the grids and to write the output file). In the second phase, the minimum-cost intersections of all the possible pairs of ellipses are determined and the cheapest trajectory is identified; this phase requires about 70 s (88 millions possible couplings) for IMs and 40 s for TOs (17 millions possible couplings). By comparing data from Table 3.4, the transfer performed by means of TOs is clearly faster than the corresponding coupling with IMs (2.78 days versus 12.38 days) as well as cheaper in terms of ΔV (514.5 m s^{-1} versus 881.4 m s^{-1}). In particular, TOs do not wind around the PLO (Figs. 3.19c and 3.19d). Therefore, they provide a faster path from the initial condition to the CI (and viceversa) when compared with IMs (Figs. 3.19a and 3.19b). The short time-of-flight provided by TOs makes them more feasible for a real mission. In fact, the intense particle radiation belts of the Jovian magnetosphere, which extend almost to the orbit of Ganymede, may represent a serious obstacle to the practical implementation of trajectories that spend many days in the inter-moon space.

(a) Europa inter-moon, IMs

(b) Ganymede inter-moon, IMs

(c) Europa inter-moon, TOs
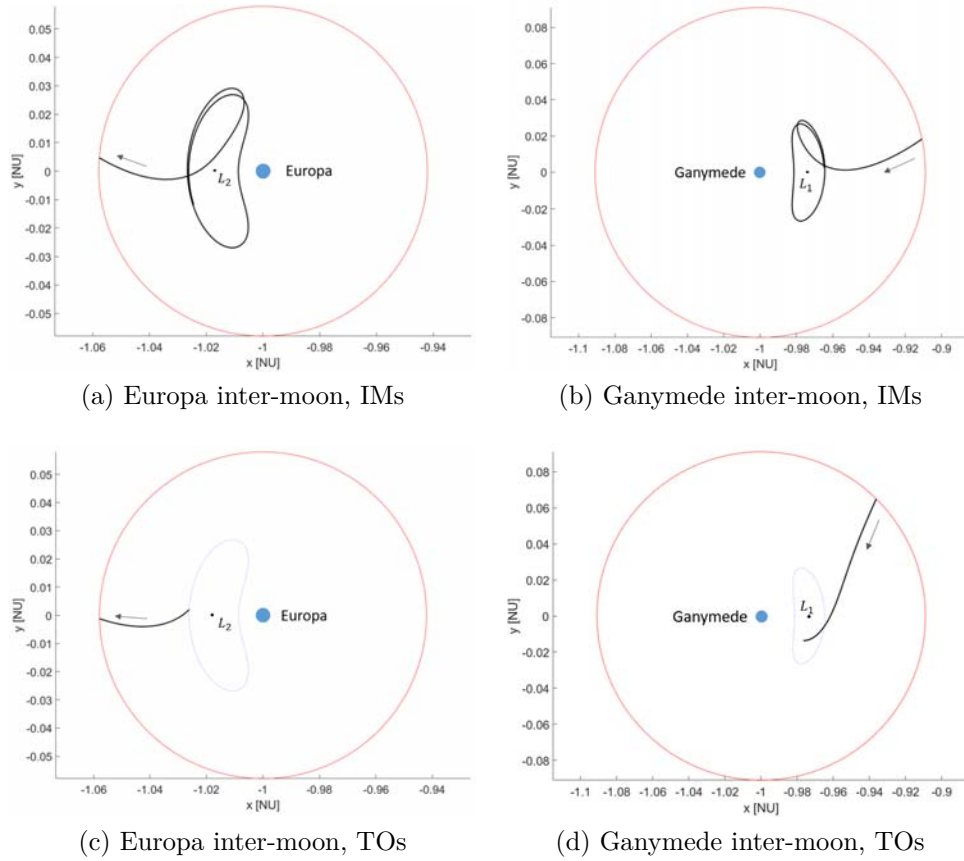
(d) Ganymede inter-moon, TOs

Figure 3.19: Europa-to-Ganymede minimum-ΔV transfers in the intra-moon space of Europa (a) and Ganymede (b) using IMs; Figs. (c) and (d) are the analogous trajectories computed with TOs. The CI is represented in red in each case. For the sake of clarity, the two PLOs corresponding to the minimum-ΔV solution are represented in Figs. (c) and (d).

Chapter 4

Tour of the Galilean moons

Introduction. In this chapter we aim at finding a trajectory visiting the Galilean moons Europa, Ganymede and Callisto (i.e., a *tour* of the Galilean moons) by repeatedly applying the coupled CR3BP between consecutive moons. Starting from an initial state in the neighbourhood of the inner moon, i.e., Europa, our goal is to find a trajectory towards the outer moon, i.e., Callisto, passing by Ganymede (*outward journey*); then, the trajectory comes back to the initial state (in the SRF) in the vicinity of Europa passing again by Ganymede (*inward journey*). The method to link multiple CR3BPs (Sect. 4.1) and to find the optimal connection (Sect. 4.2) is explained. A key issue in the design of the tour is identifying the right match of the initial phase angles of the several moons: as a matter of fact, the connection between two consecutive moons requires that a certain relative phase exists at the beginning of the transfer. When linking more inter-moon connections, the issue of the relative phase is even more critical because it implies times given by the synodical period of more than two moons, which is a large value. Therefore, once the initial phase angles for the outward journey are fixed, suitable parking orbits (*rephasing orbits*) around Ganymede and Callisto are designed to accomplish the inward journey (Sect. 4.3). The complete tour is illustrated and discussed in Sect. 4.4.

4.1 Preliminary considerations

To find connections between multiple Galilean moons, four coupled CR3BPs are taken into account, i.e., from Europa to Ganymede, from Ganymede to Callisto, from Callisto to Ganymede and from Ganymede to Europa. The whole trajectory is constructed by joining different intra-moon and inter-moon branches. Clearly, each intra-moon leg is conceived in the proper
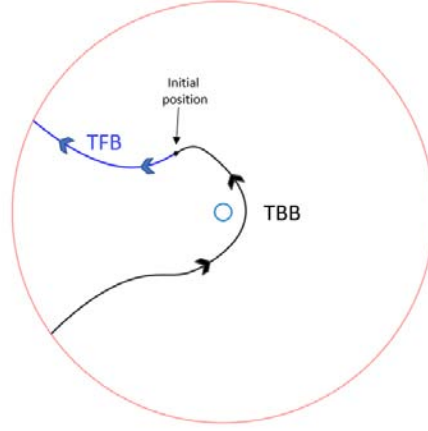
Figure 4.1: Example of TFB and TBB propagated from an initial condition in the neighbourhood of Jupiter-Europa L_2. The arrows point towards the positive time direction.

coupled CR3BP model. Inside the intra-moon space, TOs are used instead of IMs trajectories, because of the noticeable time-of-flight reduction provided by the former (see Sect. 3.5).

According to the method described in Sect. 3.2, let $\mathbf{x}_0^1, \mathbf{x}_0^2, \mathbf{x}_0^3, \mathbf{x}_0^4$ be four initial states around Jupiter-Europa L_2, Jupiter-Ganymede L_1, Jupiter-Callisto L_1 and Jupiter-Ganymede L_2, respectively, expressed in their SRFs. From each $\mathbf{x}_0^i$, two branches of a TO, rather than one, are now considered: the time-forward branch (TFB) and the time-backward branch (TBB), as shown in Fig. 4.1. The former is obtained by propagating $\mathbf{x}_0^i$ in the positive time direction, the latter in the negative time direction.

The tour of the Galilean moons is made up of:

1. a TFB originating from $\mathbf{x}_0^1$ until the CI of Europa,

2. two inter-moon branches connecting the CI of Europa and the CI of Ganymede,

3. a TBB connecting the CI of Ganymede to $\mathbf{x}_0^2$,

4. a TFB connecting $\mathbf{x}_0^2$ and the CI of Ganymede,

5. two inter-moon branches connecting the CI of Ganymede and the CI of Callisto,

6. a TBB connecting the CI of Callisto and $\mathbf{x}_0^3$,

7. a rephasing orbit connecting $\mathbf{x}_0^3$ to itself,

8. a TFB connecting $\mathbf{x}_0^3$ and the CI of Callisto,

9. two inter-moon branches connecting the CI of Callisto and the CI of Ganymede,

10. a TBB connecting the CI of Ganymede and $\mathbf{x}_0^4$,

11. a rephasing orbit connecting $\mathbf{x}_0^4$ to itself,

12. a TFB connecting $\mathbf{x}_0^4$ and the CI of Ganymede,

13. two inter-moon branches connecting the CI of Ganymede and the CI of Callisto,

14. a TBB connecting the CI of Europa to $\mathbf{x}_0^1$.

Steps $1, 3, 4, 6, 7, 8, 10, 11, 12$ occur in the intra-moon space of the respective moons, the remaining ones occur in the inter-moon space. The outward journey connects $\mathbf{x}_0^1$ to $\mathbf{x}_0^3$ (from step 1 to 6); the inward journey connects $\mathbf{x}_0^3$ to $\mathbf{x}_0^1$ (from step 7 to 14). The tour is closed because the final step ends up at the same state $\mathbf{x}_0^1$ of the first step. A change in velocity with magnitude ΔV_{ij} is required during steps $2, 5, 9, 11$ in order to connect $\mathbf{x}_0^i$ and $\mathbf{x}_0^j$. We define ΔV_{TOT} as the sum of the four ΔV_{ij}:

$$\Delta V_{\mathrm{TOT}} = \Delta V_{12} + \Delta V_{23} + \Delta V_{34} + \Delta V_{41}. \tag{4.1}$$

Similarly, the total time of flight $\mathrm{TOF}_{\mathrm{TOT}}$ is defined as:

$$\mathrm{TOF}_{\mathrm{TOT}} = \mathrm{TOF}_{12} + \mathrm{TOF}_{23} + \mathrm{TOF}_{34} + \mathrm{TOF}_{41}, \tag{4.2}$$

being TOF_{ij} the time required to connect $\mathbf{x}_0^i$ to $\mathbf{x}_0^j$. Additionally, we call $\Delta V_{\mathrm{reph}}^C$ and $\Delta V_{\mathrm{reph}}^G$ the ΔVs required for the rephasing around Ganymede and Callisto respectively; T_{reph}^C and T_{reph}^G are the times of flight of the corresponding rephasing orbits.

The morphologies requested for the TOs inside the intra-moon space of each moon verify the following set of constraints:

- Inside the intra-moon space around Europa, the TO approaches the moon and leaves it through the L_2 gateway (see Fig. 4.2a).

- Inside the intra-moon space around Ganymede, during the outward journey, the TO approaches the moon through the L_1 gateway, it makes a complete turn around the moon and leaves it through the L_2 gateway (see Fig. 4.2b).

- Inside the intra-moon space around Callisto, the TO approaches and leaves the moon through the L_1 gateway (see Fig. 4.2c).

- Inside the intra-moon space around Ganymede, during the inward journey, the TO approaches the moon through the L_2 gateway, it makes a complete turn around the moon and leaves it through the L_1 gateway (see Fig. 4.2d).

- The TO does not impact the moon inside any intra-moon space.

- The minimum altitude with respect to the moon's surface must be grater than a given limit for safety reasons. We set this limit to $50\,\mathrm{km}$ (the same value is employed in [Colasurdo et al., 2014]).

We call $\mathcal{C}$ the above set of constraints. Accordingly, the states $\mathbf{x}_0^1, \mathbf{x}_0^2, \mathbf{x}_0^3, \mathbf{x}_0^4$ are said $\mathcal{C}$-*connected* if the corresponding TOs satisfy the condition imposed by $\mathcal{C}$ and:

- a connection between $\mathbf{x}_0^1$ and $\mathbf{x}_0^2$ exists in the coupled CR3BP between Europa and Ganymede,

- a connection between $\mathbf{x}_0^2$ and $\mathbf{x}_0^3$ exists in the coupled CR3BP between Ganymede and Callisto,

- a connection between $\mathbf{x}_0^3$ and $\mathbf{x}_0^4$ exists in the coupled CR3BP between Callisto and Ganymede,

- a connection between $\mathbf{x}_0^4$ and $\mathbf{x}_0^1$ exists in the coupled CR3BP between Ganymede and Europa.

A sketch of four $\mathcal{C}$-connected states is represented in Fig.4.3.

4.2 The optimal connection

In this section, the algorithm used to find the optimal $\mathcal{C}$-connected states is explained. It is divided into two main steps.

1. A first set of grids with $n_X = 10$ and $n_\beta = 30$ is generated around the four relevant Jupiter-moon Lagrangian points. Using the criteria described in Sect. 3.2, velocity angles β are selected in the range $\Delta\beta_1 = [3\pi/4, 5\pi/4]$ for grids around Jupiter-Europa L_2, Jupiter-Ganymede L_1 and Jupiter-Callisto L_1; the range $\Delta\beta_2 = [-\pi/4, \pi/4]$ is used for grids around Jupiter-Ganymede L_2. Only the last 35 PLOs of each PLO-database are taken into account to generate grids: this choice is justified

(a) *TO morphology around Europa.*

(b) *TO morphology around Ganymede (outward journey).*

(c) *TO morphology around Callisto.*
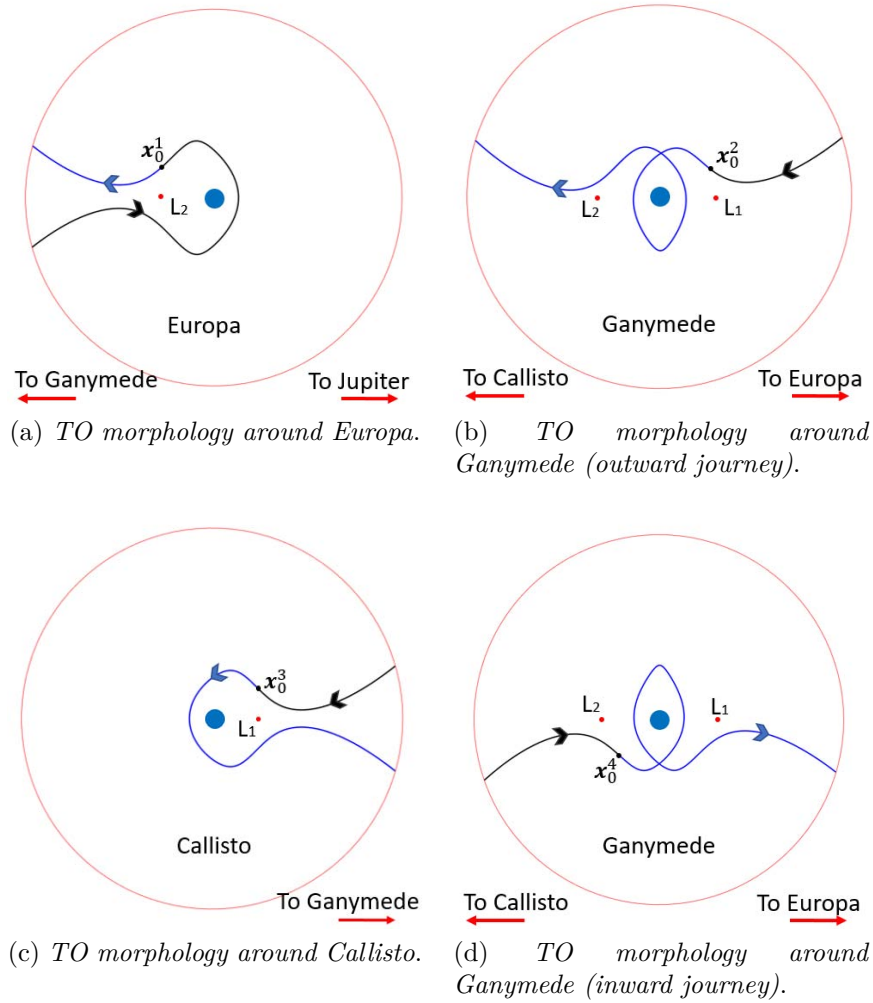
(d) *TO morphology around Ganymede (inward journey).*

Figure 4.2: TOs morphologies required to satisfy the constraints $\mathcal{C}$. TFBs and TBBs are represented in blue and black, respectively. The CI for each moon is represented in red. The Lagrangian points are marked with red dots. The sizes of the moons are not to scale.
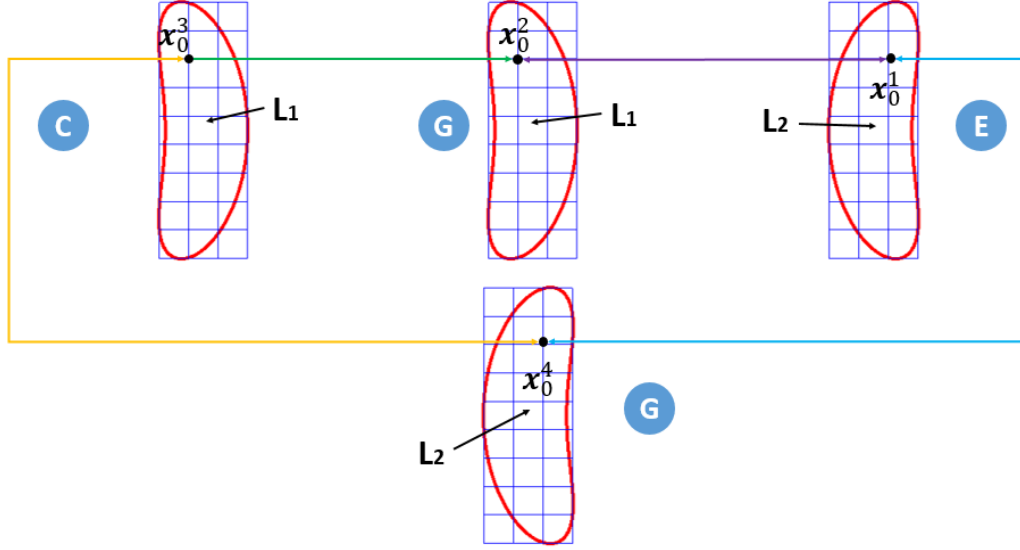
Figure 4.3: Four $\mathcal{C}$-connected states. Each coloured line represents a link between two initial conditions in a coupled CR3BP verifying the constraints $\mathcal{C}$.

by the fact that TOs providing couplings between consecutive moons with low ΔV are those with higher energies. The total amount of initial conditions provided by each database at the planar and angular resolution considered is reported in Table 4.1. From Table 4.1, the amount of theoretical connections verifying the constraints $\mathcal{C}$ is about 13×10^{15}; among them, 29 billions are $\mathcal{C}$-connected. This number can be further reduced to approximately 3×10^5 if only connections with $\Delta V_{ij} < 1.1\,\mathrm{km\,s^{-1}}$ $(ij = 12, 23, 34, 41)$ are taken into account. We call $\mathcal{T}_1$ the set of $\mathcal{C}$-connected states $\mathbf{x}_0^1, \mathbf{x}_0^2, \mathbf{x}_0^3, \mathbf{x}_0^4$ verifying the additional constraint on ΔV_{ij}: they are represented in Fig. 4.4a as a function of ΔV_{TOT} and $\mathrm{TOF}_{\mathrm{TOT}}$. ΔV_{TOT} ranges from $4.272\,\mathrm{km\,s^{-1}}$ to $4.463\,\mathrm{km\,s^{-1}}$; $\mathrm{TOF}_{\mathrm{TOT}}$ ranges from $46.63\,\mathrm{days}$ to $47.76\,\mathrm{days}$. The minimum-ΔV_{TOT} connection is characterized by the following parameters:

$$\Delta V_{\mathrm{TOT}} = 1.044 + 1.111 + 1.096 + 1.021 = 4.272\,\mathrm{km\,s^{-1}}, \qquad (4.3)$$
$$\mathrm{TOF}_{\mathrm{TOT}} = 3.982 + 14.888 + 17.616 + 10.629 = 47.116\,\mathrm{days}, \qquad (4.4)$$
$$\beta_{01}^1 = 225°, \qquad (4.5)$$
$$\beta_{02}^1 = 135°, \qquad (4.6)$$
$$\beta_{03}^1 = 135°, \qquad (4.7)$$
$$\beta_{04}^1 = -41.9°, \qquad (4.8)$$

		Europa	Ganymede-out	Callisto	Ganymede-in
$\mathcal{T}_1$	Total ICs	232080	269760	272580	257520
	ICs verifying $\mathcal{C}$	6088 (2.6%)	10924 (4%)	28429 (10.4%)	9450 (3.6%)
	Average planar res.	1085 km	1590 km	2404 km	1746 km
	Angular resolution	3°	3°	3°	3°
$\mathcal{T}_2$	Total ICs	5040	5040	2880	5040
	ICs verifying $\mathcal{C}$	1724 (34.2%)	1333 (26.4%)	1809 (62.8%)	1185 (23.5%)
	Average planar res.	122 km	197 km	277 km	193 km
	Angular resolution	0.3°	0.3°	0.3°	0.3°

Table 4.1: Total number of initial conditions (ICs), ICs verifying the set of constraints $\mathcal{C}$, average linear resolution and angular resolution for the sets $\mathcal{T}_1$ and $\mathcal{T}_2$. The data are organized in four columns, representing the grids around Jupiter-Europa L_2 (Europa), Jupiter-Ganymede L_1 (Ganymede-out), Jupiter-Callisto L_1 (Callisto) and Jupiter-Ganymede L_2 (Ganymede-in), respectively. The amount of ICs verifying the constraints $\mathcal{C}$ is a small percentage of the ICs available (especially for the set $\mathcal{T}_1$). The average linear resolution is clearly higher in the case of $\mathcal{T}_2$. The angular resolution associated to $\mathcal{T}_2$ is one order of magnitude larger than that of $\mathcal{T}_1$.

	Europa	Ganymede-out	Callisto	Ganymede-in
N_{PLO}	86	85	95	85
β [degree]	226.42	134.2105	133.8947	-42.3703
J	3.0018724817	3.0055926754	3.0047941710	3.0054564204
Min altitude [km]	2966.911	10690.407	16498.978	10628.1610

Table 4.2: Index of the PLO-database, velocity angle β, Jacobi constant and minimum altitude provided by initial conditions in the set $\mathcal{T}_2^{\min \Delta V}$.

being β_{0i}^1 the angle β associated with $\mathbf{x}_0^i$. We call $\mathcal{T}_1^{\min \Delta V}$ the four initial conditions in the set $\mathcal{T}_1$ providing the minimum-ΔV_{TOT} connection. Furthermore, N_{PLO}^i is the database index of the ith $(i = 1, \dots, 4)$ initial condition in the set $\mathcal{T}_1^{\min \Delta V}$.

2. A new set of sub-grids with $n_X = n_Y = 5$, and $n_\beta = 20$ is computed in the neighbourhood of the four $\mathbf{x}_0^i \in \mathcal{T}_1^{\min \Delta V}$, $(i = 1, \dots, 4)$. (see Fig. 4.5). Velocity angles β are selected in the range $\Delta \beta_3 = [\beta_{0i} - 3, \beta_{0i} + 3]$ deg, being β_{0i} $(i = 1, \dots 4)$ given by Eqs. (4.5), (4.6), (4.7) and (4.8). Only PLOs in the range $[N_{\mathrm{PLO}}^i - 3, N_{\mathrm{PLO}}^i + 3]$ are considered. From Table 4.1, the amount of theoretical couplings between states verifying the constraints $\mathcal{C}$ is about 5×10^{12}; among them, 3.2 billions are $\mathcal{C}$-connected. This number can be further reduced to roughly 10^5 if only connections with $\Delta V_{ij} < 1.1 \, \mathrm{km \, s^{-1}}$ are taken into account. We call $\mathcal{T}_2$ the set of initial conditions providing such connections: they are represented in Fig. 4.4b as functions of ΔV_{TOT} and $\mathrm{TOF}_{\mathrm{TOT}}$. The minimum-$\Delta V_{\mathrm{TOT}}$ connection is characterized by

$$\Delta V_{\mathrm{TOT}} = 1.028 + 1.099 + 1.096 + 1.005 = 4.227 \, \mathrm{km \, s^{-1}}, \qquad (4.9)$$
$$\mathrm{TOF}_{\mathrm{TOT}} = 3.941 + 14.871 + 17.586 + 10.660 = 47.058 \, \mathrm{days}. \quad (4.10)$$

We call $\mathcal{T}_2^{\min \Delta V}$ the set of four initial conditions providing the minimum-ΔV_{TOT} connection. Other relevant parameters for $\mathcal{T}_2^{\min \Delta V}$ are reported in Table 4.2.

The set of initial states provided by $\mathcal{T}_2^{\min \Delta V}$ is regarded as the optimal connection. The TOs in the intra-moon space of the four moons associated with this connection are represented in Fig. 4.6.
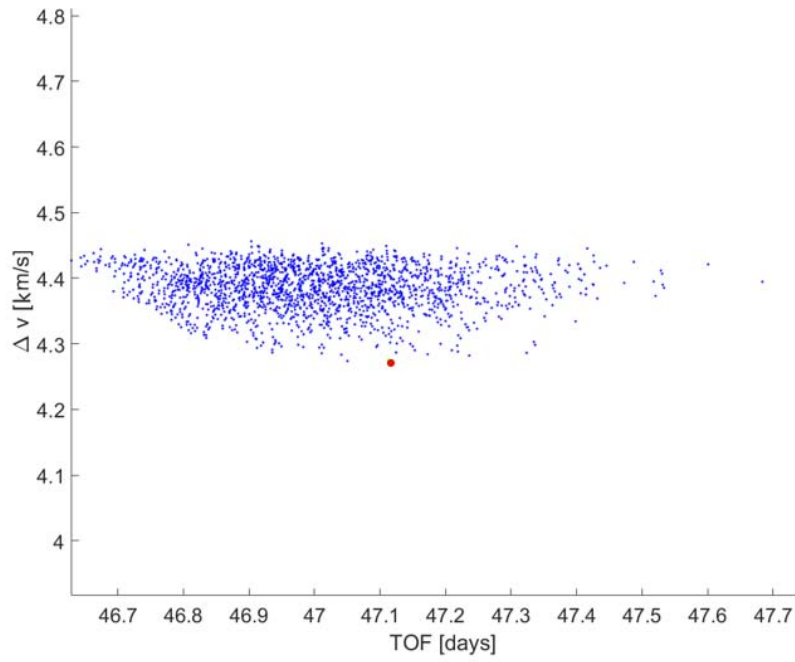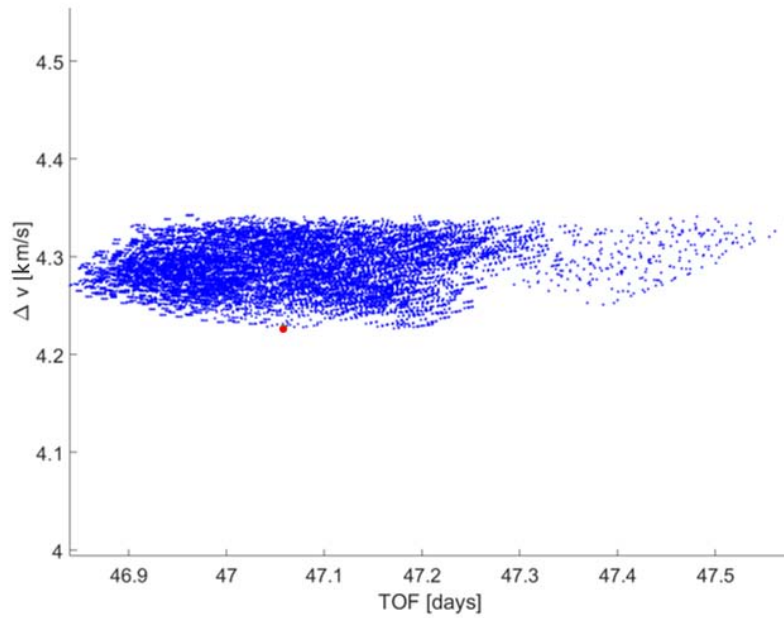
(a) $\mathcal{T}_1$ connections.

(b) $\mathcal{T}_2$ connections.

Figure 4.4: Connections in the set $\mathcal{T}_1$ and $\mathcal{T}_2$ as functions of ΔV_{TOT} and $\mathrm{TOF}_{\mathrm{TOT}}$. The connections with the minimum ΔV_{TOT} are marked with a red dot.
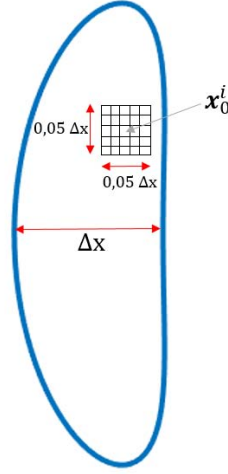
Figure 4.5: 5×5 sub-grid around the (x, y) components of an initial condition $\mathbf{x}_0^i$ associated to a given PLO. Δx is the x-amplitude of the PLO. The size of the sub-grid is $0.05\Delta x$.

4.3   Rephasing

The optimal connection $\mathcal{T}_2^{\min \Delta V}$ has been defined as the one that which minimizes the total sum of ΔVs accumulated in each stage of the tour. As discussed in Chapt. 3, the design of each inter-moon leg of trajectory includes the relative phase α_0 of the two moons under consideration at the initial time (see Appendix E). When the Europa-to-Ganymede and Ganymede-to-Callisto connections are linked together for the outward journey, it is straightforward to find a set of initial phases of the three moons at the time $t_0 = 0$ (when the spacecraft leaves $\mathbf{x}_0^1$) to guarantee the connection from $\mathbf{x}_0^1$ to $\mathbf{x}_0^3$. In the case of $\mathbf{x}_0^i \in \mathcal{T}_2^{\min \Delta V}$ $(i = 1, \ldots, 4)$ the initial phases $\alpha(t_0)$ for the three moons are:

$$\alpha_E(t_0) = 180°, \tag{4.11a}$$
$$\alpha_G(t_0) = 260.5°, \tag{4.11b}$$
$$\alpha_C(t_0) = 244.6°. \tag{4.11c}$$

Here the subscripts E, G, C refer to Europa, Ganymede and Callisto, respectively. However, the next coupling between $\mathbf{x}_0^3$ and $\mathbf{x}_0^4$, i.e., between Callisto and Ganymede at the beginning of the inward journey, requires a relative phase between Callisto and Ganymede that does not correspond with that at the end of the outward journey. The same problem occurs for the final connection between $\mathbf{x}_0^4$ and $\mathbf{x}_0^1$. To address this issue the idea is to "park" the spacecraft on some orbits (rephasing orbits) around Callisto and Ganymede
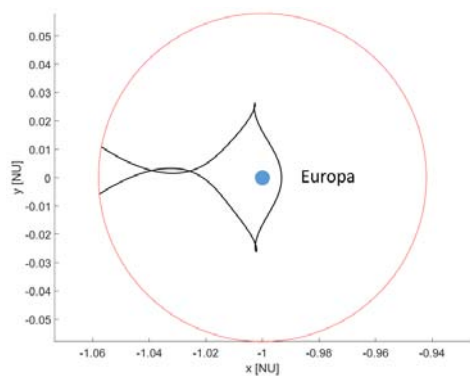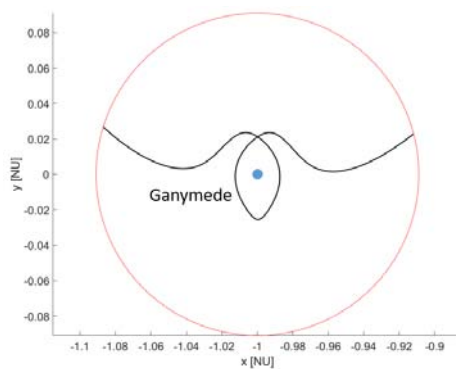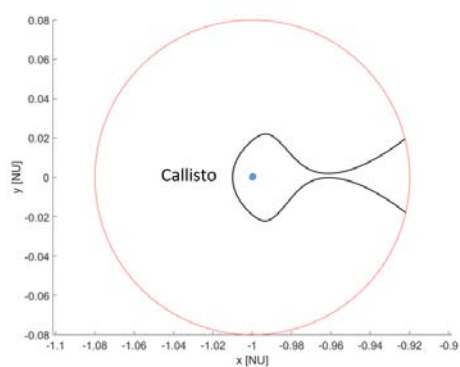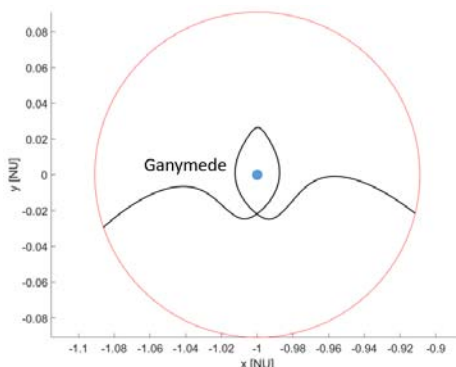
(a) *TO around Europa.*

(b) *TO around Ganymede (outward journey).*

(c) *TO around Callisto.*

(d) *TO around Ganymede (inward journey).*

Figure 4.6: TOs related to the selected connection $\mathcal{T}_2^{\min \Delta V}$ in their respective intra-moon region. The reference frames are the SRFs of the three moons. The CIs of the four moons are represented in red.

during the inward journey and wait for the right rephasing of the moon required by the optimal connection. The insertion into the rephasing orbits is carried out through impulsive manoeuvres, the magnitudes of which add propellant to the existing budget. Besides, the total time of flight over the tour increases. In this case, the two required rephasing time T_{REPH}^{C}, T_{REPH}^{G} around Ganymede and Callisto, respectively, are:

$$T_{\text{reph}}^{C}(n) = 4.243 + nT_{CG}^{\text{syn}}, \qquad (4.12\text{a})$$

$$T_{\text{reph}}^{G}(n) = 5.0576 + nT_{GE}^{\text{syn}}, \qquad (4.12\text{b})$$

with $n \in \mathbb{N}$. The first term of Eqs.(4.12) depends on the initial conditions $\mathbf{x}_0^i$ ($i = 1, \dots, 4$) given by $\mathcal{T}_2^{\min \Delta V}$, the second is the synodical period between Callisto and Ganymede (T_{CG}^{syn}) or Ganymede and Europa (T_{GE}^{syn}), i.e., the time needed to repeat the same relative phases between two moons. These periods are:

$$T_{CG}^{\text{syn}} = \frac{2\pi}{\omega_G - \omega_C} = 12.524\,\text{days}, \qquad (4.13\text{a})$$

$$T_{GE}^{\text{syn}} = \frac{2\pi}{\omega_E - \omega_G} = 7.055\,\text{days}, \qquad (4.13\text{b})$$

being ω_E, ω_G, ω_C the orbital angular velocities of Europa, Ganymede and Callisto, respectively. Hence, the rephasing time is made up by a constant term and a multiple of the synodical period.

If the initial and final point of the rephasing orbit are the same and coincide with a point of the TOs around the moon, then the rephasing time given by Eqs. (4.12) does not change when such point is varied along the TO itself (for a proof see Appendix F). For example, given the TO around Callisto, the rephasing orbit can start at any point before and after $\mathbf{x}_0^3$.

We take advantage of this fact to find possible rephasing orbits around Callisto and Ganymede (during the inward journey) minimizing the total ΔV_{REPH} required. The idea is to find possible rephasing orbits starting from points below a given altitude from each moon, by applying three ΔVs: the first is used to reduce velocity magnitude of the spacecraft for insertion into a non-diverging trajectory around the moon (i.e., a trajectory able to execute several revolutions around the moon without escaping the P_2 region), the second one aiming at changing the velocity vector to correct the time of flight of the rephasing orbit, which must coincide with that given by Eqs. (4.12) at the end of the rephasing manoeuvre, and the final is used to increase again the magnitude of the spacecraft's velocity for insertion in the original TO.

The algorithm is the same for the two moons and it is divided in the following steps.
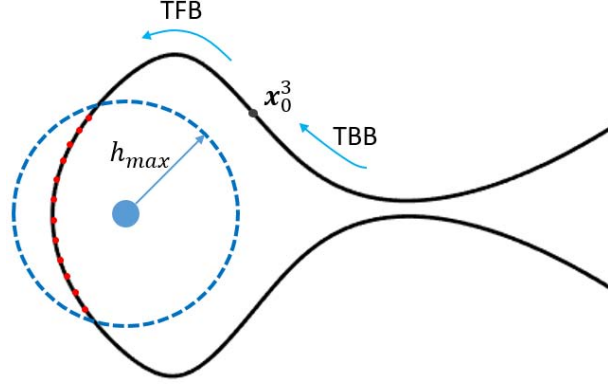
Figure 4.7: Initial points (represented as red dots) for rephasing orbits are chosen below a given altitude h_max from the moon along the TFB of the TO. The circumference of radius h_max is represented in blue. This figure shows the case of the TO around Callisto.

1. The TFB of the TO is propagated from the initial state $\mathbf{x}_0^i$ $(i = 3, 4)$, according to some time discretization.

2. We select a set of states $\mathbf{x}_i = (\mathbf{r_i}, \mathbf{v_i})$ (being $\mathbf{r_i} = (x_i, y_i)$ and $\mathbf{v_i} = (\dot{x}_i, \dot{y}_i)$) along the TFB, such that

$$r_i - r_M < h_\mathrm{max}, \tag{4.14}$$

being r_i the magnitude of $\mathbf{r}_i$, r_M the equatorial radius of the moon M and h_max an arbitrary value of maximum altitude (see Fig. 4.7). Clearly $card(\{\mathbf{x}_i\})^1$ depends on h_max and the discretization used to propagate the TFB.

3. For each $\mathbf{v_i}$ we consider the corresponding flight path angle γ_i (see Fig. 4.8). γ_i is varied in a range $\Delta\gamma_i = [\gamma_i - \delta\gamma, \gamma_i + \delta\gamma]$ $(\delta\gamma > 0)$ according to some discretization. We call $\mathbf{v}_{ij}$ the jth velocity direction provided by $\gamma_j \in \Delta\gamma_i$.

4. In turn, we let the magnitude of each velocity vector $\mathbf{v}_{ij}$ vary in a given range $\Delta v_{ij} = [v_{ij} - \delta v^-, v_{ij} + \delta v^+]$ $(\delta v^-, \delta v^+ > 0)$ with some dis-

---

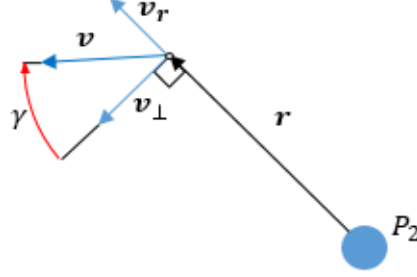[1]the symbol $card(S)$ represents the cardinality of the set S.

Figure 4.8: The flight path angle γ of a spacecraft orbiting around P$_2$ with velocity $\mathbf{x}$ is defined as $\gamma = \arctan \dfrac{v_r}{v_\perp}$, being v_r and $v_\perp$ the radial and perpendicular components of $\mathbf{v}$, respectively.

cretization. We call $\mathbf{v}_{ijk}$ the kth magnitude of the jth velocity direction associated with the point $\mathbf{r_i}$.

5. Each state $\mathbf{s}_{ijk} = (\mathbf{r_i}, \mathbf{v_{ijk}})$ is integrated over three revolutions around the moon. If the trajectory escapes the P$_2$ region, the state $\mathbf{s}_{ijk}$ is rejected. Otherwise, we call ΔV_{ijk}^1 the magnitude of the difference in velocity to change the state from $\mathbf{x}_i$ to $\mathbf{s}_{ijk}$. We call d_n $(n = 1, 2, 3)$ the distance between the endpoint of the nth revolution and $\mathbf{r}_i$ (see Fig. 4.9).

6. If $d_N < d_{\max} \quad \forall N = 1, 2, 3$, with $d_{\max}$ arbitrary small, the state $\mathbf{s_{ijk}}$ is stored in the database $\mathcal{D}_1$. Moreover, we call T_{ijk}^n the time of flight to complete the nth revolution. Since $d_{\max}$ is small, $T_{ijk}^1 \approx T_{ijk}^2 \approx T_{ijk}^3$.

7. We define the nondimensional *time performance parameter* η_{ijk} as

$$\eta_{ijk} = \frac{T_{\mathrm{reph}}}{T_{ijk}^1} - \mathrm{round}\left(\frac{T_{\mathrm{reph}}}{T_{ijk}^1}\right), \tag{4.15}$$

where the operator $\mathrm{round}(a)$ rounds a to the nearest integer. From this definition it follows that $\eta_{ijk} \in [-1/2, 1/2]$. When $\eta_{ijk} = 0$, T_{reph} is a multiple of T_{ijk}^1. If $\eta_{ijk} > 0$ (< 0) the last revolution of the rephasing orbit will take more (less) time than that required by T_{reph}.

8. States $\mathbf{s}_{ijk} \in \mathcal{D}_1$ such that $\eta_{ijk} \in [\eta^-, \eta^+]$ (with $\eta^- < 0$, $\eta^+ > 0$ and $|\eta^-|$, $|\eta^+|$ arbitrary small) are stored in a database $\mathcal{D}_2$. Each state
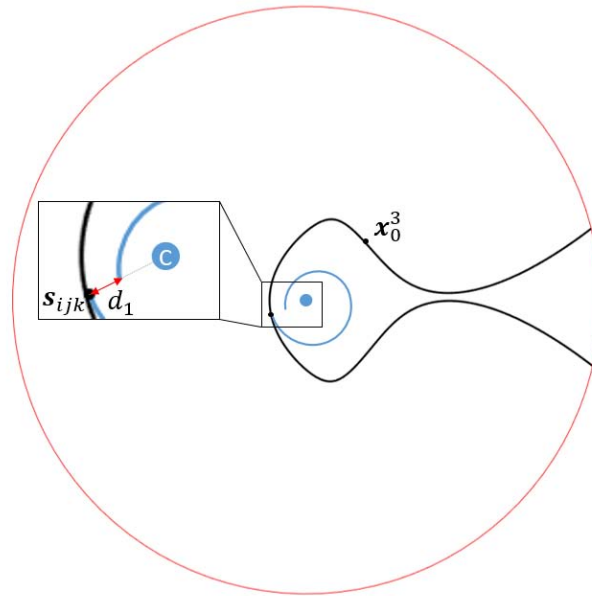
Figure 4.9: In black, the TO around Callisto generated by $\mathbf{x}_0^3 \in \mathcal{T}_2^{\min \Delta V}$. In blue, the first revolution around the moon of a possible rephasing orbit propagated from the state $\mathbf{s}_{ijk} = (\mathbf{r_i}, \mathbf{v}_{ijk})$. The distance between the endpoint of such trajectory and $\mathbf{r}_i$ is called d_1.

$\mathbf{s}_{ijk} \in \mathcal{D}_2$ is propagated over m revolutions such that

$$m = \underset{m \in \mathbb{N}}{\arg\min} \left| T_{\text{reph}}^M - \sum_{n=1}^m T_{ijk}^n - T_{ijk}^m \right|, \tag{4.16}$$

where $\arg\min_x f(x) := \{x \mid \forall y : f(y) \geq f(x)\}$. In other words, the states $\mathbf{s}_{ijk} \in \mathcal{D}_2$ are propagated until approximately one more revolution is needed to reach the required rephasing time.

9. The $(m+1)^{th}$-revolution is propagated over a rotation of π rad around the moon; we call $\mathbf{s}_{ijk}^f = (\mathbf{r}_{ijk}^f, \mathbf{v}_{ijk}^f)$ the state at this point. Let T_{ijk}^f be the total time of flight from the initial state $\mathbf{s}_{ijk}$ until $\mathbf{s}_{ijk}^f$. A single-shooting algorithm with control on the velocity is used to target the initial position $\mathbf{r_i}$ from $\mathbf{v}_{ijk}^f$ with a constraint on the time of flight (see Appendix G for a detailed description of this algorithm). In particular, the time of flight $\text{TOF}_{\text{shooting}}$ required by the algorithm to close the rephasing orbit is:

$$\text{TOF}_{\text{shooting}} = T_{\text{reph}}^M - T_{ijk}^f. \tag{4.17}$$

The output of the single-shooting algorithm is the velocity $\mathbf{v}_{ijk}^{\text{shooting}}$ necessary to reach $\mathbf{r_i}$ from $\mathbf{v}_{ijk}^f$. The required ΔV for this manoeuvre is:

$$\Delta V_{ijk}^2 = \left\| \mathbf{v}_{ijk}^{\text{shooting}} - \mathbf{v}_{ijk}^f \right\|. \tag{4.18}$$

10. Eventually we evaluate the last change in velocity ΔV_{ijk}^3 to return to the original state $\mathbf{x}_i$

11. Steps from 2 to 10 are repeated for every $i = 1, \ldots, card(\{\mathbf{x}_i\})$, $j = 1, \ldots, card(\Delta\gamma_i)$, $k = 1, \ldots, card(\Delta v_{ij})$.

12. The rephasing orbit minimizing $\Delta V_{ijk}^{\text{TOT}} = \Delta V_{ijk}^1 + \Delta V_{ijk}^2 + \Delta V_{ijk}^3$ is chosen.

This algorithm is used to find the optimal rephasing orbit around Callisto and Ganymede using the parameters listed in Table 4.3. The available rephasing orbits are represented in Fig. 4.11 by means of the two parameters $\Delta V_{ijk}^{\text{TOT}}$ and η, for $\eta \in [\eta^-, \eta^+]$. The cost of the minimum-ΔV^{TOT} rephasing orbits are:

$$\Delta V_{\text{reph}}^C = 104.539 + 13.578 + 92.039 = 210.157\,\text{m s}^{-1}, \tag{4.19a}$$

$$\Delta V_{\text{reph}}^G = 158.562 + 30.889 + 138.577 = 328.038\,\text{m s}^{-1}. \tag{4.19b}$$

The optimal rephasing orbits are showed in Fig. 4.11 in the respective SRF.

		Ganymede	Callisto
n		1	1
T_{reph}	[days]	16.77	12.11
h_{max}	[km]	20000	15000
$\delta\gamma$	[degree]	3	3
$card(\Delta\gamma_i)$		100	100
δv^-	[km s^{-1}]	$0.08v_{ij}$	$0.08v_{ij}$
δv^-	[km s^{-1}]	$0.2v_{ij}$	$0.2v_{ij}$
d_{max}	[NU]	1×10^{-4}	1×10^{-4}
η^-		-0.1	0.1
η^+		-0.1	0.1

Table 4.3: Parameters used in the algorithm to find the optimal rephasing orbit around Ganymede and Callisto.
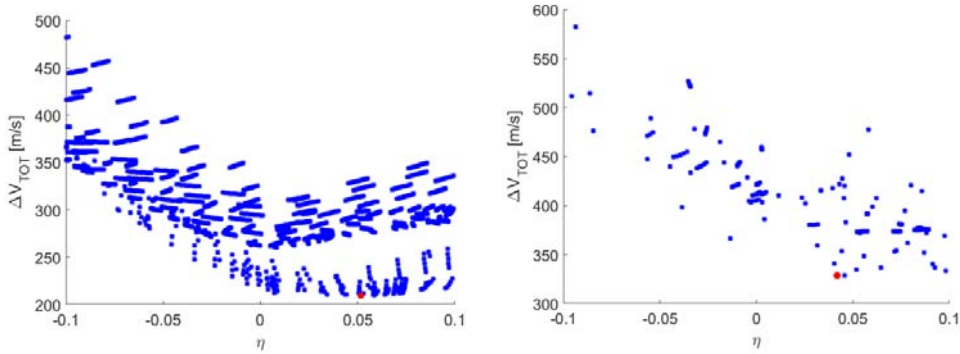
(a) *Rephasing orbits around Callisto*   (b) *Rephasing orbits around Ganymede*

Figure 4.10: Available rephasing orbits around Callisto (left) and Ganymede (right) as a function of $\Delta V_{ijk}^{\mathrm{TOT}}$ and η. The two minimum-ΔV rephasing orbits are marked with a red dot.
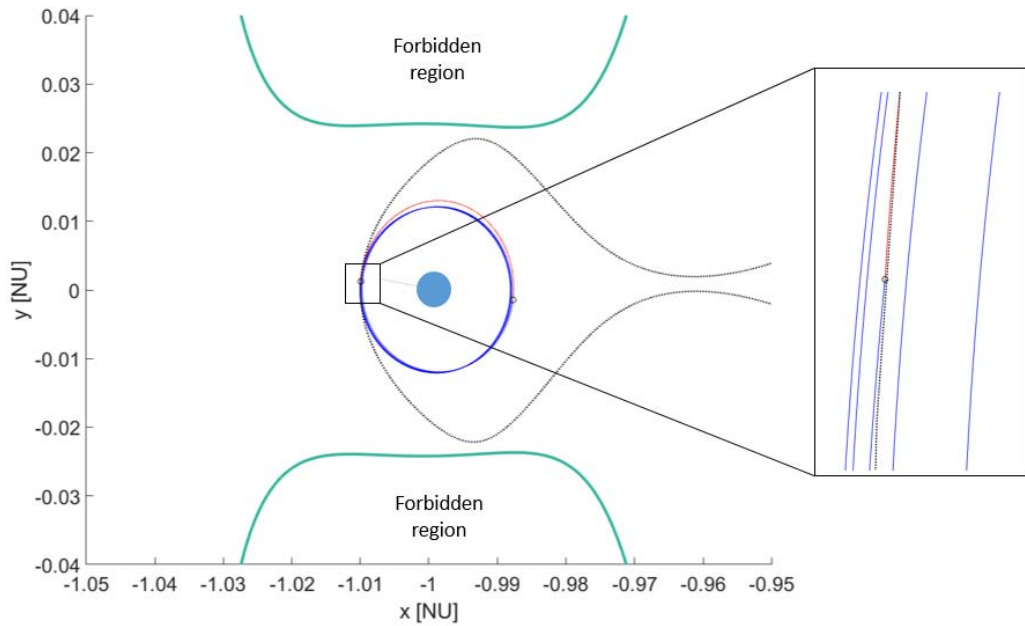
(a) *Optimal rephasing orbit around Callisto.*
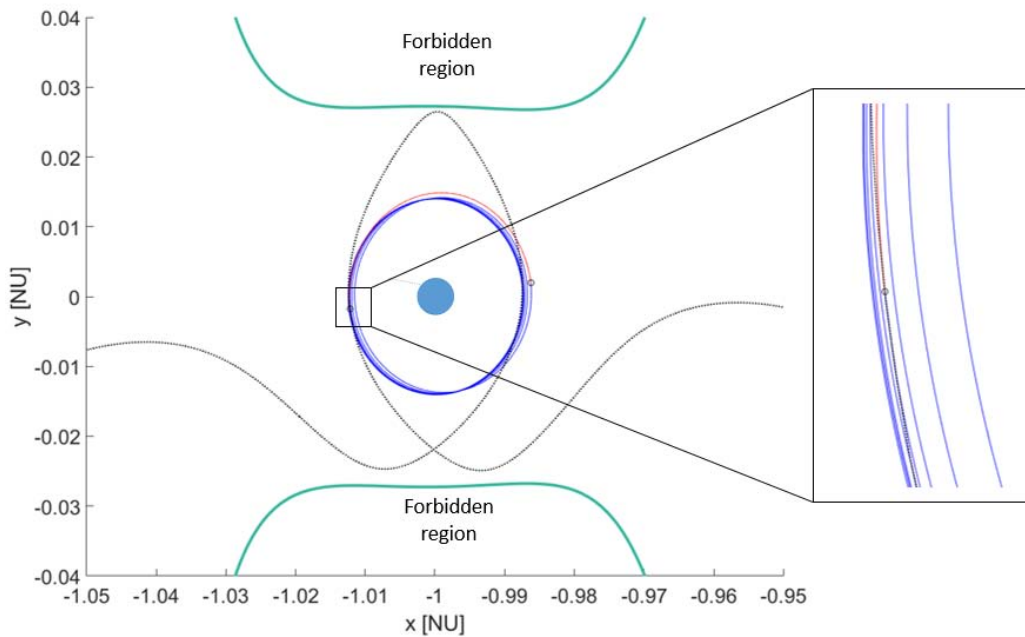
(b) *Optimal rephasing orbit around Ganymede.*

Figure 4.11: Optimal rephasing orbits around Ganymede (top) and Callisto (bottom). The original TO is represented as a black dotted trajectory. The rephasing orbit is showed as a continuous blue line from $\mathbf{s}_{ijk}$ to $\mathbf{s}_{ijk}^{f}$. The remaining part of the rephasing orbit, where the single-shooting algorithm is applied to link $\mathbf{s}_{ijk}^{f}$ and $\mathbf{r}_i$, is represented with a continuous red line. In each case, on the right-side of the figure, a close-up view around $\mathbf{r}_i$ is shown. The black circles mark the points where the ΔVs are applied. The sizes of the moons are not to scale.

4.4 Analysis of the results

The total ΔV of the tour is calculated by summing the results of Eqs. (4.9) and (4.19):

$$\Delta V = 4.227 + 0.210 + 0.328 = 4.765 \, \mathrm{km \, s^{-1}}. \qquad (4.20)$$

Similarly, the total TOF is:

$$\mathrm{TOF} = 47.058 + 16.767 + 12.113 = 75.938 \, \mathrm{days}. \qquad (4.21)$$

The resulting outward journey is showed in Fig. 4.13; the inward journey is represented in Fig. 4.14. Figs. 4.15 show the altitude and velocity of the spacecraft with respect to time inside the four intra-moon regions. Velocities are given in the moon-centred inertial reference frames. As represented in these figures, the velocity of the spacecraft never exceeds $1.1 \, \mathrm{km \, s^{-1}}$, and the maximum velocity is reached at the minimum-altitude point. For the sake of comparison, the velocity at the periapsis of a flyby-hyperbola ranges between $1.4 \, \mathrm{km \, s^{-1}}$ and $1.7 \, \mathrm{km \, s^{-1}}$, when the hyperbolic excess speed is calculated using Hohmann transfers between consecutive moons and the periapsis of the hyperbola is equal to the minimum-altitude reached by the given TO. The time of flight spent inside the Laplace sphere in the case of a flyby-hyperbola is between 1 and 6 hours; in the case of TOs this time is between 7 hours and 2.3 days. These values are further increased when rephasing orbits are considered, thus providing more opportunities for scientific exploration around the moons.

The time and ΔV performances of the trajectory obtained must be compared with the state of the art in this field. The size of the manoeuvres for each inter-moon connection is about $1 \, \mathrm{km \, s^{-1}}$. This value is larger than the ΔV-budget of [Lantoine and Russell, 2011] and [Lantoine et al., 2011]. However, our method generates solutions in the class of high-ΔV, low-time-of-flight transfers. Our ΔV budget can be directly compared with the PGT reported in [Gómez et al., 2004] (from Ganymede to Europa with a cost of $1.2 \, \mathrm{km \, s^{-1}}$) and with [Campagnola et al., 2014] (from Callisto to Europa with $1.1 \, \mathrm{km \, s^{-1}}$). There is agreement between ΔV budgets found in this thesis and those reported in the quoted papers. The added value presented in this work is twofold. Firstly we identified the minimum-ΔV solution of this category using a method which combines efficiency and accuracy. Secondly, we reduced significantly the time of flight in the inter-moon region, with respect to other methods employing IMs and multiple flybys. This is a merit of TOs which do not spend any additional time winding around the PLOs at the beginning and the end of the moon-to-moon transfer. For the sake of comparison, the time of flight required for the sole connection between Europa and Ganymede found in this study is about 4 days (Eq. (4.10)), while

in [Gómez et al., 2004] the transfer between the same moons employing IMs requires 25 days. It is worth recalling that the intense particle radiation environment characterizing the Jovian magnetosphere puts serious limitations to the feasibility of long-duration tours. Therefore, our low-time-of-flight tour is in agreement with the requirement of reducing the accumulation of radiation dose.

Besides, our large manoeuvres are perfectly attainable by means of electrical thrusters, which nowadays constitute a mature and widely used spacecraft technology. In this context, the trajectory would become a long spiral between the orbits of the moons to be connected. The solution presented here for each moon-to-moon connection would constitute the initial guess, and the initial relative lunar configuration would be employed to generate the boundary conditions. In terms of propellant consumption, the resulting low-thrust transfers would result in some tens of $m\,s^{-1}$.

Lastly, exploiting the natural dynamics provided by the CR3BP, more constraints can be added to the TO morphology inside the intra-moon space of the moons; for example the requirement of more than one revolution around the moon can be introduced. In Fig. 4.12 we provide an example of two TOs completing five revolutions around Europa and Ganymede, while verifying the remaining set of constraints $\mathcal{C}$ defined in Sect. 4.1. No additional ΔV is required for these trajectories.
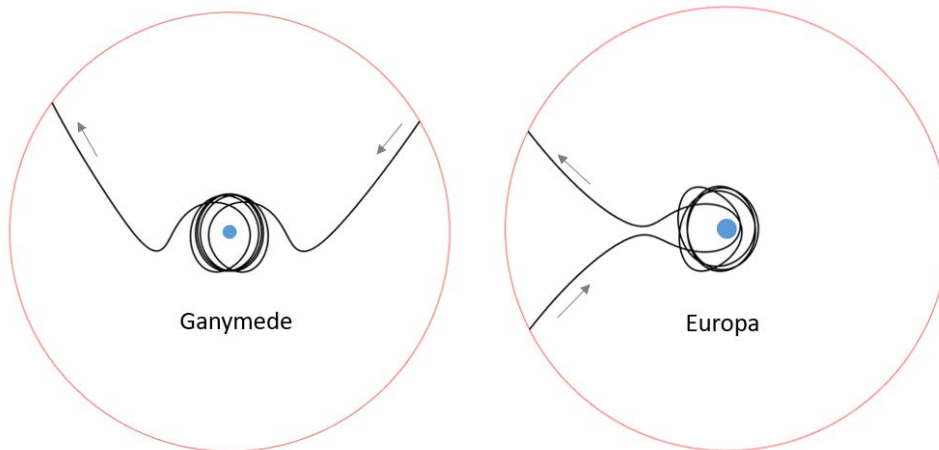
(a) *TO completing five revolutions around Ganymede.*

(b) *TO completing five revolutions around Europa.*

Figure 4.12: Examples of TOs making five revolutions in the intra-moon space of Ganymede (left) and Europa (right). The CI of the two moons is represented in red. The arrows indicate the time direction of the TO. These trajectories are found using the same method described Sect.4.1 and do not require any additional ΔV.
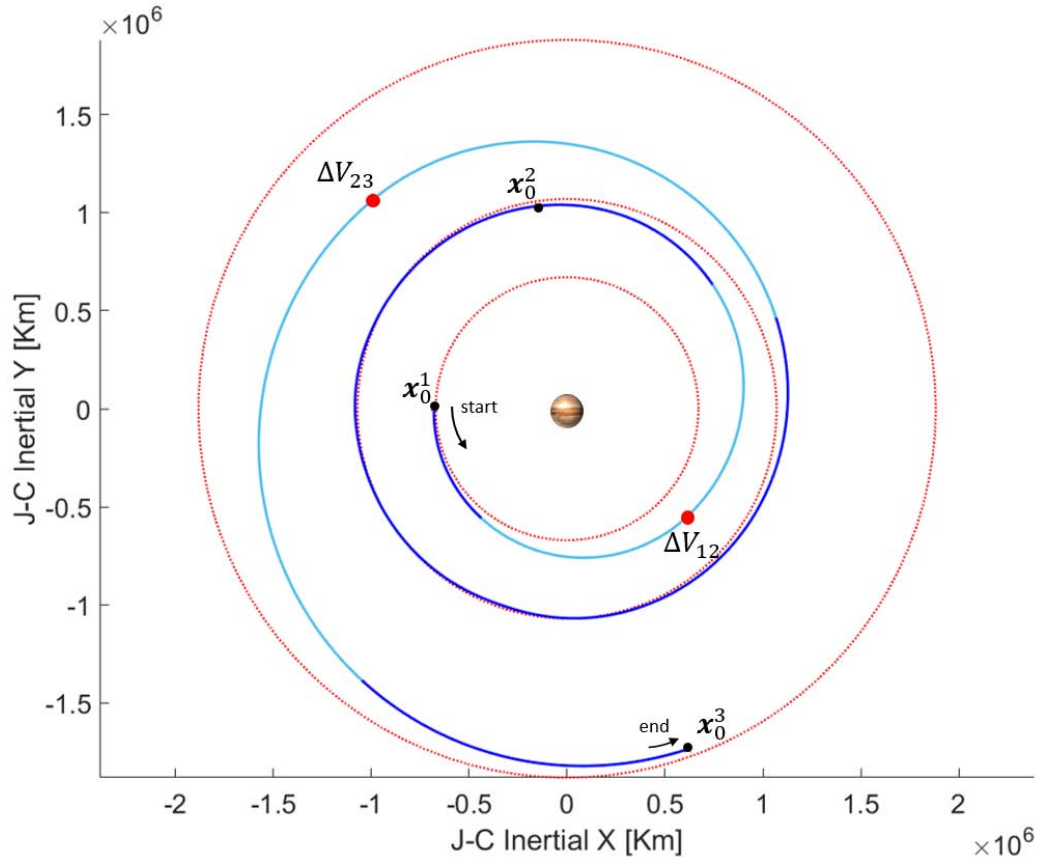
Figure 4.13: The outward journey of the Galilean moons provided by initial conditions $\mathcal{T}_2^{\min \Delta V}$ as viewed from the Jupiter-centred IRF. The orbits of the three moons are represented as dotted circles. The intra-moon branches are represented in blue, the inter-moon branches are represented in light-blue. The trajectory connects sequentially the states $\mathbf{x}_0^1$, $\mathbf{x}_0^2$ and $\mathbf{x}_0^3$. The locations of the required ΔV_{12} and ΔV_{34} are represented with red circles.
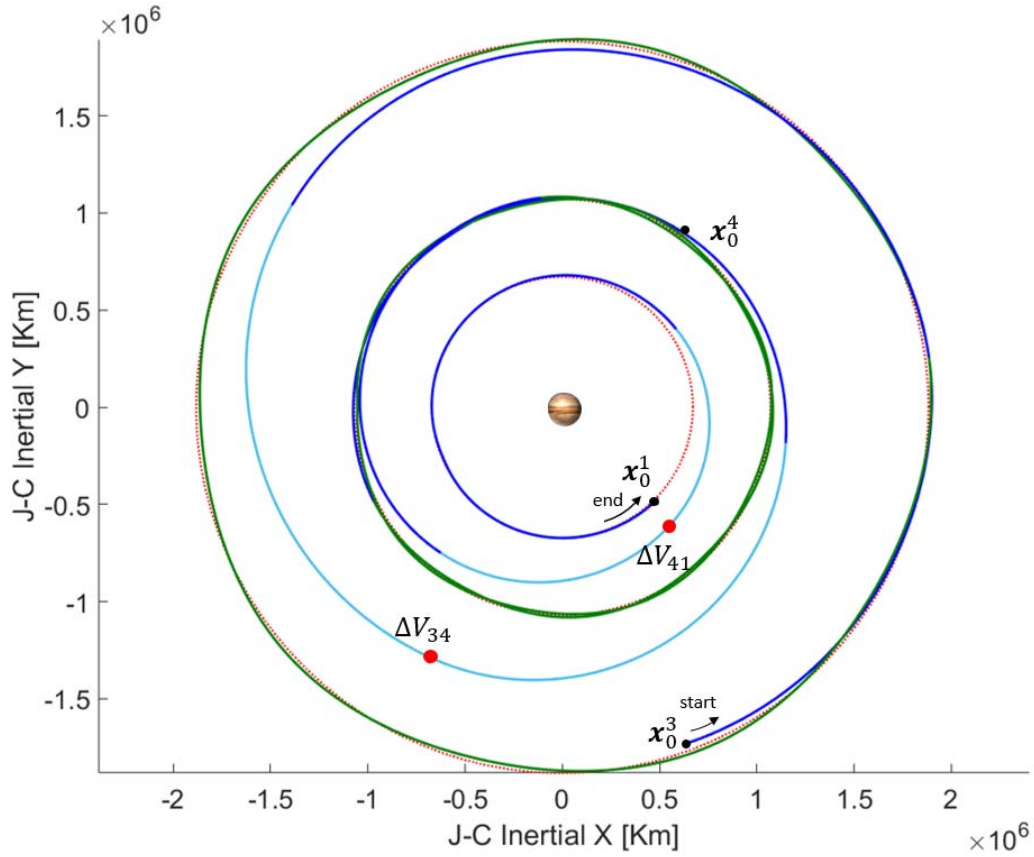
Figure 4.14: The inward journey of the Galilean moons provided by initial conditions $\mathcal{T}_2^{\min \Delta V}$ as viewed from the Jupiter-centred IRF. The orbits of the three moons are represented as dotted circles. The intra-moon branches are represented in blue, the inter-moon branches in light-blue, the rephasing trajectories in green. The trajectory connects sequentially the states $\mathbf{x}_0^3$, $\mathbf{x}_0^4$ and $\mathbf{x}_0^1$. The locations of the required ΔV_{34} and ΔV_{41} are represented with red circles.
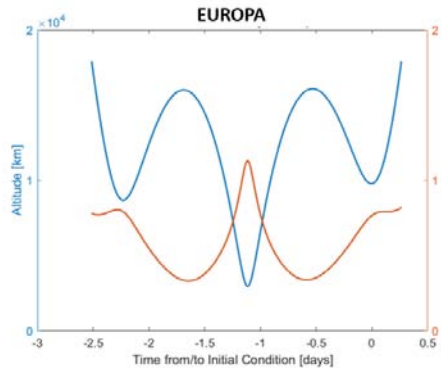
(a) *TO around Europa.*
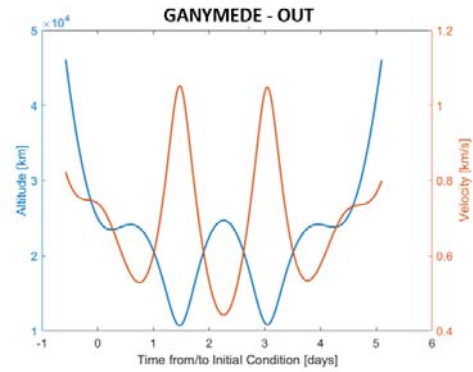
(b) *TO around Ganymede (outward journey).*
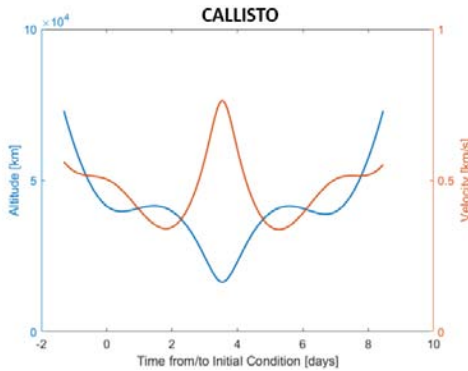
(c) *TO around Callisto.*
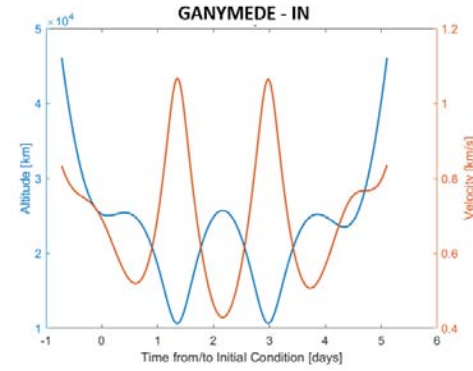
(d) *TO around Ganymede (inward journey).*

Figure 4.15: Altitude (blue) and velocity (red) of TOs of the set $\mathcal{T}_2^{\min \Delta V}$ in each moon-centred inertial reference frame. The maximum velocity never exceeds $1.1 \, \mathrm{km \, s^{-1}}$ in every case and such velocity is reached at the minimum altitude.

Chapter 5

Conclusions

The method presented in this thesis allows to determine the minimum-cost direct low-energy trajectories between consecutive moons of a planetary system. This method has been repeatedly applied to find a tour of the Galilean moons Europa, Ganymede and Callisto.

The Keplerian approximation employed in the inter-moon space offers conspicuous savings in computing time over traditional approaches based on intersecting invariant manifold trajectories. The computations are entirely analytical and explicit and no numerical approximation is made (except for IMs and TOs propagation).

The minimum-cost solution requires the occurrence of specific values of α_0 to connect two consecutive states $\mathbf{x}_0^i$ and $\mathbf{x}_0^j$, i.e., specific relative orbital geometries between the moons at the time of departure from the state $\mathbf{x}_0^i$. These values affect the initial phases of the moons at the beginning of the outward journey as well as the rephasing times required during the inward journey. Solutions with cost above the absolute minimum may be chosen if they correspond to more convenient values of α_0 relative to the mission requirements. Hence, in general, the method lends itself to trade-off between cost and other parameters (including time of flight).

The cost to link four $\mathcal{C}$-connected states is at the level of $1\,\mathrm{km\,s^{-1}}$ in each inter-moon connection. This value is large in comparison with those obtained with the high-energy patched conics published in the open literature. However different methods are used in the two cases. In this case we are dealing with low-energy transfers, i.e., the resulting trajectories between the moons are direct, hence faster. In addition, we replaced invariant manifolds, used in the original method [Fantino and Castelli, 2016b], with transit orbits, which further reduce the time of flight in each moon-to-moon connection. In fact, they do not wind around the same-energy PLO as invariant-manifold trajectories do. Moreover, in this context, the solution yields results in agreement

95

with previous studies [Gómez et al., 2004, Campagnola et al., 2014] and it also identifies the minimum-cost solution of this category. Indeed, for this application, it is impossible to further reduce the ΔV in the inter-moon connection to values lower than $1 \, \text{km} \, \text{s}^{-1}$. Besides, such large manoeuvres are perfectly attainable by means of electrical thrusters, which nowadays constitute a mature and widely used spacecraft technology. The conversion from the impulsive manoeuvres found in this work to equivalent low-thrust arcs is currently under development.

The key feature of the analytical method here presented is the tangency configuration of the inter-moon Keplerian ellipses associated with the minimum-ΔV connection between consecutive moons. This configuration can be found because only one degree of freedom exist in the coupled CR3BP, i.e., the relative phase α_0 between the x-axes of the two SRFs. In particular, instead of scanning all the possible values of α_0 only two values are selected, i.e., the ones which guarantee the tangency configuration between the involved inter-moon ellipses. In turn, α_0 dictates the relative phase between the moons at the beginning of the connection. When the four moon-to-moon connections are linked together, we proved that parking orbits (that we called rephasing orbits) around Callisto and Ganymede are necessary to match the phases of the moons at the end of the outward journey with the optimal angles α_0 associated to the inward journey. Such orbits have been computed in the framework of the CR3BP for the two Jupiter-moon systems. ΔVs required to insert the spacecraft in these orbits range from $210 \, \text{m} \, \text{s}^{-1}$ to $330 \, \text{m} \, \text{s}^{-1}$. Despite the need for additional fuel, rephasing orbits actually have two pros. Firstly, more time can be spent in the vicinity of the moons at low altitudes, secondly they provide more flexibility to the method. In fact, such trajectories can be employed around any moon, thus allowing to repeat the tour more than once.

Our choice to study the planar problem was justified by the fact that the relative inclinations between the orbital planes of the Galilean moons never exceeds one degree. In real cases, however, the most interesting observation orbits around the moons are characterized by non-zero inclinations with respect to the orbital plane. For this reason additional ΔVs could be required to change the orbital inclinations in case of an orbit insertion around a moon.

A final remark on the domain of applicability of the method here presented is due. The Keplerian approximation has been illustrated here in the context of the low-energy transfers between Jovian moons, but its capability is much wider. It can be employed in any context in which a dominant center of attraction is present: for instance, in the realm of geocentric orbits, whenever a rendezvous or an orbit change is sought, in the optimization of high-energy patched-conics tours of multi-moon systems, and in the design

of interplanetary deep space manoeuvres.

I would like to mention that this thesis has been presented to the XV workshop in Celestial Mechanics which took place in Manresa, Spain. Additionally, a paper about this work is under development for submission to Acta Astronautica.

Appendices

Appendix A

Lagrange quintic equation

We recall here Eq. (2.31)

$$u^5 + u^4(\mu - 3) + u^3(3 - 2\mu) - u^2\mu + 2\mu u - \mu = 0, \qquad (A.1)$$

where

$$u = x - \mu + 1. \qquad (A.2)$$

In this section we prove that this 5th-order equation has only one positive real solution, which is related to the x-coordinate of the Lagrangian point L_1. The case for the other points L_2 and L_3 can be treated similarly.

To achieve that goal we recall the *Sturm chains* and the Sturm's theorem. A Sturm chain is a finite sequence of polynomials:

$$p_0, p_1, \ldots, p_m \qquad (A.3)$$

of decreasing degree which satisfies the following properties:

- $p_0 = p$ is square free (i.e. it has no repeated roots),

- if $p(\xi) = 0$ then $\text{sign}(p_1(\xi)) = \text{sign}(p_1'(\xi))$,

- if $p_i(\xi) = 0$ for $0 < i < m$ then $\text{sign}(p_{i-1}(\xi)) = -\text{sign}(p_{i+1}(\xi))$,

- p_m does not change in sign.

We can choose the following polynomials to respect the above mentioned

conditions:

$$p_0(x) := p(x), \tag{A.4}$$

$$p_1(x) := p'(x), \tag{A.5}$$

$$p_2(x) := -\text{rem}(p_0, p_1), \tag{A.6}$$

$$p_3(x) := -\text{rem}(p_1, p_2), \tag{A.7}$$

$$\vdots$$

$$p_m(x) := -\text{rem}(p_{m-2}, p_{m-1}), \tag{A.8}$$

where $\text{rem}(p_i, p_j)$ is the remainder of the polynomial division of p_i by p_j and m is the minimal number of divisions required to obtain a zero reminder ($m \leq \deg(p)$). According with Sturm theorem, given a Sturm chain $p_0, \ldots, p_m$ of a polynomial p ad denoting with $\sigma(\xi)$ the number of sign changes (ignoring zeros) in the sequence $p_0(\xi), p_1(\xi), \ldots, p_m(\xi)$ then the number of distinct roots of p in the half open interval $(a, b]$ (with $a < b$) is $\sigma(a) - \sigma(b)$. If p is not square free, the same conclusion holds whenever neither a or b is a multiple root of b. However, if we consider $]-\infty, +\infty[$ as interval, the square free condition does not hold.

In this case we apply the Sturm theorem to find the number of real roots of equation (A.1) in the interval $[-\infty, +\infty[$. To evaluate the polynomial behaviour at infinity, only the coefficient of the higher-degree term needs to be taken into account. For this reason, from p_2 on, only the first coefficient is reported. Thus, the Sturm chain results:

$$p_0 = u^5 + u^4(\mu - 3) + u^3(3 - 2\mu) - u^2\mu + 2\mu u - \mu, \tag{A.9}$$

$$p_1 = 5u^4 + 4(\mu - 3)u^3 + 3(3 - 2\mu)u^2 - 2\mu u + 2\mu, \tag{A.10}$$

$$p_2 = \left[\mu + 2\mu \left(\frac{\mu}{25} - \frac{3}{25} \right) \right] u^3 + \ldots, \tag{A.11}$$

$$p_3 = \left[\frac{25 \, (12\,\mu^4 - 42\,\mu^3 - 96\,\mu^2 + 45\,\mu)}{4\,(2\,\mu^2 - 2\,\mu + 3)^2} \right] u^2 + \ldots, \tag{A.12}$$

$$p_4 = \left[\frac{4\,\mu\,(\mu - 1)\,(2\,\mu^2 - 2\,\mu + 3)^2\,(-80\,\mu^4 + 112\,\mu^3 + 1174\,\mu^2 - 720\,\mu + 729)}{25\,(-20\,\mu^4 + 40\,\mu^3 + 220\,\mu^2 - 240\,\mu + 81)^2} \right] u +$$

$$+ \ldots, \tag{A.13}$$

$$p_5 = \frac{25\,(-20\,\mu^4 + 40\,\mu^3 + 220\,\mu^2 - 240\,\mu + 81)^2}{64\,(-80\,\mu^6 + 240\,\mu^5 + 822\,\mu^4 - 2044\,\mu^3 + 3807\,\mu^2 - 2745\,\mu + 1458)^2} + \tag{A.14}$$

$$+ \frac{(-448\,\mu^4 + 896\,\mu^3 + 6032\,\mu^2 - 6480\,\mu + 6561)}{64\,(-80\,\mu^6 + 240\,\mu^5 + 822\,\mu^4 - 2044\,\mu^3 + 3807\,\mu^2 - 2745\,\mu + 1458)^2} +$$

$$+ \ldots. \tag{A.15}$$

Evaluating p_1, p_2, p_3, p_4, p_5 to $-\infty$ and $+\infty$, assuming $\mu \ll 0$ produces the sequence of signs $(- + + + - +)$ and $(+ + - + + +)$ respectively, thus the sign variations are $\sigma(-\infty) = 2$ and $\sigma(+\infty) = 1$: the total number of real roots is $\sigma(-\infty) - \sigma(+\infty) = 2 - 1 = 1$. Considering now the first polynomial (A.9) we notice that $\lim_{u \to -\infty} p_0 = -\infty$, $\lim_{u \to +\infty} p_0 = \infty$ and $p_0(u = 0) - \mu < 0$. Therefore, the only real root of this quintic equation is positive. From the variable conversion (A.2) it turns out that $x > \mu + 1$, i.e. the solution lies on the right of the smaller primary.

Appendix B

Second-order partial derivatives of the effective potential

We list here the second-order partial derivatives of the effective potential Ω (Eq. (2.33)):

$$\Omega_{xx} = 1 - \frac{1-\mu}{r_1^3} - \frac{\mu}{r_2^3} + \frac{3(1-\mu)(x-\mu)^2}{r_1^5} + \frac{3\mu(x+1-\mu)^2}{r_2^5}, \tag{B.1}$$

$$\Omega_{xy} = \frac{3(1-\mu)(x-\mu)y}{r_1^5} + \frac{3\mu(x+1-\mu)y}{r_2^5}, \tag{B.2}$$

$$\Omega_{xz} = \frac{3(1-\mu)(x-\mu)z}{r_1^5} + \frac{3\mu(x+1-\mu)z}{r_2^5}, \tag{B.3}$$

$$\Omega_{yy} = 1 - \frac{(1-\mu)}{r_1^3} - \frac{\mu}{r_2^3} + \frac{3(1-\mu)y^2}{r_1^5} + \frac{3\mu y^2}{r_2^5}, \tag{B.4}$$

$$\Omega_{yx} = \Omega_{xy}, \tag{B.5}$$

$$\Omega_{yz} = \frac{3(1-\mu)yz}{r_1^3} + \frac{3\mu yz}{r_2^5}, \tag{B.6}$$

$$\Omega_{zz} = -\frac{(1-\mu)}{r_1^3} - \frac{\mu}{r_2^3} + \frac{3(1-\mu)z^2}{r_1^5} + \frac{3\mu(x+1-\mu)}{r_2^5}, \tag{B.7}$$

$$\Omega_{zx} = \Omega_{xz}, \tag{B.8}$$

$$\Omega_{zy} = \Omega_{yz}. \tag{B.9}$$

B.1 Sign of the second-order partial derivatives at the collinear equilibrium points

The characteristic equation (2.71) of the linearised system (2.65) is here recalled in (x, y, z) coordinates:

$$(\lambda^2 - \Omega^0_{zz})[(\lambda^4) + \lambda^2(4 - \Omega^0_{xx} - \Omega^0_{yy}) + \Omega^0_{yy}\Omega^0_{xx}] = 0, \qquad (B.10)$$

where Ω^0_{pq} are the second-order partial derivatives $\frac{\partial^2 \Omega}{\partial p \partial q}$ of the potential (2.33) in the collinear point of interest. To gain more insight into the stability of the collinear point the signs of Ω_{xx}, Ω_{yy} and Ω_{zz} are required.

In the collinear points, $y = z = 0$. Therefore, from Eq. (B.7) it is clear that $\Omega^0_{zz} < 0$. Examining the expression of Ω^0_{xx} and Ω^0_{yy} from Eqs. (B.1) and (B.4) we can rewrite this term in the collinear points as:

$$\Omega_{xx}(x, 0, 0) = 1 + \frac{2(1 - \mu)}{r_1^3} + \frac{2\mu}{r_2^3}, \qquad (B.11)$$

$$\Omega_{yy}(x, 0, 0) = 1 - \frac{1 - \mu}{r_1^3} - \frac{\mu}{r_2^3}, \qquad (B.12)$$

being $r_1 = |x - \mu|$ and $r_2 = |x + 1 - \mu|$ evaluated at L$_1$, L$_2$ and L$_3$. It is apparent that $\Omega^0_{xx} > 0$. The sign of the remaining term Ω_{yy} is taken into account separately for the three collinear equilibrium points. Recall from Eq. (2.36) that all first partials are zero in the equilibrium points. In particular:

$$\Omega_x = x - \frac{(1 - \mu)(x - \mu)}{|x - \mu|^3} - \frac{\mu(x + 1 - \mu)}{|x + 1 - \mu|^3} = 0. \qquad (B.13)$$

The discussion that follows is based on [Szebehely, 2012].

L$_1$. For this point $x - \mu < 0$ and $x + 1 - \mu > 0$. Therefore $r_1 = |x - \mu| = \mu - x$ and $r_2 = |x + 1 - \mu| = x + 1 - \mu$. Hence we can rewrite Eq. (B.13) as:

$$x + \frac{1 - \mu}{r_1^2} - \frac{\mu}{r_2^2} = 0, \qquad (B.14)$$

from which:

$$\frac{(1 - \mu)}{r_1^2} = \frac{\mu}{r_2^2} - x. \qquad (B.15)$$

Substituting this term into Eq. (B.12) yields:

$$\Omega^0_{yy} = 1 - \frac{1}{r_1}\left(\frac{\mu}{r_2^2} - x\right) - \frac{\mu}{r_2^3} \qquad (B.16)$$

$$= 1 - \frac{1}{r_1}\left(\frac{\mu}{r_2^3} - x\right), \qquad (B.17)$$

being $r_1 + r_2 = 1$. By replacing $x = \mu - r_1$ in Eq. (B.17) the latter reduces to the form

$$\Omega_{yy}^0 = \frac{\mu}{r_1}\left(1 - \frac{1}{r_2^3}\right), \tag{B.18}$$

being $r_2 < 1$ it follows that $\Omega_{yy}^0 < 0$.

L$_2$. For this point $x - \mu < 0$ and $x + 1 - \mu < 0$. Therefore $r_1 = |x - \mu| = \mu - x$ and $r_2 = |x + 1 - \mu| = -(x + 1 - \mu)$. Hence we can rewrite Eq. (B.13) as:

$$x + \frac{1 - \mu}{r_1^2} + \frac{\mu}{r_2^2} = 0, \tag{B.19}$$

from which:

$$\frac{(1 - \mu)}{r_1^2} = -\frac{\mu}{r_2^2} - x. \tag{B.20}$$

Substituting this term into Eq. (B.12) yields:

$$\Omega_{yy}^0 = 1 - \frac{1}{r_1}\left(-\frac{\mu}{r_2^2} - x\right) - \frac{\mu}{r_2^3} \tag{B.21}$$

$$= 1 - \frac{1}{r_1}\left(\frac{\mu}{r_2^3} - x\right), \tag{B.22}$$

being $r_1 - r_2 = 1$. From this point the procedure is the same as in the case of Eq. (B.17) and thus, again, $\Omega_{yy}^0 < 0$.

L$_3$ For this point $x - \mu > 0$ and $x + 1 - \mu > 0$. Therefore $r_1 = |x - \mu| = x - \mu$ and $r_2 = |x + 1 - \mu| = x + 1 - \mu$. Hence we can rewrite Eq. (B.13) as:

$$x - \frac{1 - \mu}{r_1^2} - \frac{\mu}{r_2^2} = 0, \tag{B.23}$$

from which:

$$\frac{(1 - \mu)}{r_1^2} = x - \frac{\mu}{r_2^2}. \tag{B.24}$$

Substituting this term into Eq. (B.12) yields:

$$\Omega_{yy}^0 = 1 - \frac{1}{r_1}\left(x - \frac{\mu}{r_2^2}\right) - \frac{\mu}{r_2^3} \tag{B.25}$$

$$= 1 - \frac{1}{r_1}\left(x - \frac{\mu}{r_2^3}\right), \tag{B.26}$$

being $r_1 - r_2 = -1$. By replacing $x = \mu + r_1$ in Eq. (B.26) the latter expression reduces to the form

$$\Omega_{yy}^0 = -\frac{\mu}{r_1}\left(1 - \frac{1}{r_2^3}\right),\tag{B.27}$$

being $r_2 < 1$ it follows that $\Omega_{yy^0} < 0$.

Appendix C

Rotation of ellipses

In the following, we derive the relationship between two planet-centered ellipses generated by one and the same state vector on the CI at two different orbital phases of the moon. Let $\mathbf{x} = (x, y, \dot{x}, \dot{y})^T$ be a state vector on the CI in synodical coordinates. Denote by $\mathbf{X}_1 = (X_1, Y_1, \dot{X}_1, \dot{Y}_1)^T$ and $\mathbf{X}_2 = (X_2, Y_2, \dot{X}_2, \dot{Y}_2)^T$ two state vectors in the planet-centered inertial frame obtained by $\mathbf{s}$ when the orbital phases of the moon (i.e., the planet-centered angles from the X-axis to the location of the moon) are α_1 and α_2, respectively. Also, let Σ_1 and Σ_2 be the two elliptical orbits, with focus at the planet, passing through $\mathbf{X}_1$ and $\mathbf{X}_2$, respectively. We are going to prove that Σ_1 and Σ_2 have the same shape (i.e., they have the same semimajor axis and eccentricity) and are related by a rotation of angle $\Delta\alpha = \alpha_2 - \alpha_1$, i.e., $\omega_2 = \omega_1 + \Delta\alpha$. Denoting $R(\alpha) = \begin{bmatrix} \cos\alpha & -\sin\alpha \\ \sin\alpha & \cos\alpha \end{bmatrix}$ the rotation matrix of angle α, we show that

i) $(X_2, Y_2)^T = R(\Delta\alpha)(X_1, Y_1)^T$

ii) $(\dot{X}_2, \dot{Y}_2)^T = R(\Delta\alpha)(\dot{X}_1, \dot{Y}_1)^T$.

i) Let us consider the trajectory passing through $\mathbf{x}$ at time $t = T$ in the rotating frame. In the same time units in the planet-centered inertial frame, the trajectory is given by

$$\begin{bmatrix} X \\ Y \end{bmatrix}(t) = \kappa R(\beta(t)) \begin{bmatrix} x \\ y \end{bmatrix}(t), \qquad (\text{C.1})$$

where the constant κ is the scaling factor from normalized to physical units and $\beta(t) = \beta + t$, being β the relative phase of the rotating frame with respect

to the inertial frame at time $t = 0$. If at time $t = T$ the orbital phase of the moon is α_i ($i = 1,2$), then the phase at time $t = 0$ is $\beta_i = \alpha_i - T$. Hence, in the planet-centered inertial frame we consider two trajectories

$$\begin{bmatrix} X_1 \\ Y_1 \end{bmatrix} (t) = \kappa R(\beta_1 + t) \begin{bmatrix} x \\ y \end{bmatrix} (t), \tag{C.2}$$

and

$$\begin{bmatrix} X_2 \\ Y_2 \end{bmatrix} (t) = \kappa R(\beta_2 + t) \begin{bmatrix} x \\ y \end{bmatrix} (t). \tag{C.3}$$

Since the rotations form a group, $R(\beta_2 + t) = R(\beta_1 + t + \Delta\alpha) = R(\Delta\alpha)R(\beta_1 + t)$. Thus,

$$\begin{bmatrix} X_2 \\ Y_2 \end{bmatrix} (t) = R(\Delta\alpha) \begin{bmatrix} X_1 \\ Y_1 \end{bmatrix} (t). \tag{C.4}$$

The last expression, evaluated at $t = T$, gives $i)$. Differentiation and time units rescaling yield $ii)$. This proof neglects the distance between the center of mass of the planet-moon system and the center of the planet. In the cases under study this distance does not exceed a few tens of km.

Appendix D

Parametric cubic splines

A *cubic spline* is, by definition, a continuous piecewise cubic curve with continuous first-order and second-order derivatives. Moreover, a cubic spline is called *relaxed* if the second-order derivative is zero at each endpoint. The following considerations partially follow [McKinley and Levine, 1998].

Consider a set of N points (x_i, y_i), as represented in Fig. D.1a. We want to connect all these points through a piecewise continuous cubic function as showed in Fig. D.1b. The cubic function connecting these points will be *parametric* and defined as

$$\mathbf{P} : \Re \rightarrow \Re^2, \tag{D.1}$$

$$t \mapsto (x(t), y(t)) = (b_{1x} + b_{2x}t + b_{3x}t^2 + b_{4x}t^3, b_{1y} + b_{2y}t + b_{3y}t^2 + b_{4y}t^3). \tag{D.2}$$

At each point (x_i, y_i), $\mathbf{P}_i = (x_i, y_i)$, where $\mathbf{P}_i$ is supposed known and given by the coordinates of ith point. The total number N of points defines $N - 1$ intervals; the parameter t can vary in each interval $[i - 1, i]$ from 0 to $l_i{}^1$, being:

$$l_i = \sqrt{(x_i - x_{i-1})^2 + (y_i - y_{i-1})^2}. \tag{D.3}$$

Moreover, we assume that in each interval of the type $[i - 1, i]$

$$\mathbf{P}(0)_{[i-1,1]} = P_{i-1} = (x_{i-1}, y_{i-1}), \tag{D.4a}$$

$$\mathbf{P}(l_i)_{[i-1,i]} = P_i = (x_i, y_i). \tag{D.4b}$$

For the sake of simplicity, the following equations will refer only to one of the two components of Eq. (D.2) (the extension to the second component is immediate), thus we will evaluate

$$P(t) = b_1 + b_2 t + b_3 t^2 + b_4 t^3. \tag{D.5}$$

---

[1] In other sources you may also find a variation from 0 to 1.

(a) *Set of numbered points*   (b) *Cubic spline connecting the points*
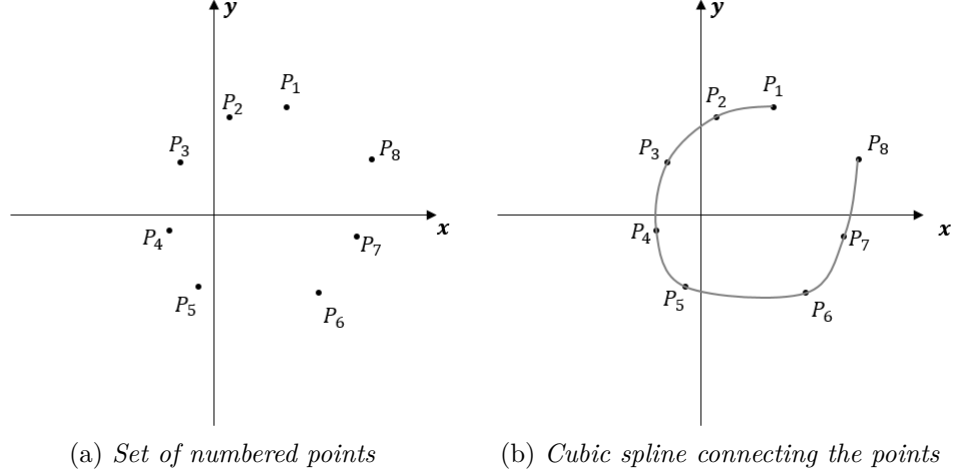
Figure D.1: An example of a parametric cubic spline.

Consider the interval $[1, 2]$. From Eq. (D.4):

$$P(t = 0) = P_1 = b_1, \tag{D.6}$$

$$P(t = l_2) = P_2 = b_1 + b_2 l_2 + b_3 l_2^2 + b_4 l_2^3. \tag{D.7}$$

Substituting Eq. (D.6) in Eq. (D.7) yields:

$$P_2 = P_1 + b_2 l_2 + b_3 l_2^2 + b_4 l_2^3. \tag{D.8}$$

The first and second-order derivatives of D.5 are respectively:

$$P'(t) = b_2 + 2b_3 t + 3b_4 t^2, \tag{D.9}$$

$$P''(t) = 2b_3 + 6b_4 t. \tag{D.10}$$

In the interval $[1, 2]$:

$$P'(t = 0) = P'_1 = b_2, \tag{D.11}$$

$$P'(t = l_2) = P'_2 = b_2 + 2b_3 l_2 + 3b_4 l_2^2. \tag{D.12}$$

Substituting (D.11) in (D.12):

$$P'(t = l_2) = P'_2 = b_2 + 2b_3 l_2 + 3b_4 l_2^2 = P'_1 + 2b_3 l_2 + 3b_4 l_2^2. \tag{D.13}$$

Considering now Eqs. (D.8) and (D.13) it is possible to write a system of two equations in the two unknowns b_3 and b_4:

$$\begin{cases} b_3 + b_4 l_2 = \dfrac{P_2 - P_1}{l_2^2} - \dfrac{P'_1}{l_2}, \\ 2b_3 + 3b_4 l_2 = \dfrac{P'_2}{l_2} - \dfrac{P'_1}{l_2}. \end{cases} \tag{D.14}$$

The solutions are:

$$b_3 = \frac{3(P_2 - P_1)}{l_2^2} - \frac{2P_1'}{l_2} - \frac{P_2'}{l_2}, \tag{D.15}$$

$$b_4 = \frac{2(P_1 - P_2)}{l_2^3} + \frac{P_1'}{l_2^2} + \frac{P_2'}{l_2^2}. \tag{D.16}$$

Hence, substituting the results into Eq. D.5 and considering Eqs. (D.6) and (D.11) provide:

$$P(t)_{[1,2]} = P_1 + P_1't + \left[\frac{3(P_2 - P_1)}{l_2^2} - \frac{2P_1'}{l_2} - \frac{P_2'}{l_2}\right]t^2+ \tag{D.17}$$

$$+ \left[\frac{2(P_1 - P_2)}{l_2^3} + \frac{P_1'}{l_2^2} + \frac{P_2'}{l_2^2}\right]t^3. \tag{D.18}$$

Now, considering a generic interval $[i - 1, i]$, Eq. (D.18) can be rewritten as:

$$P(t)_{[i-1,i]} = P_{i-1} + P_i't + \left[\frac{3(P_i - P_{i-1})}{l_i^2} - \frac{2P_{i-1}'}{l_i} - \frac{P_i'}{l_i}\right]t^2+ \tag{D.19}$$

$$+ \left[\frac{2(P_{i-1} - P_i)}{l_i^3} + \frac{P_{i-1}'}{l_i^2} + \frac{P_i'}{l_i^2}\right]t^3. \tag{D.20}$$

Considering now two adjacent intervals $[i - 1, i], [i, i + 1]$:

$$P_{[i-1,i]}''(l_i) = 2b_3 + 6b_4 l_k, \tag{D.21}$$

$$P_{[i,i+1]}''(0) = 2b_3. \tag{D.22}$$

Being $P_{[i-1,i]}''(l_i) = P_{[i,i+1]}''(0)$ (it is the same point, viewed from consecutive intervals) it follows that, considering Eqs. (D.15) and (D.16):

$$l_{i-1}P_{i-1}' + 2(l_{i-1} + l_i)P_i' + l_iP_{i+1}' = \frac{3}{l_i t_{i+1}}\left[l_k^2(P_{i+1} - P_i) + l_{k+1}^2(P_i - P_{i-1})\right]. \tag{D.23}$$

This equation can be written for each knot. In other words, it is possible to write a system of $N - 2$ equations in N unknowns $P_1', P_2', ..., P_n'$:

$$\begin{bmatrix} l_3 & 2(l_2 + l_3) & l_2 & 0 & 0 & \cdots & 0 \\ 0 & l_4 & 2(l_3 + l_4) & l_3 & 0 & \cdots & 0 \\ 0 & 0 & l_5 & 2(l_4 + l_5) & l_4 & \cdots & 0 \\ \vdots & \vdots & \ddots & \ddots & \ddots & \vdots & \vdots \\ 0 & \cdots & l_{N-2} & 2(l_{N-3} + l_{N-2}) & l_{N-3} & 0 & 0 \\ 0 & \cdots & 0 & l_{N-1} & 2(l_{N-2} + l_{N-1}) & l_{N-2} & 0 \\ 0 & \cdots & 0 & 0 & l_N & 2(l_{N-1}) & l_{N-1} \end{bmatrix} \begin{Bmatrix} P_1' \\ P_2' \\ P_3' \\ \vdots \\ P_{N-2}' \\ P_{N-1}' \\ P_N' \end{Bmatrix} =$$

$$= \left\{ \begin{array}{c} \dfrac{3}{l_2 l_3}\left[l_2^2(P_3 - P_2) + l_3^2(P_2 - P_1)\right] \\ \dfrac{3}{l_3 l_4}\left[l_3^2(P_4 - P_3) + l_4^2(P_3 - P_2)\right] \\ \vdots \\ \vdots \\ \vdots \\ \dfrac{3}{l_3 l_4}\left[l_3^2(P_4 - P_3) + l_4^2(P_3 - P_2)\right] \\ \dfrac{3}{l_{N-1}l_N}\left[l_{N-1}^2(P_N - P_{N-1}) + l_N^2(P_{N-1} - P_{N-2})\right] \end{array} \right\} \qquad (D.24)$$

The last two equations can be found by assuming that $P_{[1,2]}''(0)$ and $P_{[N-1,N]}''(l_N)$ are known. From equations (D.9) and (D.10):

$$P_{[1,2]}''(t = 0) = 2b_3 = 2\left[\frac{3(P_2 - P_1)}{l_2^2} - \frac{2P_1'}{l_2} - \frac{P_2'}{l_2}\right], \qquad (D.25)$$

$$P_{[N-1,N]}''(t = l_N) = 2b_3 + 6b_4 t_N = 2\left[\frac{3(P_N - P_{N-1})}{l_N^2} - \frac{2P_{N-1}'}{l_2} - \frac{P_N'}{l_N}\right]$$
$$+ 6\left[\frac{2(P_{N-1} - P_N)}{l_N^3} + \frac{P_{N-1}'}{l_N^3} + \frac{P_N'}{l_N^2}\right]l_N. \quad (D.26)$$

It is eventually possible to rearrange these equations to obtain the last two relations for the system (D.24) in order to obtain a $N \times N$ system; supposing both the second derivatives are zero at the endpoints (*relaxed* cubic spline) the previous equations become:

$$\begin{cases} 2P_1' + P_2{}' = \dfrac{3(P_2 - P_1)}{l_2}, \\ P_{n-1}' + 2P_n' = \dfrac{3}{l_n}(P_n - P_{n-1}). \end{cases} \qquad (D.27)$$

Equations (D.24) and (D.27) are a system of N equations in the N unknowns $\{x\} = \{P_1', P_2', ..., P_n'\}$ in the form

$$[A]\{x\} = \{b\}, \qquad (D.28)$$

and can be solved numerically. Once the unknown $\{x\}$ is found, by means of equation (D.20) it is easy to find the value of $x(t)$ and $y(t)$ in each interval.

Moreover, supposing we want to find a point (x_0, y_0) of which only one coordinate is known, the following algorithm can be used.

1. Suppose x_0 is known (the procedure for y_0 known is identical). Firstly, it is necessary to find what intervals contain the value x_0. This can be done by verifying if, in the interval $I_i = [i-1, i]$:

$$x(t = 0) \leq x_0 \leq x(t = l_i). \tag{D.29}$$

2. In each interval found in step 1, apply Newton-Raphson algorithm in order to find:

$$t_0 : x(t_0) = x_0. \tag{D.30}$$

In general, more than one t_0 can be found in each interval. In this application, being the length of the interval very small it is almost impossible to find two values of t_0 inside a single interval.

3. With the values of t_0 found at step 2, just calculate

$$y_0 = y(t_0). \tag{D.31}$$

Appendix E

Relative phase between two moons

Consider the coupled CR3BP between two consecutive moons M_1 and M_2 of a planetary system with central planet P, and a trajectory connecting a state $\mathbf{x}_1$ in the neighbourhood of P-M_1 L_2 with a state $\mathbf{x}_2$ in the neighbourhood of P-M_2 L_1. We aim at finding the relative phase between the two moons at the initial time (i.e., when P_3 leaves $\mathbf{x}_0^1$) to guarantee the connection between $\mathbf{x}_0^1$ and $\mathbf{x}_0^3$. Positive angles are measured anticlockwise from the inertial X-axis of the planet-centered IRF (see Fig. E.1). Let ω_{P1} and $\omega_{P2} = \omega_{P1} + \Delta\omega$ be the arguments of periapsis of the two inter-moon ellipses connecting the CI of M_1 and M_2, where $\Delta\omega$ is the optimal difference between the two arguments of periapsis, given in Sect.3.3. Hence, when P_3 reaches the CI of M_2, the angle swept from $\mathbf{x}_1$ is $\sigma_1 = \omega_2 + \theta_2 = \omega_1 + \Delta\omega + \theta_2$, being θ_2 the true anomaly of P_3 relative to the second inter-moon ellipse when it reaches the CI of M_2. Calling Δt_2 the time required to reach $\mathbf{x}_2$ from the CI of M_2 and

$$\delta = \arctan \frac{y_{\text{CI}}}{|x_{\text{CI}}|}, \tag{E.1}$$

with $(x_{\text{CI}}, y_{\text{CI}})$ the SRF-coordinates at the CI of M_2, the phase of M_2 when P_3 reaches its CI is:

$$\Delta\alpha_{12} = \sigma_1 + \delta + \Delta t_2 \frac{2\pi}{T_{M_2}}, \tag{E.2}$$

being T_{M_2} the period of M_2. Therefore the angle α_0 is:

$$\alpha_0 = \Delta\alpha_{12} - \omega_2 \text{TOF}_{12}, \tag{E.3}$$

being ω_2 the angular velocity of M_2 and TOF_{12} the time of flight from $\mathbf{x}_0^1$ to $\mathbf{x}_0^2$.
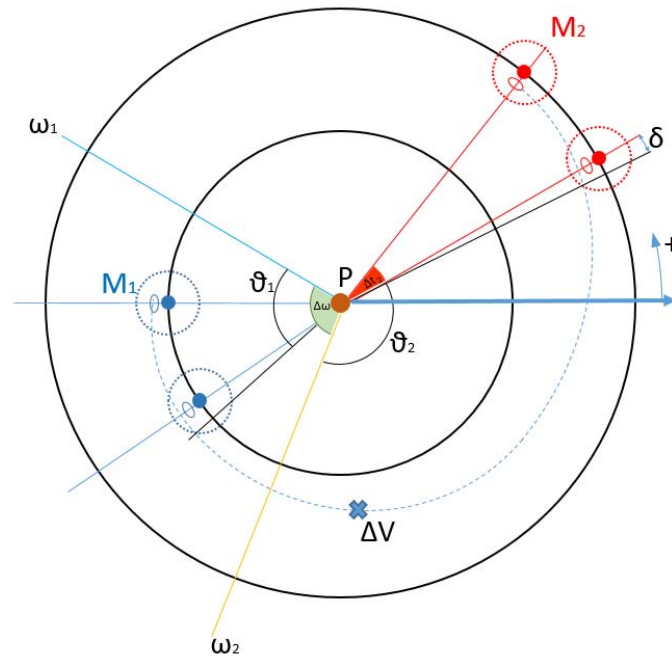
Figure E.1: A transfer from the inner moon M_1 to the outer moon M_2. The trajectory is represented as a dotted blue line. ω_1 and $\omega_2 = \omega_1 + \Delta\omega$ are the arguments of periapsis of the two inter-moon ellipses. θ_1 and θ_2 represent the true anomaly at the CI intersection of M_1 and M_2 with respect to the two apse line given by ω_1 and ω_2 respectively. δ is the angular displacement between the position of P_3 at the intersection with the CI of M_2 and the actual position of M_2 at that instant.

Appendix F

Rephasing period

We consider here the connection between Callisto and Ganymede during the inward journey. The case for the Ganymede-to-Europa connection is similar. Let $\Delta\alpha_0^{\text{out}}$ and $\Delta\alpha_0^{\text{in}}$ be the difference between the phases of Ganymede and Callisto at the end of the outward journey, and the one required to start the inward journey, the latter dictated by the optimal connection between $\mathbf{x}_0^3$ and $\mathbf{x}_0^4$. Moreover, let $\Delta\alpha^{\text{out}}(t)$ and $\Delta\alpha^{\text{in}}(t)$ be the relative phases at any time t before/after the state $\mathbf{x}_0^3$ along the TO around Callisto when the initial condition $\Delta\alpha_0^{\text{out}}$ and $\Delta\alpha_0^{\text{in}}$ is applied, respectively. Clearly:

$$\Delta\alpha^{\text{out}}(t) = \Delta\alpha_0^{\text{out}} + (\omega_G - \omega_C)t, \qquad \text{(F.1a)}$$

$$\Delta\alpha^{\text{in}}(t) = \Delta\alpha_0^{\text{in}} + (\omega_G - \omega_C)t, \qquad \text{(F.1b)}$$

with $\Delta\alpha^{\text{out}}(t) \in [0, 2\pi[$ and $\Delta\alpha^{\text{in}}(t) \in [0, 2\pi[$. Eq. (F.1b) represents the required relative phase between Callisto and Ganymede at the generic instant $t \neq 0$ (i.e., by starting the rephasing orbits from other states $\mathbf{x} \neq \mathbf{x}_0^3$). Similarly, Eq. (F.1a) represents the relative phase between the same moons at the generic instant $t \neq 0$ during the outward journey. Clearly, the rephasing time T_{reph} is such that:

$$\Delta\alpha^{\text{out}}(t + T_{\text{reph}}) = \Delta\alpha^{\text{in}}(t). \qquad \text{(F.2)}$$

Combining Eq. (F.2) with Eqs. (F.1) it follows:

$$T_{\text{reph}} = \frac{\Delta\alpha_0^{\text{out}} - \Delta\alpha_0^{\text{in}}}{\omega_C - \omega_G}. \qquad \text{(F.3)}$$

Since $\Delta\alpha_0^{\text{out}} - \Delta\alpha_0^{\text{in}} = \Delta\alpha_0^{\text{out}} - \Delta\alpha_0^{\text{in}} + 2\pi n, \ (n \in \mathbb{N})$, we can rewrite Eq. (F.3) as

$$T_{\text{reph}} = \frac{\Delta\alpha_0^{\text{out}} - \Delta\alpha_0^{\text{in}}}{\omega_C - \omega_G} + n\frac{2\pi}{\omega_C - \omega_G}. \qquad \text{(F.4)}$$

The second term on the right-hand of Eq. (F.4) is the synodic period between Ganymede and Callisto: it is the time required by the two moons to return in the same configuration of relative phase. Therefore, the rephasing period is made up of two terms, the first one depending on the initial conditions provided by the $\mathcal{C}$-connected states considered and the second one (the synodic period) independent from it.

Eventually, we observe that Eq. (F.4) is independent from t. Therefore, the rephasing orbit can be found at any time $t \neq 0$, i.e., for other points $(x, y) \neq (x, y)_0^3$ along one of the two branches of the TO around $\mathbf{x}_0^3$.

Appendix G

Single-shooting algorithm

Trajectory design in the CR3BP necessitate extensive use of numerical techniques, since analytical solutions are not available. A general differential correction procedure based on Newton's method is here presented and developed. The goal is a fixed end state to be reached by variation of the initial state. Consider a general design vector $\mathbf{X}$ of n free variables X_i at the initial time t_0

$$\mathbf{X} = \{X_1, X_2, \ldots, X_n\}^{\mathrm{T}} \tag{G.1}$$

subjected at the final time t_f to a set of m equality constraints:

$$\mathbf{F}(\mathbf{X}) = \begin{Bmatrix} F_1(\mathbf{X}) \\ F_2(\mathbf{X}) \\ \vdots \\ F_m(\mathbf{X}) \end{Bmatrix} = \mathbf{0} \tag{G.2}$$

and p inequality constraints:

$$\mathbf{F}^{\mathrm{IN}}(\mathbf{X}) = \begin{Bmatrix} F_1^{\mathrm{IN}}(\mathbf{X}) \\ F_2^{\mathrm{IN}}(\mathbf{X}) \\ \vdots \\ F_p^{\mathrm{IN}}(\mathbf{X}) \end{Bmatrix} < \mathbf{0}. \tag{G.3}$$

A possible set of design variable could be position, velocity and time while the constraints vector may include path restrictions on position and velocity, or energy requirements on the Jacobi constant. An example of inequality constraint could be a specific requirement on the flight path angle γ, i.e., $\gamma_{\min} < \gamma < \gamma_{\max}$. Then, an algorithm is developed such that, starting from

an initial guess $\mathbf{X}_0$ of the design variables it will converge towards the true solution satisfying the constraints $\mathbf{F}(\mathbf{X}) = \mathbf{0}$. Expanding the constraints to a first order Taylor series yields:

$$\mathbf{F}(\mathbf{X}) \approx \mathbf{F}(\mathbf{X})_0 + D\mathbf{F}(\mathbf{X}_0)(\mathbf{X} - \mathbf{X}_0) + o(||\mathbf{X} - \mathbf{X}_0||^2) \qquad \text{(G.4)}$$

where $\mathbf{X}$ is assumed to be close to $\mathbf{X}_0$ and $D\mathbf{F}(\mathbf{X}_0)$ is the Jacobian matrix

$$D\mathbf{F} = \frac{\partial \mathbf{F}(\mathbf{X})}{\partial \mathbf{X}} = \begin{bmatrix} \frac{\partial F_1}{\partial X_1} & \frac{\partial F_1}{\partial X_2} & \cdots & \frac{\partial F_1}{\partial X_n} \\ \frac{\partial F_2}{\partial X_1} & \frac{\partial F_2}{\partial X_2} & \cdots & \frac{\partial F_2}{\partial X_n} \\ \vdots & \vdots & \ddots & \vdots \\ \frac{\partial F_n}{\partial X_1} & \frac{\partial F_n}{\partial X_2} & \cdots & \frac{\partial F_n}{\partial X_n} \\ \frac{\partial F_1^{\text{IN}}}{\partial X_1} & \frac{\partial F_1^{\text{IN}}}{\partial X_2} & \cdots & \frac{\partial F_1^{\text{IN}}}{\partial X_n} \\ \frac{\partial F_2^{\text{IN}}}{\partial X_1} & \frac{\partial F_2^{\text{IN}}}{\partial X_2} & \cdots & \frac{\partial F_2^{\text{IN}}}{\partial X_n} \\ \vdots & \vdots & \ddots & \vdots \\ \frac{\partial F_p^{\text{IN}}}{\partial X_1} & \frac{\partial F_p^{\text{IN}}}{\partial X_2} & \cdots & \frac{\partial F_p^{\text{IN}}}{\partial X_n} \end{bmatrix} \qquad \text{(G.5)}$$

evaluated at the point $\mathbf{X}_0$. The minimum size of this matrix is $m \times n$ and the maximum size is $(m + p) \times n$: the j-th $(j = m + 1, \ldots, p)$ row is only evaluated if the j-th inequality is violated, i.e., $F_j^{\text{IN}} > 0$, otherwise it is removed from $D\mathbf{F}$ at the current iteration step. Since $\mathbf{F}(\mathbf{X})$ has to satisfy the constraint (G.2) $\mathbf{F}(\mathbf{X}) = \mathbf{0}$, neglecting the higher order terms, Eq. (G.5) can be rewritten as an iterative function, i.e.,

$$\mathbf{F}(\mathbf{X}_i) + D\mathbf{F}(\mathbf{X}_i)(\mathbf{X}_{i+1} - \mathbf{X}_i) = \mathbf{0}. \qquad \text{(G.6)}$$

Calling q the actual number of rows at the i-th iteration $m \leq q \leq m + p$, in case $n = q$ the Jacobian matrix is a square and the iteration process is reduced to a simple matrix inversion, that is:

$$\mathbf{X}_{i+1} = \mathbf{X}_i - D\mathbf{F}(\mathbf{X}_0)^{-1}\mathbf{F}(\mathbf{X}_i). \qquad \text{(G.7)}$$

Conversely, if $n > q$ an infinite number of solution is available; in this case the solution is evaluated through the least squares method:

$$\mathbf{X}_{i+1} = \mathbf{X}_i - D\mathbf{X}(\mathbf{X}_i)^{\text{T}} \left[D\mathbf{F}(\mathbf{X}_i)D\mathbf{X}_i^{\text{T}} \right]^{-1} \mathbf{F}(\mathbf{X}_i). \qquad \text{(G.8)}$$

The matrix $D\mathbf{X}(\mathbf{X}_i)^{\text{T}} \left[D\mathbf{F}(\mathbf{X}_i)D\mathbf{X}_i^{\text{T}} \right]^{-1}$ is often called *pseudo-inverse matrix*. In both the cases (G.7) and (G.8) the iteration process is repeated until the

constraint vector falls below an arbitrary small tolerance $||\mathbf{F}(\mathbf{X}_i)|| < \epsilon$. The norm of the full constraint vector may not always yield the best performance, hence this criterion can be adjusted accordingly if necessary. Equations (G.7) and (G.8) yield the same result as that found by Eq. (2.115) being this new formulation more general in term of the constraints applied.

In summary we can summarize the algorithm as follows:

1. Determine the free variable vector $\mathbf{X}$, according with the problem requirements and choose an adequate initial solution guess $\mathbf{X}_0$.

2. Define the constraints equalities vector $\mathbf{F}(\mathbf{X})$ and the inequality vector $\mathbf{F}^{\mathrm{IN}}(\mathbf{X})$.

3. Define the complete $(m + p) \times n$ Jacobian matrix $D\mathbf{F}(\mathbf{X})$.

4. At each iteration step evaluate the proper number q of rows of the Jacobian matrix and use equation (G.7) or (G.8) if $n = q$ or $n > q$ respectively.

5. Iterate until $||\mathbf{F}(X_i)|| < \epsilon$.

If $p = 0$ (all the constraints are generated as equality) and the initial guess $\mathbf{X}_0$ is sufficiently close to a true solution, the algorithm will converge quadratically. We talk about *single shooting* techniques because only changes to the initial guess are applied, leaving unperturbed the rest of the trajectory.

G.1 Example: fixed-time single shooting

We provide here an application of the single-shooting technique in the framework of the planar CR3BP with control on the initial velocity and constraints on the final state. Let

$$\mathbf{X} = \begin{Bmatrix} X_1 \\ X_2 \end{Bmatrix} = \begin{Bmatrix} \dot{x}_0 \\ \dot{y}_0 \end{Bmatrix} \tag{G.9}$$

be the control vector on the initial velocity. The position components $\{x_0, y_0\}$ are fixed at the initial time t_0. The target point at the final fixed time t_f is fixed, hence the constraints vector can be written as

$$\mathbf{F}(\mathbf{X}) = \begin{Bmatrix} F_1 \\ F_2 \end{Bmatrix} = \begin{Bmatrix} x_f - x_{\mathrm{T}} \\ y_f - y_{\mathrm{T}} \end{Bmatrix}, \tag{G.10}$$
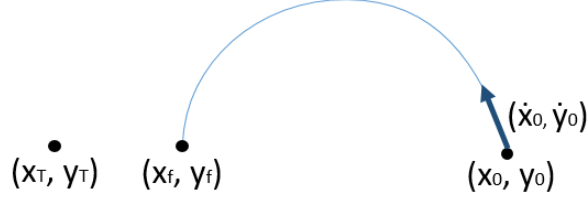
Figure G.1: An example of single shooting problem. From the initial fixed point (x_0, y_0) the final target $(x_\mathrm{T}, y_\mathrm{T})$ must be reached by variations on the initial velocity $(\dot{x}_0, \dot{y}_0)$.

being $\{x_f, y_f\}^\mathrm{T} = \{x(t_f), y(t_f)\}^\mathrm{T}$ the final state at time t_f and $\{x_\mathrm{T}, y_\mathrm{T}\}^\mathrm{T}$ the desired final state at the same time. By variation of the initial state, i.e., varying the initial velocity components, we want to reach the desired target point. The problem is sketched in Fig G.1. Since there are not inequality constraints, $p = 0$ and the dimension of the Jacobian matrix is $m \times n = 2 \times 2$:

$$D\mathbf{F} = \frac{\mathbf{F}(\mathbf{X})}{\partial \mathbf{X}} = \begin{bmatrix} \dfrac{\partial F_1}{\partial X_1} & \dfrac{\partial F_1}{\partial X_2} \\ \dfrac{\partial F_2}{\partial X_1} & \dfrac{\partial F_2}{\partial X_2} \end{bmatrix}. \tag{G.11}$$

The components of the Jacobian matrix can be calculated by substituting Eqs. (G.9) and (G.10) into Eq. (G.11):

$$\frac{\partial F_1}{\partial X_1} = \frac{\partial (x_f - x_\mathrm{T})}{\partial \dot{x}_0} = \frac{\partial x_f}{\partial \dot{x}_0} = \Phi_{14}, \tag{G.12a}$$

$$\frac{\partial F_1}{\partial X_2} = \frac{\partial (x_f - x_\mathrm{T})}{\partial \dot{y}_0} = \frac{\partial x_f}{\partial \dot{y}_0} = \Phi_{15}, \tag{G.12b}$$

$$\frac{\partial F_2}{\partial X_1} = \frac{\partial (y_f - y_\mathrm{T})}{\partial \dot{x}_0} = \frac{\partial y_f}{\partial \dot{x}_0} = \Phi_{24}, \tag{G.12c}$$

$$\frac{\partial F_2}{\partial X_2} = \frac{\partial (y_f - y_\mathrm{T})}{\partial \dot{y}_0} = \frac{\partial y_f}{\partial \dot{y}_0} = \Phi_{25}, \tag{G.12d}$$

being Φ_{ij} the components of the STM from Eq. (2.51) evaluated at the final time $t = t_f$. Therefore, we can rewrite the Jacobian matrix as:

$$D\mathbf{F} = \frac{\mathbf{F}(\mathbf{X})}{\partial \mathbf{X}} = \begin{bmatrix} \Phi_{14} & \Phi_{15} \\ \Phi_{24} & \Phi_{25} \end{bmatrix}. \tag{G.13}$$

It is straightforward to invert this matrix:

$$D\mathbf{F}(\mathbf{X}) = \frac{1}{\det(D\mathbf{F}(\mathbf{X}))} \begin{bmatrix} \Phi_{25} & -\Phi_{15} \\ -\Phi_{24} & \Phi_{14} \end{bmatrix}. \tag{G.14}$$

We can now apply the iterative process described by Eq. (G.7) from a suitable initial guess $\mathbf{X}_0$.

This technique is the same as that employed in the derivation of Eq. (2.56). Thus, the solution obtained through this new formulation is equivalent to the result from Eq. (2.56).

Bibliography

[Alessi et al., 2010] Alessi, E. M. et al. (2010). *The Role and Usage of Libration Point Orbits in the Earth-Moon System*. Universitat de Barcelona.

[Burton, 1966] Burton, T. (1966). Linear differential equations with periodic coefficients. *Proceedings of the American Mathematical Society*, 17(2):327–329.

[Campagnola et al., 2014] Campagnola, S., Buffington, B. B., and Petropoulos, A. E. (2014). Jovian tour design for orbiter and lander missions to europa. *Acta Astronautica*, 100:68–81.

[Castelli, 2012] Castelli, R. (2012). Regions of prevalence in the coupled restricted three-body problems approximation. *Communications in Nonlinear Science and Numerical Simulation*, 17(2):804–816.

[Colasurdo et al., 2014] Colasurdo, G., Zavoli, A., Longo, A., Casalino, L., and Simeoni, F. (2014). Tour of jupiter galilean moons: Winning solution of gtoc6. *Acta Astronautica*, 102:190–199.

[Conley, 1968] Conley, C. (1968). Low energy transit orbits in the restricted three-body problems. *SIAM Journal on Applied Mathematics*, 16(4):732–746.

[Corrêa et al., 2004] Corrêa, A. A., Gómez, G., and Stuchi, T. J. (2004). Transfer orbits guided by the unstable/stable manifolds of the lagrangian points. Congreso Brasileño de Dinamica Orbital.

[Fantino and Castelli, 2016a] Fantino, E. and Castelli, R. (2016a). Efficient design of direct low-energy transfers in multi-moon systems. *Celestial Mechanics and Dynamical Astronomy*, pages 1–22.

[Fantino and Castelli, 2016b] Fantino, E. and Castelli, R. (2016b). Two-body approximations in the design of low-energy transfers between galilean moons. In *Astrodynamics Network AstroNet-II*, pages 63–71. Springer.

[Farquhar and Kamel, 1973] Farquhar, R. W. and Kamel, A. A. (1973). Quasi-periodic orbits about the translunar libration point. *Celestial Mechanics*, 7(4):458–473.

[Floquet, 1883] Floquet, G. (1883). Sur les équations différentielles linéaires à coefficients périodiques. In *Annales scientifiques de l'École normale supérieure*, volume 12, pages 47–88.

[Gómez, 2001] Gómez, G. (2001). *Dynamics and Mission Design Near Libration Points, Vol I: Fundamentals: the Case of Collinear Libration Points*, volume 1. World Scientific.

[Gómez et al., 2001] Gómez, G., Jorba, À., Simó, C., and Masdemont, J. (2001). *Dynamics and Mission Design Near Libration Points: Volume III: Advanced Methods for Collinear Points*, volume 4. World Scientific.

[Gómez et al., 2004] Gómez, G., Koon, W., Lo, M., Marsden, J., Masdemont, J., and Ross, S. (2004). Connecting orbits and invariant manifolds in the spatial restricted three-body problem. *Nonlinearity*, 17(5):1571.

[Gómez and Mondelo, 2001] Gómez, G. and Mondelo, J. M. (2001). The dynamics around the collinear equilibrium points of the rtbp. *Physica D: Nonlinear Phenomena*, 157(4):283–321.

[Grasset et al., 2013] Grasset, O., Dougherty, M., Coustenis, A., Bunce, E., Erd, C., Titov, D., Blanc, M., Coates, A., Drossart, P., Fletcher, L., et al. (2013). Jupiter icy moons explorer (juice): An esa mission to orbit ganymede and to characterise the jupiter system. *Planetary and Space Science*, 78:1–21.

[Grover and Ross, 2009] Grover, P. and Ross, S. D. (2009). Designing trajectories in a planet-moon environment using the controlled keplerian map. *Journal of guidance, control, and dynamics*, 32(2):437–444.

[Guckenheimer and Holmes, 1983] Guckenheimer, J. and Holmes, P. (1983). Local bifurcations. In *Nonlinear oscillations, dynamical systems, and bifurcations of vector fields*, pages 117–165. Springer.

[Howell and Pernicka, 1987] Howell, K. and Pernicka, H. (1987). Numerical determination of lissajous trajectories in the restricted three-body problem. *Celestial Mechanics*, 41(1-4):107–124.

[Howell, 1984] Howell, K. C. (1984). Three-dimensional, periodic, halo orbits. *Celestial Mechanics*, 32(1):53–71.

[Izzo et al., 2013] Izzo, D., Simões, L. F., Märtens, M., De Croon, G. C., Heritier, A., and Yam, C. H. (2013). Search for a grand tour of the jupiter galilean moons. In *Proceedings of the 15th annual conference on Genetic and evolutionary computation*, pages 1301–1308. ACM.

[Koon et al., 2000] Koon, W. S., Lo, M. W., Marsden, J. E., and Ross, S. D. (2000). Dynamical systems, the three-body problem and space mission design.

[Koon et al., 2001] Koon, W. S., Lo, M. W., Marsden, J. E., and Ross, S. D. (2001). Low energy transfer to the moon. In *Dynamics of Natural and Artificial Celestial Bodies*, pages 63–73. Springer.

[Koon et al., 2008] Koon, W. S., Lo, M. W., Marsden, J. E., and Ross, S. D. (2008). Dynamical systems, the three-body problem and space mission design. *Free online Copy: Marsden Books.*

[Koon et al., 2002] Koon, W. S., Marsden, J. E., and Ross, S. D. (2002). Constructing a low energy transfer. In *Celestial Mechanics: Dedicated to Donald Saari for His 60th Birthday: Proceedings of an International Conference on Celestial Mechanics, December 15-19, 1999, Northwestern University, Evanston, Illinois*, volume 292, page 129. American Mathematical Soc.

[Lam et al., 2015] Lam, T., Camacho, J., and Buffington, B. (2015). The europa mission: Multiple europa flyby trajectory design trades and challenges. In *AAS/AIAA Astrodynamics Specialist Conference, Vail, Colorado, number Paper No. AAS*, pages 15–657.

[Lantoine and Russell, 2011] Lantoine, G. and Russell, R. P. (2011). Complete closed-form solutions of the stark problem. *Celestial Mechanics and Dynamical Astronomy*, 109(4):333–366.

[Lantoine et al., 2011] Lantoine, G., Russell, R. P., and Campagnola, S. (2011). Optimization of low-energy resonant hopping transfers between planetary moons. *Acta Astronautica*, 68(7):1361–1378.

[Masdemont and Mondelo, 2004] Masdemont, J. and Mondelo, J. M. (2004). Advanced topics in astrodynamics - notes for the numerical and analytical techniques.

[McKinley and Levine, 1998] McKinley, S. and Levine, M. (1998). Cubic spline interpolation. *College of the Redwoods*, 45(1):1049–1060.

[Moulton, 2012] Moulton, F. R. (2012). *An introduction to celestial mechanics.* Courier Corporation.

[Parker and Anderson, 2013] Parker, J. S. and Anderson, R. L. (2013). Low-energy lunar trajectory design. *Pasadena: Jet Propulsion Laboratory.*

[Parker and Chua, 2012] Parker, T. S. and Chua, L. (2012). *Practical numerical algorithms for chaotic systems.* Springer Science & Business Media.

[Perko, 2013] Perko, L. (2013). *Differential equations and dynamical systems*, volume 7. Springer Science & Business Media.

[Petropoulos, 2013] Petropoulos, A. E. (2013). Problem description for the 6th global trajectory optimisation competition. *h ttp://sophia. estec. esa. int/gtoc_portal/wp-content/uploads/2012/11/gtoc6_problem_stmt-2. pdf.*

[Poincaré, 1882] Poincaré, H. (1882). Mémoire sur les courbes défines par une équation différentielle (ii). *Journal de mathématiques pures et appliquées*, pages 251–296.

[Richardson, 1980] Richardson, D. L. (1980). Analytic construction of periodic orbits about the collinear points. *Celestial mechanics*, 22(3):241–253.

[Ross et al., 2003] Ross, S. D., Koon, W. S., Lo, M. W., and Marsden, J. E. (2003). *Design of a multi-moon orbiter.* Number 114. American Astronautical Society.

[Roy, 2004] Roy, A. E. (2004). *Orbital motion.* CRC Press.

[Sims, 2006] Sims, J. A. (2006). *Jupiter Icy Moons Orbiter Mission Design Overview.* Citeseer.

[Steves et al., 2006] Steves, B. A., Maciejewski, A. J., and Hendry, M. (2006). *Chaotic Worlds: From Order to Disorder in Gravitational N-Body Dynamical Systems*, volume 227. Springer Science & Business Media.

[Sturm, 1835] Sturm, C. (1835). *Mémoire sur la résolution des équations numériques.*

[Szebehely, 2012] Szebehely, V. (2012). *Theory of orbit: The restricted problem of three Bodies.* Elsevier.

[Villac and Scheeres, 2003] Villac, B. and Scheeres, D. J. (2003). Escaping trajectories in the hill three-body problem and applications. *Journal of guidance, control, and dynamics*, 26(2):224–232.

[Zanzottera et al., 2012] Zanzottera, A., Mingotti, G., Castelli, R., and Dellnitz, M. (2012). Intersecting invariant manifolds in spatial restricted threebody problems: design and optimization of earth-to-halo transfers in the sun–earth–moon scenario. *Communications in Nonlinear Science and Numerical Simulation*, 17(2):832–843.